Research Center

Separation Control for Rotorcraft
Final Progress Report

Contract DAAG55-98-C-0066

Peter F. Lorber, Duane C. McCormick,
Brian E. Wake, Razvan Florea

United Technologies Research Center
East Hartford, CT 06108

August 2002

UTRC Report 2002-5.200.0015-5

REPORT DOCUMENTATION PAGE

Form Approved
OMB NO. 0704-0188

1. AGENCY USE ONLY (Leave Blank)	1. REPORT DATE	3. REPORT TYPE AND DATES COVERED
	08-30-2002	Final Progress 9/1/1998-8/31/2002

4. TITLE AND SUBTITLE
Separation Control for Rotorcraft
Final Progress Report

5. FUNDING NUMBERS
DAAG55-98-C-0066

6. AUTHOR(S)
Peter F. Lorber, Duane C. McCormick,
Brian E. Wake, Razvan Florea

7. PERFORMING ORGANIZATION NAME(S) AND ADDRESS(ES)
United Technologies Research Center
411 Silver Lane
East Hartford, CT 06108

8. PERFORMING ORGANIZATION REPORT NUMBER
UTRC Report 2002-5.200.0015-5

9. SPONSORING / MONITORING AGENCY NAME(S) AND ADDRESS(ES)
U. S. Army Research Office
P.O. Box 12211
Research Triangle Park, NC 27709-2211

10. SPONSORING / MONITORING AGENCY REPORT NUMBER
P-39174-EG

11. SUPPLEMENTARY NOTES
The views, opinions and/or findings contained in this report are those of the author(s) and should not be construed as an official Department of the Army position, policy or decision, unless so designated by other documentation.

12 a. DISTRIBUTION / AVAILABILITY STATEMENT
Approved for public release; distribution unlimited.

12 b. DISTRIBUTION CODE

13. ABSTRACT (Maximum 200 words)
Active flow control can play a significant role in improving rotorcraft performance by delaying flow separation. Retreating blade stall (RBS) limits rotor capability to generate lift and transmits large pitching moments to the flight control system. This project developed compact, high-power flow control actuators for RBS and evaluated them using a combination of computation and a wind tunnel test on a full scale helicopter blade section. A set of electromechanical Directed Synthetic Jet (DSJ) actuator modules were designed, fabricated, and installed. The actuators produced the intended unsteady momentum coefficient of 0.1% at Mach 0.4 at 260 Hz. Flow control improved airfoil steady and dynamic stall characteristics, but the improvements were not as large as desired, especially for dynamic stall at higher Mach number. Additional computations of the coupled flow fields showed that moving the DSJ exit slot further aft could increase recovery of post-stall lift, but could not further increase unsteady peak lift or stall delay at momentum coefficients less than 0.5%. A 2nd generation DSJ actuator was designed and bench tested. By operating two slots, inboard and outboard of the piston, this actuator avoids back acoustic losses and can tolerate the centrifugal loads of a rotating blade

14. SUBJECT TERMS
Helicopters Dynamic Stall Synthetic jets
Flow Control Separation Control

15. NUMBER OF PAGES
72

16. PRICE CODE

17. SECURITY CLASSIFICATION OR REPORT	18. SECURITY CLASSIFICATION ON THIS PAGE	19. SECURITY CLASSIFICATION OF ABSTRACT	20. LIMITATION OF ABSTRACT
UNCLASSIFIED	**UNCLASSIFIED**	**UNCLASSIFIED**	**UL**

NSN 7540-01-280-5500
Standard Form 298 (Rev.2-89)
Prescribed by ANSI Std. 239-18

Foreword

Summary

Active flow control technologies can play a significant role in improving rotorcraft performance by delaying flow separation in several key locations. Retreating blade stall (RBS) limits rotor capability to generate lift and transmits large impulsive blade pitching moments to the flight control system. This project concentrated on developing compact, high-power flow control actuators for RBS and evaluating their effectiveness using a combination of computation and a wind tunnel test on a full scale helicopter blade section. A set of electromechanical Directed Synthetic Jet (DSJ) actuator modules were designed, fabricated, and installed inside the blade section. The actuators succeeded in producing the intended unsteady momentum coefficient of 0.1% at Mach 0.4 at the desired frequency of 260 Hz. Flow control improved airfoil steady and dynamic stall characteristics, but the measured improvements were not as large as desired, especially for dynamic stall at higher Mach number. Additional computational simulations of the coupled external and internal flow fields during unsteady stall showed that moving the DSJ exit slot further aft could increase recovery of post-stall lift, but such geometric variations were not able to provide further increases in unsteady peak lift or stall delay at momentum coefficients less than 0.5%. A 2nd generation DSJ actuator with increased authority was designed and bench tested. By operating two slots, inboard and outboard of the piston, this actuator avoids back acoustic losses and can tolerate the centrifugal loads of a rotating blade.

Acknowledgements

This activity was conduced as part of the DARPA Micro Adaptive Flow Control (MAFC) Program, James McMichael, William Scheuren and Richard Wlezian, Program Managers. It was supported by the U.S. Army Research Office under Contract DAAG55-98-C-0066, Dr. Thomas Doligalski, Technical Monitor.

Table of Contents

List of Illustrations

List of Tables

Introduction

Statement of the Problem Studied

High performance future rotorcraft will need significant improvements in multiple attributes, including increased range for global self-deployability, increased speed and performance (maneuverability and agility) for demanding combat missions, increased payload, reduced external noise emissions, and reduced cabin noise and vibration. Active flow control technologies may be able to play a significant role in achieving these objectives by a) delaying retreating blade stall to increase rotor maximum lift capability and aerodynamic efficiency and minimize vibratory loads in forward flight, b) minimizing airframe bluff body separation to reduce drag and induced vibration, and c) reducing internal flow turning losses and distortion to improve the efficiency of compact propulsion system installations. Successful application of flow control to rotorcraft will require the development of innovative technologies that efficiently integrate an understanding of the underlying fluid dynamics with a robust and efficient actuation sensing and control system.

Phase 1 of this Micro-Adaptive Flow Control (MAFC) activity examined application of flow control to these three areas. Phase 2 focused on developing an on-blade separation control system for retreating blade stall. The specific goal was to delay stall onset by at least 5° in steady and unsteady motion and to increase the steady maximum lift coefficient, C_L^{max}, by at least 10%. Two actuation paths were pursued, electromechanical directed synthetic jets (DSJ) and phased plasma actuators. The effectiveness of the electromechanical DSJ actuators was studied using a full scale pitching blade section experiment. Plasma actuation development was conducted under a separately funded activity at the University of Notre Dame. Aircraft system benefits from flow control were determined for representative military missions.

Retreating Blade Stall

Retreating Blade Stall (RBS) establishes limits on rotor load and flight speed. In addition to the loss of capability to generate lift, unsteady blade stall transmits large impulsive blade pitching moments to the flight control system. In order to prevent excess control loads, stall boundaries are set that define the maximum blade load capability as a function of rotor load and flight speed. These limits impact maneuverability and agility as well as speed and payload. The fluid mechanism involved in blade stall is boundary layer separation near the leading edge of the rotor blade during the rapid motion to high blade angle of attack that occurs when the blade is on the retreating side of the rotor disc. This dynamic stall phenomenon has been extensively studied using pitching airfoil sections, and the basic process appears well understood (Refs. 1-3). Some separation is typically present on the inboard portion of the retreating blade in forward flight, but the region of separation grows rapidly as load and speed increase. Stalled flow locations on the rotor disc have been identified by surface measurements (Refs. 4-5). Figure 1 is based on model rotor experimental data and shows the relatively small stall regions for a moderate load condition, and the significantly larger stall regions at a high load condition close to the stall boundary. The combination of detailed unsteady airfoil experiments and computations and global rotor measurements has defined the RBS phenomenon that must be controlled and the conditions under which control is required.

A practical way of avoiding or significantly delaying RBS has not yet been demonstrated under flight conditions. Separation control must be effective in an unsteady, compressible, high Reynolds number flow. The combination of the blade cyclic pitch required to maintain rotor trim in forward flight, aeroelastic twist, and induced velocity variations causes a rapid increase in local blade section angle of attack. Reduced frequencies are typically $k = \omega c/2U \sim 0.05$ to 0.15, with maximum instantaneous pitch rates of $A = \dot{\alpha} c/2U \sim 0.002$ to 0.02. The relative external flow Mach numbers are M = 0.3 to 0.5, while the peak local Mach numbers near the separation location of x/c= 0.05 to 0.15 are typically M = 1.1 to 1.3. Full scale Reynolds numbers are Re ~ 4×10^6, with transition to turbulence occurring ahead of separation (Refs. 1-3).

Any stall control approach applied on the retreating blade side must not create a significant drag penalty on the advancing side, where the relative external Mach numbers are 0.6 to 0.85. Further, the approach must be practically incorporated into the confined space in a rotating blade, and be robust enough to survive centrifugal loads of 200 to 400g and vibratory loads of several g generated by unsteady blade motion.

Flow Control Technologies.

Steady flow control methods such as air injection or suction have been investigated to improve airfoil and fixed wing stall characteristics, but transferring sufficient fluid from the fixed system to a rotating helicopter blade at acceptable levels of power and complexity presents significant difficulties. Unsteady excitation has been studied previously as a way to delay or avoid separation (Ref. 6). The most extensive series of experiments have been conducted by Wygnanski and his colleagues (Refs. 7-10). While the precise mechanism is not fully understood, the concept involves low level periodic forcing to modulate the formation of vortices in a separating flow. At or near an optimum frequency, $F^+ = fc/U \sim 1$, high streamwise momentum flow is driven towards the surface, energizing the boundary layer and avoiding massive separation. The periodic excitation can be provided by moving a mechanical element, by injecting an unsteady jet of air, or by alternate suction and blowing. For the later two methods, the key parameter is the unsteady momentum coefficient, $C_\mu = \left(\rho h u^2\right)_{JET} / \left(\rho c U^2\right)_\infty$, where u_{JET} is the amplitude of the unsteady jet velocity and h is the width of the jet exit.

Technical Approach

The primary separation control technique that was applied in the current work is the Directed Synthetic Jet (DSJ). It utilizes the phenomena of acoustic streaming (Ref. 11) to form a synthetic jet (Ref. 12) with a curved exit neck optimized for separation control (Ref. 13). Figure 2 shows a typical DSJ configuration. The curved neck allows low momentum fluid to be ingested during the suction phase of the DSJ and high momentum fluid to be ejected during the blowing phase. Both phases energize the boundary layer. At high enough Cμ, the DSJ can suppress separation without the need to operate at an optimum F^+. The concept is more fully described in Ref. 13, together with initial validation using a planar diffuser.

Summary of the Primary Results

Summary of Phase 1 Activities

Airframe Separation Control

Airframe separation has become increasingly important since 1) observability requirements are leading to less-aerodynamic airframe geometries and 2) increased emphasis is being placed on rotorcraft fuel consumption and self-deployability. Airframe flow separation can also affect aircraft vibratory loads when separated flow from the rotor hub and pylon strikes the empennage surfaces. Reductions in airframe separation can reduce drag (download) levels in hover, which impacts payload, and in forward flight (parasite drag), which impacts speed and range. While complete control of airframe separation may be impractical, localized control at key locations on the pylon and other sharply angled sections of the airframe can result in significant drag reduction, eliminate undesirable separated flow interactions, and relax the compromises required to minimize observability. Figure 3 shows drag coefficients for a variety of fixed and rotary wing airframes as a function of the airframe length to diameter ratio. While current low drag civil helicopter designs approach theoretical minimum drag levels, military designs typically have much higher drag, especially if the design requirements include reduced observability. An aggressive goal is to reduce the bluff body drag of such designs by 50%.

A small scale demonstration experiment was conducted using a generic three dimensional bluff body that represented a drive system pylon or protrusion. Figure 4 shows the body, which has a rounded nose, a flat mid section, and a 45° sloped aft ramp. Flow control experiments were conducted in the UTRC Boundary Layer Tunnel at a Reynolds number based on length of approximately 1 million, and a Mach number of 0.1. An internal speaker was used to actuate single or double DSJ slots on the ramp. Lift and drag was measured using a two-component force balance, and the separated flow region behind the body was visualized using a tuft rake. Figure 5 shows that activation of the DSJ at a reduced frequency of $F^+ \sim 0.6$ and a momentum coefficient of $C\mu \sim 0.015$ significantly reduced the size of the separated flow region. Drag measurements showed that the form drag was reduced by approximately 60%, from $C_D \sim 0.27$ to 0.10. Interpreting the drag measurements were complicated by the need to first subtract out the induced drag generated by lift on the body to. Reattaching the flow over the aft facing 45° ramp created a low aspect ratio wing with strong tip vortices and significant induced drag. The induced drag here on an isolated component mounted above a plate could presumably be avoided by appropriate design of the complete airframe that accounted for the controlled flow. Based upon the reduction in form drag and the measured flow control power in the DSJ slot, there was a net power benefit of approximately 30:1. This value would be reduced by ~50% by inefficiencies in converting from electrical power to flow control power, but the net return would still be quite high.

An aircraft system benefits study was performed based upon self deployment of a reconnaissance / attack helicopter. For each 10% reduction in parasite drag, there would be up to 4% increase in range, 4 kts increase in cruise speed, and 6% increase in power margin for maneuverability. Actuation system challenges seemed moderate because the external flow velocities were in the Mach 0.1 to 0.25 range, and temperature and

vibration load constraints were not severe. Electromechanical actuation seemed quite feasible. While airframe separation control work was not continued into Phase 2, the potential for substantial benefit at moderate cost may make further investigation desirable in the future.

Enhanced Flow Turning

Internal flow turning can be a significant rotorcraft design constraint because of requirements for low observability and high efficiency. Airframe geometries are often dictated by low loss considerations related to inlet and exhaust flow paths through the aircraft. Low observability often places further requirements on these geometries, degrading the resulting aerodynamic profile of the airframe. The resulting separated flow increases drag and vibratory loads. An ability to provide high efficiency flow turning in reduced areas could mitigate these degradations and improve aircraft attributes. Flow turning within a duct is a common feature of many rotorcraft designs. Propulsion system inlets and exhaust flows often negotiate complex paths dictated by either adjacent structures or observability constraints. The resulting paths typically use large radii turning segments to reduce turning losses, since high flow efficiency is important. While turning vanes can be used to maintain flow efficiency with smaller radii, turning limits are still reached when design space is limited.

Figure 6 shows the experiment used to demonstrate internal flow turning control. A compact 90° rectangular elbow with a ratio of turn radius to duct height of 0.6 was built. At a flow velocity of 60 fps, the Reynolds number based on width was approximately 200,000. Without control, flow losses of 1.4 to 1.5 dynamic heads were measured, as expected. DSJ control was applied using speaker actuation through single and double slots on the inner radius. Wall static and inflow total pressure measurements were made together with tuft flow visualization. Figure 7 summarizes the results. Flow control was able to reduce distortion across the duct by 1.5 dynamic heads, and reduce total pressure losses by 1 dynamic head. This represented a 30:1return on the control flow power required.

The system study indicated that engine inlet, exhaust, IR suppression, and other internal flow passages could benefit from separation control. Actuation requirements are challenging because of the high required frequencies (> 500 Hz), flow velocities (inlet flows at Mach ~ 0.5), and temperatures (exhaust flows at T~1150F). Actuation power consumption is a significant issue, since the system will usually remain on. A periodic valve actuator using bleed air appeared to be most attractive. This activity also was not continued into Phase 2, however if a specific application with a favorable cost – benefit ratio is identified, the Phase 1 study has shown that substantial reductions in turning-induced total pressure loss and flow distortion can be obtained.

Retreating Blade Stall Control

Phase 1 activities in retreating blade stall control concentrated on identifying required flow control system characteristics from experimental airfoil separation control results obtained by UTRC and other researchers, investigating actuation alternatives, and identifying system requirements and benefits. Previous experimental results, summarized in Table 1, showed that while significant stall delay and lift enhancement has been achieved, the level of unsteady momentum coefficient required for full scale conditions

was not clearly established. A working estimate of $C\mu > 0.001$ (0.1%) at Mach 0.4 was established as a compromise between desired authority and that believed to be achievable by an in-blade actuator in the near term. Several actuation alternatives were studied, including synthetic jets powered by moving voice coils or variable air gap motors, and periodic values modulating bleed or centrifugally pumped air sources. Figure 8 illustrates several of these concepts.

Aircraft system goals were also established based on a reconnaissance / attack class helicopter. They included adding less than 10% to the blade weight (2 lbs/ foot of span), not compromising the structural integrity of the blade spar, minimizing total system

Table 1. Phase 1 Summary of Blade Stall Control Experiments

Result	*Source*	*Mach*	*Reynolds*	*Pitching?*	*Airfoil?*
$C\mu$=.0001 is too low	UTRC 96	0.2-0.4	2-3 $x10^6$	Yes, +-10°	SSC-A09
$C\mu$=.001 is fair $C\mu$=.01 is good	Greenblatt & Wygnanski 98	<0.12	.3-.9$x10^6$	Yes, +-5°	NACA 0015
$C\mu$=.0005 is good	Seifert & Pack 98	0.3	30 x 10^6	No	NACA 0015
$C\mu$=.002-.003 is good	UTRC 98 Expt Computation	0.1 0.2	$1x10^5$ 2 x 10^6	No	SSC-A09

weight (goal of approximately 100 lbs) and power required (less than 15 hp for the complete system), and making the system robust enough to withstand the blade centrifugal and vibratory loads.

The Phase 1 system concept included actuating at a frequency F^+~1 (200-300Hz), and applying control from 40% to 85% of the blade radius through 0.1" to 0.2" slots located at 5% of the chord. Each blade would be divided into three spanwise sections with independent actuation, sensing, and control. The ideal system would minimize power consumption by only actuating each blade on the retreating side of the rotor disc. Aircraft system benefits were primarily identified in terms of improved rotor thrust capabilities and maneuver characteristics. The assessment at the end of Phase 1 was that the level of difficulty was quite high, with the most important challenges for Phase 2 being demonstration of effective stall control at full scale blade conditions using a $C\mu$ level that could be provided by an actuation system that would be practical for the rotor blade.

Retreating Blade Stall Control System Benefits

Rotorcraft benefits from a RBS control system include enhanced performance, mission effectiveness, maneuverability and survivability. The impact of retreating blade stall control on conventional rotor sustained lift limitations is shown in Fig. 9 in terms of rotor thrust versus forward airspeed, based upon a quasi-steady rotor performance analysis. The figure normalizes rotor thrust by the thrust of a baseline rotor at the

minimum power airspeed. Airspeed is represented as rotor advance ratio (airspeed / tip speed). Enhanced rotor performance from a blade flow separation control system is incrementally shown for two levels of improvement. The first increment represents a 5° increase in the stall angle of attack. The second increment adds a 10% increase in C_L^{max} and extends the control out to 95% of the blade radius. At the minimum power airspeed of about 85 knots (advance ratio = .20), the improvements increase blade load capability by 10%. This translates into a 20% increase in turn rate, which would improve the ability of an aircraft engaged in combat to turn on a target. In battlefield situations, these maneuverability improvements could significantly improve rotorcraft survivability. Separation control systems that provide more than 10% increase in C_L^{max} would provide proportionately greater blade load and maneuver improvements.

DSJ impacts on stall related speed limitations for a conventional rotor in forward flight can also be derived from the data in Fig. 9. For a constant operating weight, or normalized thrust, significant improvements are possible. For example, at a normalized thrust of 1.0, where the baseline rotor is limited to an advance ratio of 0.195, or 85 knots TAS, the enhanced rotor performance potentially allows flight to about 0.29 advance ratio, or 125 knots TAS, representing a level flight rotor limited speed improvement of 40 knots. Although the margin decreases as weight is decreased, the improved rotor still allows significant speed increases. At a normalized thrust of 0.90, the advance ratio difference is .035, equating to a speed increase of about 15 knots TAS.

Payload, range and endurance improvements will result from increases in rotor thrust margin. For example, defense aircraft are often required to fly to a remote location (radius point), perform specific operations, and return. This scenario is depicted in Fig. 10 in the form of on-station endurance versus radius of action. Endurance and range enhancements of greater than 25% are made possible by using the additional thrust margin to increase the fuel load at take off where weight limitations would otherwise restrict fuel.

A preliminary analysis was also made for a long range heavy lift/cargo transport mission. RBS control will provide benefits of increased speed (reduced mission time and fuel), improved rotor cruise efficiency and reduced operational risk. Future heavy lift aircraft are planned to transport a 22-ton payload with a range of 2100 nautical miles, and operate to and from unprepared areas. The design of a conventional helicopter that meets these mission requirements can result in a high gross weight and a very large main rotor. One initial design study of such a vehicle produced an operating weight (i.e., vehicle weight without fuel or payload) of about 55,000 lb and a need for at least 65,000 lb of fuel to transport the 22 ton payload to the maximum range, leading to a takeoff gross weight of approximately 165,000 lb. To maintain a disk loading below 15 psf, the rotor diameter was about 120 feet.

Rotor technology that incorporating RBS control would enhance the performance of this mission. Increased rotor cruise efficiency significantly increases the cruise speed and thereby reduces the mission time and the associated fuel required. Forward flight blade-element theory with airfoil data modifications representing a rotor with RBS was used to compute normalized rotor cruise efficiency versus rotor lift coefficient, assuming that cruise speed is varied to maximize rotor efficiency at each C_L. Figure 11 compares the non-dimensional speed variation associated with optimized cruise efficiency as a function of rotor C_L. The increase in cruise speed is most significant for $C_L > .009$, where a

majority of the mission profile would be flown. This is demonstrated in Fig. 12 where non-dimensional rotor lift variation is shown as a function of variations in dimensional weight (i.e., as fuel is consumed) and altitude (i.e., air density change). The density altitude is chosen to approximately optimize the cruise efficiency for each configuration. Following take off of the baseline configuration, rotor stall limits will restrict climb, leading to a mission profile that maintains a very low cruise altitude for about half of the mission duration. After this point the fuel burn has reduced the rotor C_L enough to permit altitude changes to optimize mission performance. For the RBS control configuration, an immediate cruise climb can be initiated following the take off to optimize the fuel consumption. This not only reduces the fuel required (a 15% reduction is estimated), but also reduces risk associated with achieving autorotation in the event of engine failure. The primary assumption is that next generation engine specific fuel consumption will improve enough to offset the effect of increased weight and power for this particular mission. Table 2 provides some key parameters used in the analysis.

The analytical studies summarized here have shown that RBS control can provide a substantial benefit for a wide range of defense aircraft and missions, including improved maneuverability for attack aircraft, improved time on station for utility aircraft, and weight reductions and mission time improvements for future heavy lift cargo aircraft.

Table 2. Notional Heavy Lift Aircraft Parameters

	Baseline	RBS Control
Operating Weight, lbs x 1000	**56**	**51**
Fuel, lbs x 1000	**65**	**55**
Payload, lbs x 1000	**44**	**44**
Takeoff Gr. Wt., lbs x 1000	**165**	**150**
Average Cruise Speed	**130 kts**	**152 kts**
Mission Time	**16.3 hrs**	**13.8 hrs**
Distance	**2100 n mi**	**2100 n mi**

DSJ Flow Control Actuation

Actuation Concept Identification and Selection

Electromechanical Synthetic Jets

Practical DSJ actuation systems were developed and evaluated using a combination of analytical modeling and prototype construction. Figure 13 shows a generic electromechanical DSJ actuator concept and the corresponding electro-acoustic model of the system. Efficiency, defined as the acoustic power converted to useful fluid power ($U_N^2 R_N$) divided by the actuator input power, is a primary metric for actuator performance. Effective actuator designs for the demanding RBS application must be compact to fit within the limited available space, powerful to provide sufficient $C\mu$ at the

appropriate F^+ for the high relative velocities at the blade, robust, and efficient to minimize the power that must be supplied to each blade.

The electro-acoustic model was exercised for a wide range of actuator parameters. From this effort, an understanding of the key parameters for maximizing efficiency was developed. An example parametric study is shown in Fig. 14, which gives efficiency versus neck velocity for three different piston-to-slot area ratios. As indicated, there is an optimum area ratio that maximizes at the operating point efficiency (and is efficient over a wider range). This optimum is related to impedance matching the neck resistance ($\sim u_N/A_N$) to the other circuit resistances ($R_{AE} + R_S$) which maximizes the power flow (circuit theory). Other key parameters important to maximizing efficiency are motor constant and mechanical quality factor. In addition, it is highly desirable to minimize the weight of the moving mass.

A benchmark analytical comparison of the three basic electromechanical motor configurations (moving or voice coil, variable air-gap, and variable reluctance) was performed. Schematic drawings of these motors are shown in Fig. 15. The moving-coil is typically used in acoustic speakers and it offers large, linear displacement and small moving mass. However, this motor is power limited since the coil heat is not easily dissipated. The variable reluctance and air gap motors do not have the fatigue and heat sink problems of moving coil motor since the coils are stationary. However, the moving mass is generally greater. The advantage of the variable air gap is the peak force is much higher (since the magnetic field and attractive force are parallel). However the stroke is limited and tolerance issues more severe. Based upon study of the relative size, weight and efficiency of these different motor embodiments, the moving coil actuator was selected as the best electromechanical choice for the wind tunnel validation experiment, and is recommended for future on-blade applications.

Periodic Modulation

An alternate approach for producing an oscillating jet is to modulate a steady air supply at the required frequency. This approach has been successfully used in several previous wind tunnel experiments. If a steady air supply is readily available, this approach can provide unsteady excitations with lower actuation weight than possible with synthetic jets. This concept would use an air motor to drive a rotating valve to modulate the flow. It offers the advantages of (1) reduced system weight using compressed bleed air available from the engine, (2) reduced system complexity and (3) easily achievable flow and frequency performance requirements. One disadvantage is 4x to 6x higher required flow power to achieve the same amplitude from a 0 to maximum velocity waveform as compared to a waveform where the velocity has alternating sign. The available air supply also presents a practical limitation. Since pressure differentials on the order of only 1 psi are required across the injection slot, use of bleed air at 50-60 psi discards much of energy used to compress it. An ejector can recover some of this energy, but their efficiency is only on the order of 50%. The overall efficiency in delivering the required airflow is no better than 7% for the rotor case, 4-6 times the power required for an ideal DSJ. A separate low pressure blower might be used to minimize the compression power. This was considered impractical because of the added weight, size and complexity and the large ducts required to deliver low pressure air to the slots. The conclusion was that high net power consumption made blowing an impractical means of controlling the flow for the rotorcraft applications considered.

Plasma Actuation

High amplitude steady and unsteady plasma actuation techniques were also investigated in Phase 1. The advantage of plasma actuators is that they would not require any bleed-air sources or moving mechanical parts. The plasma produces a pumping effect, which induces an air flow. A net flow can be induced from an asymmetric electrode pattern. With the proper insulating material, the induced velocity can be maximized by minimizing the electrode gap spacing. A concept has been developed to produce large unsteady velocity fluctuations. It includes a symmetric arrangement of anodes and cathodes on the upper and lower sides of an insulating sheet. Phase 1 activities included demonstration of the phased plasma technique on a flat plate airfoil at angle of attack. Further development of plasma actuation during Phase 2 was transferred to a parallel direct grant from ARO to Notre Dame, and is not discussed here.

Electromechanical Synthetic Jet Actuator Development

Practical DSJ actuation systems were developed and evaluated using a combination of modeling and prototype construction. The lumped parameter electro-acoustic system model was refined for actuator design. To validate and tune the model, a large scale prototype DSJ actuator was built. Figure 16 shows the assembled unit and some of the individual components. The attached schematic shows the assembly and identifies the components associated with the electro-acoustic model. The actuator impedance consists of a 2nd order system that contains moving mass, compliance, and resistance. This system can be more simply represented by a resonant frequency $\omega_o = (C_{AS}\ M_{AT})^{-0.5}$, and mechanical quality factor, $Q_M = R_{AS}\ \omega_o / M_{AT}$. A high quality factor, corresponding to low damping, is critical for achieving practical actuation. The efficiency, defined as the useful fluid power ($U_N^2\ R_N$) divided by the actuator input power, is the primary metric that is maximized within the installation constraints. Exercising the prototype and the analytical model over a range of parameters was useful in determining design criteria. For example, piston leakage, particularly when the back cavity is sealed, results in large loss in efficiency. Also, minimizing moving mass while maximizing mechanical quality factor and motor constant ($BL / RC^{1/2}$) provides the highest efficiency. It is also very important to size the piston correctly in order to provide the best impedance match between the coil and the acoustic load.

The bench top actuation testing and modeling described above identified flexure design as the most challenging issue for actuation integration inside the leading edge. To achieve an actuator that can provide the authority required, a high efficiency system based on a resonant mass and spring was selected. Due to the high external flow velocity of the RBS application, a relatively high actuation frequency (f~260 Hz) is required to reach $F^+ \sim 1$. The combination of this frequency with the moving mass of the actuator (voice coil, piston, and flexure ~0.1 lbm) resulted in a very high required flexure stiffness (~800 lbf/in). Due to the confined space, the moving piston size is quite limited, so that a large flexure displacement (~±0.1") is required to generate the required $C\mu$. Achieving a compact flexure with high stiffness and large displacement was a challenge.

A breakthrough in flexure design was achieved by working with Helical Product Company, which specializes in machined coil springs. With Helical's finite element

method (FEM) analysis and innovative design approach, a solution was developed. Figure 17 shows this machined spring and corresponding assembly for the initial RBS bench top actuator. The machined ends of the spring enable both tension and compression operation (typical coil springs only operate in one or the other mode). The resulting single spring design can be much more compact. The voice coil is attached to the free end of the spring with screw threads and the piston is electron beam (EB) welded onto the free end to maximize strength and minimize weight. The permanent magnet is suspended over the voice coil. Both sealed (with metal bellows) and unsealed piston cases were tested and modeled. With a vented piston backside, the unsealed leakage was found to be acceptable. This significantly simplifies the leading edge integration. Figure 18 shows the excellent agreement between experimental and model results, demonstrating that high actuator authority can be achieved (~200 f/s velocity amplitude in a 0.1" wide slot) in a compact design.

DSJ Actuator Design for Wind Tunnel Experiment

In order to adapt the bench top actuator into a design that could be used for the full scale blade section wind tunnel experiment, a rigid brace was needed for both the fixed end of the spring and the field assembly. For the bench top actuator, these locations were on opposite sides of the piston. Due to the limited space in the blade section leading edge, such an arrangement was not possible. To solve this problem, the voice coil motor was moved inside the spring, co-locating the fixed end of the spring and the field assembly, significantly simplifying the installation and making the actuator more compact. Figure 19 shows a cross section of the motor / spring subassembly in the blade leading edge. Three of these subassemblies were grouped together to form a module pack driving a rectangular piston. Figure 20 shows how five module packs are used to cover the 33” span of the blade section. Each module pack is isolated by partitions that enable a spatial variation in the phase of the forcing. The backside of the pistons are vented through slots on the top and bottom of the blade spar to minimize the acoustic loading and hence the unsealed piston leakage. Figure 21 gives a photograph of the actuator subassembly and module pack components.

The springs were fabricated from corrosion resistant steel, heat treated for increased strength and, after machining, shot peened for improved surface finish and durability. The fifteen springs were individually statically tested for spring rate. The variation from the mean spring rate was plus 4% to minus 3%. Trim weighs were attached to the voice coils to maintain a constant natural frequency for each module. Without the field assembly, the structural losses were identified by hammer test to be about 0.2% damping, consistent with the original bench top actuator. With the field assembly, an additional 0.4% damping is incurred, primarily due to eddy currents in the former tube for the coil. For the assembled module pack, hammer and electrical impedance tests indicated a quality factor of Q_m~50-55 which is somewhat lower than the individual subassembly but still very reasonable.

Due to the cavities and spar slots on the backside of the piston, the electro-acoustic model of this actuation system is more complicated. Figure 22 shows the front and backside loading modeled as two impedances in series (Z_F, Z_B) and the piston leakage as a resistor in parallel (the acoustic mass of leakage gap is neglected). As before, the

actuator impedance (Z_{ACT}) is a second order system consisting of the moving mass, spring compliance, internal losses (Q_m), and the coil resistance (mapped into the acoustic side of the circuit). The expanded piston loading impedances are also shown in the figure. Critical to a successful design is ensuring that the resonant mode of the backside is out of band relative to the operational frequency. Otherwise, a large velocity oscillation will occur in the spar slots and large pressure oscillation across the piston, causing excessive losses. For the current arrangement, this mode is ~600 Hz. The model indicates an efficiency of about 15%, requiring 260 W of electrical power to drive each module pack.

Actuation Geometry Design from CFD

Unsteady Navier Stokes simulations were used to evaluate separation control performance at full scale and to aid in the design of the actuation system. A series of computations using the CFL3D analysis were made for a Sikorsky SC2110 airfoil with an internal DSJ plenum and a contoured exit slot on the upper surface. The computations were performed with the airfoil at fixed pitch, undergoing a constant pitch rate ramp motion, and undergoing a sinusoidal pitch motion. The objective was to improve the effectiveness of the slot and plenum geometries and to predict DSJ performance at realistic Mach and Reynolds numbers. The eight-block grid near the vicinity of the initial DSJ slot and plenum design shown in Fig. 23 consisted of 40,083 points. An unsteady normal velocity boundary condition was implemented at the wall of the plenum to represent the DSJ piston. At a low angle of attack, velocity magnitude contours are shown in Fig. 24 during the in-stoke and out-stroke of the DSJ. During the in-stroke, significant losses occurred in this initial design when the jet dumps into the plenum. The CFD analysis was then used to guide improvements in the internal DSJ geometry and to identify preferred slot x/c locations.

The slot geometry was modified to reduce losses by increasing the internal radii, as shown in Fig. 25. The slot location was also varied to improve the effectiveness of the DSJ. For the ramping airfoil, it was found that choked flow could occur during the in-stroke cycle of the DSJ at the higher angles of attack. While DSJ slots at different locations were similarly effective for a given momentum coefficient ($C\mu$), moving the slot further aft reduced the wall-oscillation of the DSJ actuator piston required to achieve this momentum coefficient. This occurs even for a moderate freestream Mach number of 0.3 because of the local leading edge supersonic flow region that occurs at high angles of attack. This effect is not seen at M=0.1 or 0.2, because supersonic flow is absent at these Mach numbers. For relevance to rotorcraft, a Mach of at least M=0.3 should be studied. The DSJ slot was moved further aft to increase the flow through the DSJ slot. In Fig. 25, the DSJ flow amplitude during the airfoil ramp is shown normalized by the initial DSJ amplitude. The slot placed closer to the airfoil leading edge (x/c=0.05) experienced much more reduction in the DSJ airflow. This is due to the local supersonic flow. Force coefficients were also computed for a sinusoidal blade pitching oscillation. The benefits were similar to the ramping case.

The DSJ slot design was then modified by adding a region of increasing area to provide in-stroke diffusion and reduce losses. In Fig. 26, flow vectors and pressure contours are shown in the DSJ slot at the time of maximum in-stroke velocity. The

contours show that pressure is recovered in the slot diffuser, increasing the efficiency and effectiveness of the actuation system. Figure 27 shows the slot design implemented for the wind tunnel model. The exit slot is 0.1" (0.004c) wide, angled 20° to the surface, and begins at 0.065c.

1st Generation Actuator Performance

In-situ slot velocity measurements of the DSJ actuator performance as mounted in the wind tunnel model were taken with a hot wire probe during wind-off conditions. Figure 28 shows the power required and efficiency for the 5 actuator modules as functions of flow velocity in the slots. Two phase relationships were used: In-phase with all 5 actuators in-phase, and out-of phase with actuators 1, 3, 5 operating with reversed polarity from actuators 2 and 4. The measurements showed close to the efficiency predicted by the electro-acoustic model when neighboring DSJ actuator modules were operated out-of-phase. In-phase performance was found to be degraded due to higher than anticipated acoustic loading on the backside of the piston, which caused excessive leakage losses. The central actuator module generally operated better than the side modules, because of the increased area of its backside vents. Wind-on performance will be discussed in the following section.

Table 3 shows how the wind-off velocity measurements translate to momentum coefficient at the design condition of M=0.4. Operation at 60V excitation will satisfy the 0.1% Cμ design goal. At reduced Mach number the maximum available Cμ will increase $\sim M^{-2}$.

Table 3. Estimated DSJ authority at M=0.4, based on wind-off flow measurements

Volts	U_N (f/s)	C_μ (%)
30	128-158	0.03-0.04
40	159-197	0.04-0.07
50	189-233	0.06-0.09
60	217-268	0.08-0.12

Full Scale Blade Section Validation Experiment

Objectives

The wind tunnel experiment was designed to answer two significant questions: (1) what unsteady momentum coefficient amplitude is required to achieve significant improvements in stall characteristics at realistic conditions? and (2) can the actuation system provide this momentum coefficient within the size, mass and power constraints of a rotor blade?

Description of Experiment

The experiment was performed in February to March 2001 on a full scale, two-dimensional blade section model. The airfoil section was the Sikorsky SC2110 current technology high lift airfoil. The wind tunnel conditions matched the parameters believed to be most important to the unsteady stall process: Mach number = 0.2 to 0.4, Reynolds number = 3-5x10^6, and unsteady pitching motion. The model could be held fixed at steady angles of attack of 0 to 30° or oscillated at the appropriate frequencies (f ~ 2-7 Hz, $k=\omega c/2U$ = 0.05 to 0.15) and amplitudes (± 5 and 10°) using a hydraulic rotary drive. Figure 29 shows the model mounted in the 33" wide, 8' tall Two Dimensional Channel (TDC) in the UTRC Main Wind Tunnel. The 24" chord model with the DSJ actuation installed is shown in Fig. 30. The model contained 5 internally mounted DSJ actuation modules, as shown in Fig. 31. Also shown in Fig. 31, and in close up view in Fig. 32, are the shaped DSJ exit slots, and the aerodynamic instrumentation.

The instrumentation mounted inside the model consisted of 34 unsteady pressure transducers, 5 hot film sensors, 5 actuator thermocouples, and 2 actuator displacement strain gauges. Twenty-six of the unsteady pressure transducers were located along a central chordwise array and were integrated to measure lift and pitching moment, 4 transducers measured internal actuation system pressures, and 4 measured spanwise uniformity. Four of the hot film sensors were located on the airfoil surface and measured boundary layer separation and transition characteristics, and 1 sensor was located in the central DSJ slot to measure slot velocity. Additional instrumentation included a downstream wake rake to measure drag for steady state conditions, a model angle of attack sensor, and wind tunnel total and static pressure and temperature sensors. The data were digitized simultaneously at a rate of 1024 samples per oscillation cycle, ensemble averaged over 16 cycles, converted to coefficient, stored, and made available for on-line display and plotting.

The experimental period consisted of build up and checkout of the actuation and model systems, acquisition of baseline results with the DSJ exit slot taped over, operation with the slot open but not active, and operation of the DSJ actuator at a series of power levels. At Mach numbers of 0.2, 0.3, and 0.4, steady angle of attack sweeps through stall were performed, followed by unsteady motions of ±5° and 10°, about mean angles of 10° and 15°, at reduced frequencies of k = 0.04 to 0.10.

Aerodynamic Results

Pressure Distributions

Pressure distributions at steady angle of attack are shown in Figs. 33 and 34. Figure 33 shows results for 5 angles of attack at M=0.2, with the DSJ slot open but inactive. While the pressure distributions appear normal at α=10°, at α=12° a pressure plateau appears at x/c=0.1 to 0.2 on the upper surface, indicating a flow separation bubble has formed over the open slot. At α=14° the pressures are flat for x/c > 0.1, indicating substantial separation. Figure 34 shows results with the DSJ operating at 30Vexcitation in the out-of-phase mode, producing $C\mu$ ~ 0.15%. There is no separation bubble at the slot, and a strong leading edge suction peak of C_P ~ -7 is maintained through α=16°.

Unsteady upper surface pressure distributions for M=0.2, α=10°-10°cosωt, k=0.05 are shown in Fig. 35. Results for the DSJ slot taped over are in the upper left. Each curve is for a separate pressure transducer. The leading edge transducer (x/c=0.005) is at the bottom, with its scale on the right. The results are characteristic of dynamic stall, with a smooth increase in suction to a strong leading edge peak of C_P~ -8.5, followed by a sudden loss of suction over the forward 10% of chord, convection of a stall vortex (shown by a compact suction pressure valley) towards the trailing edge, several post stall oscillations, and then reattachment. With the DSJ slot open but not activated (shown in the upper right), suction begins to collapse near the slot at x/c=0.06 to 0.08 by α ~ 12°, and the suction peak is terminated 3° early when it reaches C_P~-5. Activating the DSJ at 20V, Cμ ~0.01 (shown in the lower left) delays stall and increases suction, but not back to the baseline values. Only at the higher excitation of 60V, Cμ ~ 0.4% (shown in the lower right) does the peak exceed the baseline level and last to a higher angle before collapse. At this excitation level there are additional benefits in that the convected stall vortex appears weaker, and reattachment at the leading edge occurs sooner, at α ~15° versus ~10° for the baseline.

Unsteady pressures at M=0.3 (Fig. 36) show similar trends, but since the maximum applied DSJ excitation of 60V only produces Cμ ~ 0.2% here, the leading edge suction levels and angle at stall did not fully recover to the baseline levels. At M=0.4 (Fig. 37) the leading edge suction pressures are less affected by the open slot, but DSJ actuation up to 60V (Cμ ~ 0.1%) did not seem to provide any substantial enhancements.

Aerodynamic Loads

Figure 38 shows steady lift and pitching moment results for M=0.2. The black circles are with the DSJ slot taped over. The blue squares are with the slot open, but with the actuators not active. As anticipated from the steady pressure distributions shown in Fig. 33, opening the slot causes a substantial drop of 4° in the lift stall angle, accompanied by a reduction in C_L^{max}. This is a larger effect than was anticipated based on the slot size (0.4% of chord), pretest CFD results, and previous experience with disturbances on other airfoils. Operating the DSJ actuators (Cμ~0.15% results are shown as green diamonds) recovered the stall performance and produced a net improvement over the taped slot baseline of +6°stall angle and +6% C_L^{max}. This was however less than the objective of +5° angle, +10%C_L^{max}. The pitching moment results show somewhat smaller changes in the moment stall angle, from α=15° (slot taped), to α=13° (slot open), to α=17° (Cμ = .15%).

The lift results for unsteady pitching motion exhibit similar trends, as shown in Fig. 39. Lift hysteresis loops are shown at the left for M=0.2, α=10°±10°, k=0.07. Opening the slot with the DSJ off causes a 2 to 3° earlier stall than the baseline. This is accompanied by a reduction in peak C_L. Activating the DSJ actuation recovers and slightly improves on the baseline stall angle and peak C_L, but the available levels of Cμ (up to 0.4%) were unable to provide the planned level of improvements. The actuation does make a substantial improvement in post stall lift; at Cμ~0.4%, the post stall C_L is increased by 0.6, to 160% of the baseline. Lift hysteresis loops for M=0.3 are shown at the right of Fig. 39. The M=0.3 behavior is similar to that at M=0.2, but while the

activated DSJ is able to recover the baseline stall angle, it is unable to fully recover C_L^{max} at the maximum available Cμ of 0.2%.

Unsteady pitching moment results at M=0.2 and 0.3 are shown in Fig. 40. The M=0.2 taped slot results (the upper plot) show a strong negative pitching moment peak of C_M~-0.35, characteristic of the response to convection of a strong dynamic stall vortex past the trailing edge. The slot-open results show an earlier increase in pitching moment caused by the earlier stall, but the moment does not reach the same peak because the stall vortex does not get as strong. Results with the DSJ active show increasingly narrow peaks, but of decreasing strength. At 60V (Cμ~0.4%), the peak has been reduced by over 40% from the baseline level. This is a positive benefit, since pitching moment peaks generate the vibratory control loads that let stall boundaries. Results at M=0.3 (the lower plot) show a similar trend, but the maximum reduction in pitching moment peak is only 10% at the maximum available Cμ of 0.2%.

Actuation System Performance

Actuation system performance and diagnostic information during wind-on running were measured using the suite of velocity, displacement, temperature, pressure, and power sensors shown in Fig. 41. A surface hot film gage was mounted in the DSJ slot to determine exit velocities. The concept was to calibrate the hot film sensor against the hot wire traverse data taken wind-off, and then use the surface film by itself wind-on to quantify actual forcing levels. The top plot in Fig. 42 shows surface hot film gauge output versus sample number (time) during a wind-on blade pitching condition. The middle plot shows the leading edge cavity pressure (clearly showing the forcing frequency of 260 Hz) and the bottom plot shows the blade pitch angle. Initially, the surface gauge indicates oscillation at the expected 260 Hz, with a larger amplitude initial peak and a lower second peak. (The waveform is rectified by the flow direction insensitivity of the hot film.) This waveform was very similar to that obtained during calibration. However, as the pitch angle increased, the waveform changed to a single peak with much larger amplitude. Post-test CFD replicated some of this behavior. It appears to be caused by a strong vortex that develops during the instroke and induces an internal reverse flow near the hot film gauge during portions of the outstroke. Visualization of this vortex is also shown in Fig. 42. This and other factors made it difficult to extract wind-on forcing levels from the surface gauge.

An alternative approach to determine the wind-on forcing level was to use the cavity pressure amplitude and actuator power consumption measurements. Figure 43 shows these measurements versus actuator coil voltage at Mach 0.2, 0.3,and 0.4. There is little observed effect of Mach number, particularly in the power consumption. Power consumption has been observed during bench top testing to be quite sensitive to resistance changes in the slot, so the lack of observed changes in power implies that slot resistance did not substantially increase with Mach number. Figure 44 shows the variation in cavity pressure during one cycle of a pitching motion. The amplitude at the forcing frequency of 260 Hz varied little, even during dynamic stall (samples 600 to 1050). Hence, it was concluded that the wind-off measurements provide a good estimate of the wind-on forcing levels.

The actuators were not adversely affected by wind tunnel environment. The 10° amplitude, 2-5 Hz pitching motion generated up to 2 g of alternating acceleration normal to the actuator motion axis. This had no observed effect on the operation, as measured by the cavity pressures, and the displacement (strain) measured by strain gauges on two springs. Steady and unsteady pressure differences of up to 5 psi were introduced across the actuator piston because the front was vented to the slot on the suction surface and the rear was vented to the aft portion of the airfoil. Since the actuator had high stiffness, these pressure differentials did not cause significant deflections, and did not affect operation.

Heat transfer calculations predicted that sufficient radiative and advective transfer would occur across the thin gap between the coil and the surrounding magnet to maintain a safe operating coil temperature at power levels above the manufacturer's recommended steady state limit without use of active cooling. Thermocouples monitored operating temperatures, which remained below 120? F at the maximum power condition (70V excitation), consuming 250W per coil. A second reliability issue was fatigue of the lead wires from the moving coil. Proper strain relief is required. A more serious issue was fatigue cracks in two of the springs. One occurred during pre-test checkout, and was traced to propagation of a surface crack from initial machining. The set of operational springs was treated by shot peening to minimize this risk. The second failure occurred during maximum power operation at the end of the test. It was traced to a 10% reduction in material strength of this spring caused by insufficient heat treatment. The root cause was a reduction in the design margins for these springs relative to the earlier benchtop prototypes. Future springs should be designed with a 10-20% increase in stress margin, and inspected to verify material properties before machining.

Conclusions from Wind Tunnel Experiment

The DSJ actuators met their design goal of 0.1% Cμ at Mach 0.4 using an internal system, and The system increased the steady and unsteady stall angles, increased the steady C_L^{max}, increased the post-stall CL in unsteady motion, and reduced the strength of the unsteady pitching moment during dynamic stall. However, the loss in stall performance caused by the adding the open DSJ slot to the SC2110 airfoil was too high to permit the DSJ actuation to provide the desired net performance improvements of 5° steady and unsteady stall delay and 10% increase in steady C_L^{max}. Substantial benefits appear to require at least 0.4% Cμ, and perhaps as much as 1%.

The pre-test slot design effort emphasized improving the internal flow in the slot to maximize actuator authority, but did not pay enough attention to the effect on the external flow. Additional computational slot design studies were conducted after the experiment (as described in the following section) to try to identify a workable compromise between maximizing actuator efficiency and minimizing the effect on the airfoil characteristics. A revised actuator design was also generated to try to address back end acoustic and centrifugal loading issues and achieve higher authority.

Airfoil and Actuation System Computation

Airload Prediction and Comparison with Experiment

The CFL3D Navier-Stokes analysis used for these computations has been used previously for many applications. For airfoil stall prediction, comparisons were made for steady and unsteady stall. In Fig. 45, the lift coefficient versus angle of attack is shown for steady flow, using two turbulence models. The analysis predicted the maximum lift coefficient and stall point quite well. Dynamic stall is much more difficult, as the analysis must predict the unsteady flow separation, release and convection of the stall vortex, and the unsteady reattachment of the flow (for sinusoidal pitching motion conditions). Turbulence models are still lacking high-accuracy for such complicated unsteady flows. For some conditions, the analysis does not do very well, in particular for oscillation in which the airfoil is on the verge of stall; missing the stall angle can produce drastically different results. Conversely, for pitching motions in very deep stall, the flow experiences very large separated regions, and may not reattached until low angles of attack; this produces strong hysteresis effects that are difficult to capture. For cases in between these two extremes, the analysis may do much better. For example, unsteady lift coefficients are shown compared with experiment in Fig, 46, for M=0.3, $\alpha=10°+10°\sin\omega t$, and k=0.07. This is considered to be good correlation for dynamic stall. Fortunately, this Mach number, reduced frequency, and angle of attack range is representative of conditions experienced by a rotor blade section. This was used as the baseline condition to assess DSJ effectiveness for dynamic stall control.

Exit Slot Redesign and Repositioning

The experiment revealed a loss in lift when blowing is turned off caused by presence of the slot. CFD analysis was used to try to recover the lift by redesigning the slot geometry. Figure 47 shows steady C_L vs angle of attack for no slot, for the original 20° slot, and for two variations with the slot at 45° to the surface. The 45° slots recovered some of the stall angle and C_L^{max} reductions. The slot geometry was then parameterized using the key design variables shown in Fig. 48. This enabled automatic grid generation and efficient parametric studies. The grid is also shown in Fig. 48. With a redesigned slot that reduces the blowing-off lift-loss, many variations were performed to find the best configuration for improving dynamic stall characteristics. With low-levels of blowing (C_μ~0.1%) the peak lift coefficient could not be improved for the sinusoidal pitching case of 10 +/- 10°. However, the post-stall behavior can be improved by increasing the post-stall lift and reducing the peak drag and pitching moments. Figure 49 show baseline, DSJ-on ,and DSJ-on, averaged over the DSJ oscillation period. In Figure 50, the maximum lift coefficient is plotted versus the minimum pitching moment. This is one method for summarizing airfoil effectiveness for dynamic stall, since a design that increases maximum lift coefficient may also introduce a pitching moment penalty and therefore not necessarily be better. An improved design would provide higher lift coefficient for the same or lower pitching moment. Both experimental and computational points are provided in this plot for various Mach numbers, ramping rates, and blowing levels. To date, only higher levels of blowing ($C\mu \sim 0.3\%$) have been shown to be able to shift this trend curve favorably by a substantial margin.

For further parametric studies, an average lift metric was constructed for dynamic stall effectiveness. Using C_L^{max} as the metric can be misleading for several reasons. First, as discussed above, the higher maximum lift coefficient during dynamic stall may be due to a more severe stall, and hence larger pitching moment and drag penalty. Secondly, the peak lift coefficient is short lived and doesn't necessarily provide a good measure of the increased lift of the rotor. The post-stall behavior influences the rotor lift as well, and the post still lift can occur at higher dynamic head, providing more lift to the rotor. Parametric studies were performed on both a high-lift airfoil (SC2110), and an airfoil that provides lower drag at higher Mach numbers (SSCA09).

As a measure of the improved lift over the entire cycle, the $\overline{\Delta C_L}$ metric was constructed based on the change in average lift coefficient over the entire cycle using the DSJ relative to the baseline airfoil.

$$\overline{\Delta C_L} = \oint_{\alpha} \Delta C_L d\alpha \Big/ \oint_{\alpha} C_L d\alpha, \quad \Delta C_L = C_{L,DSJ} - C_L \qquad (1)$$

Detailed parametric studies were performed for position and angle of upper surface slots on the SC2110 and SSCA09 airfoils. These two parameters were found to be the most critical for a given momentum coefficient. A schematic diagram is shown in Fig. 51 of the upper surface slot on the SC2110. Note the definition of X_S for the slot position: a value of –0.25 corresponds to the leading edge, and a value 0.0 is at the quarter-chord. Hysteresis loops for lift, drag and moment are shown in Fig. 52 for various slot positions (40 deg slot angle and average unsteady blowing of $C\mu Avg=0.13\%$[1]). The upstroke behavior of the force coefficients is relatively independent of the slot position. Starting at the location of –0.184, the post-stall behavior tended to improve (an increase in post-stall lift with a decrease in post-stall drag), as the slot was moved aft. Relative to the baseline airfoil with no slot, there was a loss of lift during pitch-up, but a gain in lift during the pitch-down (post-stall). In Fig. 53 the $\overline{\Delta C_L}$ metric is plotted versus slot location and angle. The contributions to this metric during the pitch-up and pitch-down motions are shown, along with the net value. There is an optimum near $X_S = –0.14$ (x/c=0.11) which provides about a 20% increase in the $\overline{\Delta C_L}$. At this location, $X_S = -0.174$ (Fig. 53), and other positions (not shown), the results were relatively insensitive to slot angle. This can also be seen in Figure 54, where a contour plot for the $\overline{\Delta C_L}$ metric is shown versus slot angle and slot position. The contour plot identifies the optimal configuration for these two design parameters for this Mach number, momentum coefficient, pitching motion, and airfoil as a slot angle of 20 to 25° and a slot position of X_S=-.14 to -.15 (x/c=0.10 to 0.11).

The effects of different unsteady blowing levels on the SC2110 are shown in Figs. 55 (C_L, C_M, and C_D vs α) and 56 ($\overline{\Delta C_L}$ versus $C\mu$). Clearly, the unsteady blowing levels have a strong effect on the post-stall behavior. At $C\mu$ ~0.55%, $\overline{\Delta C_L}$ reached a maximum value of +90%, but there was again little effect during pitch-up prior to stall.

[1] $C\mu_{avg}$ is the average of the unsteady amplitude of $C\mu$ over the airfoil oscillation period

In Figures 57 and 58 the results of varying slot position and slot angle on the SSCA09 airfoil are shown. Again, the effectiveness of the slot was improved by moving it downstream. However, once moved downstream of $X_S = -0.16$ (x/c=0.09) the lift metric did not show further improvement. Figure 58 also shows that variations in the slot exit width did not have a significant effect. Contours of $\overline{\Delta C_L}$ versus slot position and slot angle are shown in Fig, 59. The optimum values were close to the optimum for the SC2110: a slot angle near 20° and a slot position of *Xs* = -0.155 (x/c=0.095).

Constant pitch rate ramp motions can be used to identify stall delays and airload overshoots without the complications introduced by the varying pitch rate caused by sinusoidal motion. Figure 60 shows ramp results at Mach 0.2 and 0.3 at a moderate rate of A=0.01. At low momentum coefficients of Cμ< 0.3% there are no substantial stall delays, and the lift, moment, and drag overshoots are slightly lower than for the baseline. At M=0.2, high levels of Cμ (1% to 1.4%) cause stall delays of up to 5° and modest increases in pre-stall lift. At M=0.3, Cμ levels up to 0.6% do not create substantial load changes or stall delays.

The effects of unsteady blowing levels on the stall behavior of the SSCA09 airfoil in sinusoidal motion are shown in Fig. 61. For this condition, $\overline{\Delta C_L}$ reached a maximum value of +65%, but there was again little effect during pitch-up prior to stall. In Fig. 62 the instantaneous blowing levels are shown versus angle of attack for increasing and decreasing pitch at four levels of Cμ. Slightly higher Cμ levels occurred near stall at the maximum angle of attack. The non-sinusoidal waveform of Cμ reflects its U^2 dependence

Alternative Separation Control Slot Configurations

In addition to blowing on the upper surface, the computational study examined having DSJ slots on the lower surface, blowing toward the leading edge. Again, variations in slot position, slot angle, and unsteady blowing levels were performed. The optimal location was found to be as close to the leading edge as possible at low slot angles (20 deg). These results are summarized in Figures 63-65. The maximum increase in $\overline{\Delta C_L}$ was +15% for Cu=0.13%, a lower value than that produced by an upper surface slot (Fig. 60), and still caused primarily by recovering post-stall lift.

A double slotted configuration was also studied, with the lower surface slot in the optimal position found from the lower-surface blowing study. The upper surface slot location and unsteady blowing levels were varied for the double-slotted configuration. In Fig. 66, the results are shown for unsteady blowing levels of 0.13% for each slot. There is no added benefit of two slots over one slot with twice the blowing. Based on the lift measure, the improvement was 33% versus a value of about 37% for a single slot with 0.26% blowing (Fig. 60). In Fig. 67, the effect of increased blowing levels is shown. The average lift improvement from the double slot reaches $\overline{\Delta C_L}$ = +140% for the high blowing level of Cμ=0.59% for each slot. This increase is still largely from post-stall lift recovery, but there is also an 8% increase in peak C_L before stall.

Summary of Computational Results

The post-test computational study has shown that moving the slot aft from x/c~7% to x/c~10% to 11% at 20° slot angle can improve post stall lift recovery and thereby increase the average lift coefficient during a sinusoidal pitching motion. Reducing the width of the slot and increasing the slot angle to 45° reduced the DSJ-off stall penalty, but also reduced the DSJ-on post-stall lift increase. Significant improvements in average lift coefficient required Cμ greater than 0.5%. No combination of single upper surface or lower surface slots or double slots on both surfaces using momentum coefficients less than Cμ~0.5%was found that substantially improved pre-stall characteristics (C_L^{max} and stall angle) for the M=0.3, $\alpha=10+10\sin\omega t$ motion analyzed.

2nd Generation DSJ Actuation System

2nd Generation System Design

The 2nd generation actuation design path has the goal of improving actuator performance metrics (efficiency and authority), eliminating the problematic backside acoustic loading, and developing a more realistic rotor embodiment (centrifugal load tolerant and reduced part count). Reorienting the axis of the motor along the span, as shown in Fig. 68, allows these improvements to be achieved. Though this orientation limits the forcing to being periodically out-of-phase across the span, this arrangement provides better control of piston-to-slot area for improved impedance matching, greatly reduces backside side acoustic loading, removes the need for vent passages, and eliminates mean flow leakage across the actuator piston. Further, the single motor per piston arrangement will reduce the chance of other piston modes (other than planar) being excited, and alignment of the actuator axis with the centrifugal load of a spinning rotor blade is more realistic, since a voice coil offset can compensate for mean deflection caused by g load.

In order to better optimize the 2nd generation system, a simplified electro-acoustic model was developed which neglected all the inductive and capacitive terms. This assumption is reasonable since actuator-operating point is at resonance where the most important terms of this sort cancel each other. This assumption enables rapid analysis for a given design point (C_μ) so that parameter maps of slot length and piston size can be plotted, allowing the optimal piston size for correct impedance match and maximum slot length within motor power and stroke capacity to be rapidly identified. Figure 69 shows the full lumped acoustic model (a) and the approximate resonant model (b). An example analysis from this model in shown in Fig. 70 which gives the performance for five different slot lengths (s = 1, 2, 3, 4, and 5 inches, or where "s" is half the total spanwise coverage) versus piston size. Actuator power and stroke limits are labeled in the figure. As can be seen by the efficiency, the optimal piston size for the longer slots is about 6 in^2. The selected design point shown is based on powering the longest possible slot (s = 4 in or 8 inches of total spanwise coverage) within the stroke limit of the actuator.

Due to the re-orientation of the motor axis, the voice-coil motor was able to be located outside the spring, making it possible to employ a larger, more efficient motor with larger power capacity. Together with a better impedance match, a single motor was

able to drive a significantly larger slot length than the original wind tunnel system (8 inches per voice-coil motor versus 2 inches). For the C_μ=0.1% design point, the number of moving parts is reduced by 4x and the weight by 2x with an improved efficiency of 2x (40%). For the C_μ=0.2% design point (twice the authority achieved by the system in the wind tunnel model), there is a 20% reduction in weight and 60% fewer moving parts than the first generation.

Figure 72 shows a 3-D CAD model of the 2nd generation bench top actuator illustrating the arrangement of the spring, coil and piston (slots not shown). Figure 73 is photographs of the actuation system with and without the outer skin/slot piece installed. Figure 74 shows the experimental results in terms of efficiency versus amplitude of the slot velocity compared with full electro-acoustic model prediction. The data is below the goal given by the blue squares which represent high quality factor (Q_M = 140 or 0.35% damping ratio) and small piston leakage (gap = 0.002 in). The actual realized quality factor was found by electrical impedance testing to be Q_M = 40 (or 1.25% damping ratio). By performing hammer impact testing with and without the magnet field assembly, the extra damping was determined to be due to eddy currents in the metal former tube of voice coil. Such losses can be readily avoided in practice by slotting the former tube in order to prevent eddy currents.

The model prediction with the actual quality factor is shown in Fig. 74 as the red triangles, which significantly reduces the peak efficiency from 37% to 23%. The remaining discrepancy between the model and the experimental results is due to a larger than desired piston gap (0.002 versus 0.015). The larger gap was needed to accommodate a slight rotation of the piston about the spring axis as the spring was deflected. This rotation is attributed to slight machining differences on the spring's two coils that leads to slightly different spring rates and hence rotation about the spring axis. In order to accommodate the non-planar piston motion, a much larger gap was needed. In practice it is believed that requiring tighter spring manufacturing tolerances would mitigate this issue. With the measured piston gap and the actual quality factor, the model and experiment are seen to agree well. Though the goal of C_μ = 0.1% was not reached with this bench top actuator, it is clear that this goal is achievable by properly managing the eddy currents and leakage gap. Model analysis also indicates with high quality factor and small leak gap, an increase authority level of C_μ = 0.2% is possible with this actuator arrangement with a slot length of s = 2 inches (4 inches spanwise coverage)

The bench top actuator was subjected to g loads by mounting it to the spin rig shown in Fig. 75. Voice coil power and sensor signal were run through a slip ring assembly from the rotating to stationary frame. Rotating speeds up to 722 RPM were tested which corresponds to a g load of 200 g's. A Kulite pressure transducer inside the piston cavity and the input power absorbed were used to measure the effect of the g load on actuator. Figure 76 shows the amplitude of cavity pressure and input power versus coil voltage amplitude for a range of g loads from 0 to 200. The data shows the pressure amplitude to be moderately reduced at the highest g loads, but only for the higher coil voltage level. The reduced performance here is believed to be due to piston touch down (which was audible during the test), caused by a loosened piston (found after disassembly and inspection). Hence, nothing fundamentally wrong was determined about the design of the actuator for operating with the g loads of the rotor environment.

Conclusions and Recommendations

Conclusions

The primary results from this study of flow separation control for rotorcraft are

1. Initial feasibility demonstrations and evaluations of aircraft system benefits and actuation technology alternatives in the areas of retreating blade stall control, airframe separation control, and enhanced flow turning showed the potential for successful application of the fluid mechanics and significant system benefits.
2. Trade studies of actuation alternatives for control of airframe separation and retreating blade stall (RBS) showed electromechanical synthetic jets to be most likely to provide the required high authority, high efficiency, and compact packaging within the program time frame of 3 years.
3. Directed Synthetic Jets (DSJ) powered by moving voice coils were developed for the full scale RBS application using a combination of lumped parameter electro-acoustic modeling and prototype design and testing. The resonant actuator used a high stiffness machined coil spring to achieve the required 0.1" displacement at 260 Hz.
4. Computational fluid dynamics (CFD) models of the combined actuator and external flows were used to design slot and internal actuator geometries that minimized loss though in flow diffusion and gradual turning.
5. DSJ actuators designed for full scale RBS control met their design unsteady momentum coefficient goal of $C\mu = 0.1\%$ at Mach 0.4 using an internal system that fits completely within the blade leading edge. The actuators produced an unsteady velocity amplitude of 250 fps through a 0.1" wide slot at 260 Hz.
6. An oscillating blade section wind tunnel experiment was conducted at full scale Mach and Reynolds numbers to determine the effectiveness of the internal DSJ actuation system. Benefits obtained included increased the steady and unsteady stall angles, increased steady C_L^{max}, increased post-stall C_L in unsteady motion, and reduced unsteady pitching moment during dynamic stall.
7. The loss in stall performance caused by flow separation at the open DSJ slot was too high to permit the DSJ actuation to provide the desired net performance improvements of 5° steady and unsteady stall delay and 10% increase in steady C_L^{max}. Substantial benefits appear to require at least 0.4% $C\mu$, and perhaps as much as 1%.
8. Additional computational design studies conducted after the experiment to try to find a more effective slot configuration indicated that post-stall lift recovery could be improved by moving the slot to x/c~0.10 to 0.11, but the studies not show substantial improvements in C_L^{max} or stall angle delay relative to the original design for $C\mu$ =0.1 to 0.2%. Alternative configurations with lower surface blowing were less effective. Dual upper and lower surface blowing became more effective at high momentum coefficient, $C\mu$ >0.5%.
9. A 2nd generation DSJ actuator design with spanwise rather than chordwise piston motion was built and bench tested to resolve problems with back side venting observed during the wind tunnel experiment, provide the ability to resist

centrifugal loads on a real rotor blade, improve efficiency and authority, improve packaging, and reduce weight. Though a combination of experiments and modeling, these goals were demonstrated.

Recommendations

The primary recommendations from this study are

1. The in-blade actuation technology applied in this project, while it advanced the capability of this technology, is currently unable to achieve the unsteady forcing levels of $C\mu = 0.5\% - 1\%$ that appear to be required to provide a substantial benefit for full scale retreating blade stall control. System complexity for high authority flow control actuation on rotating blades also remains quite high. Therefore continuation to a rotating blade demonstration is not recommended.
2. The potential benefits from retreating blade stall control remain high. If actuation technology develops to the point of robustly providing significantly higher $C\mu$ within the constraints of a rotor blade installation, or if improved understanding of the fluid mechanics provides a much more effective low authority approach, then this application should be revisited.
3. Active flow control should be kept in mind as an alternative for other rotorcraft applications such as separation-induced drag and download reduction.

Publications

Papers Published in Conference Proceedings

Lorber, P., McCormick, D., Anderson, T., Wake, B, MacMartin, D., Pollack, M., Corke, T., and Breuer, K., "Rotorcraft Retreating Blade Stall Control", AIAA Paper 2000-2475, Fluids 200 Conference, Denver CO, June 2000

Wake, B. and Lurie, E., "Computational Evaluation of Directed Synthetic Jets for Dynamic Stall Control", AHS 57th Annual Forum, Washington DC, May 2001

McCormick, D., Lozyniak, S., MacMartin, D., and Lorber, P., "Compact High-Power Boundary Layer Separation Control Actuation Development", Paper 18279, 2001 ASME Fluids Engineering Division Summer Meeting, May 2001

Florea, R., and Wake, Brian E., "Parametric Analysis of Directed-Synthetic Jets for Improved Dynamic-Stall Performance," AIAA-Paper 2003-0216, Aerospace Sciences Meeting, Reno, NV, Jan 2003.

Participating Scientific Personnel

UTRC: Peter Lorber, Duane McCormick, Brian Wake, Douglas MacMartin, Torger Anderson, Steven Lozyniak, Elizabeth Lurie, David Bombara, and Razvan Florea

Sikorsky Aircraft: Michael Pollack, Robert Moffitt.

Massachusetts Institute of Technology / Brown University: Prof. Kenneth Breuer

Illinois Institute of Technology / University of Notre Dame; Prof. Thomas Corke

No degrees were received during this period.

Report of Inventions

One patent disclosure "Compact Boundary Layer Separation Control Actuator" was filed in December 2000.

References

1. Carr, L.W. and Chandrasekhara, M.S., “Compressibility Effects on Dynamic Stall”, Progress in Aerospace Sciences, Vol. 32, pp. 523-573, 1996
2. Lorber, P.F., and Carta, F.O., “Airfoil Dynamic Stall at Constant Pitch Rate and High Reynolds Number,” *Journal of Aircraft*, Vol. 25, June 1988, pp. 548-556
3. Lorber, P.F. “Compressibility Effects on the Dynamic Stall of a Three-Dimensional Wing, AIAA Paper 92-0191, 30th Aerospace Sciences Meeting, January 1992
4. Bousman, W.G., "A Qualitative Examination of Dynamic Stall from Flight Test Data," *Journal of the American Helicopter Society*, Vol. 43, October 1998, pp. 279-295
5. Lorber, P.F., Stauter, R.C., Haas, R.J., Anderson, T.J., Torok, M.J., and Kohlhepp, F.J., “Techniques for Comprehensive Measurement of Model Helicopter Rotor Aerodynamics, 50th Annual Forum of the American Helicopter Society, May 1994
6. Koga, D.J., Reisenthal, P., and Nagib, H.M. “Control of Separated Flows Using Forced Unsteadiness” Illinois Institute of Technology Fluids & Heat Transfer Report R84-1, 1984
7. Katz, Y., Nishri, B., and Wygnanski, I., “The Delay of Turbulent Boundary Layer Separation by Oscillatory Active Control,” AIAA Paper 89-0975, 1989
8. Seifert, A. and Pack, L.G., “Oscillatory Control of Separation at High Reynolds Numbers”, AIAA Paper 98-0214, January 1998
9. Greenblatt, D., and Wygnanski, I., "Parameters Affecting Dynamic Stall Control by Oscillatory Excitation," AIAA Paper 99-3121, 17th Applied Aerodynamics Conference, Norfolk VA, 28 June-1 July 1999
10. Greenblatt, D., ”Dynamic Stall Control by Oscillatory Excitation”, PhD Thesis submitted to Tel Aviv University, November 1999
11. Ingard, U, “On the Theory and Design of Acoustic Resonators”, Journal of the Acoustical Society of America, Vol. 25, No. 6, November 1953
12. Amitay, M., Smith, B.L., and Glezer, A, “Aerodynamic Flow Control Using Synthetic Jet Technology”, AIAA 98-0208, January 1999
13. McCormick, D.C., "Boundary Layer Separation Control with Directed Synthetic Jets." AIAA Paper 2000-0519, 38th Aerospace Sciences Meeting, Reno, NV, Jan 2000

Illustrations

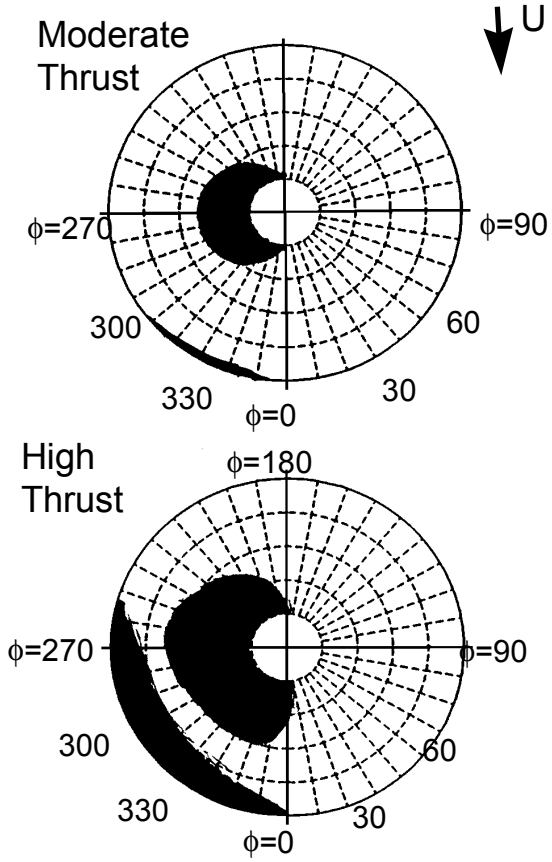

Figure 1. Measured helicopter rotor blade stall regions.

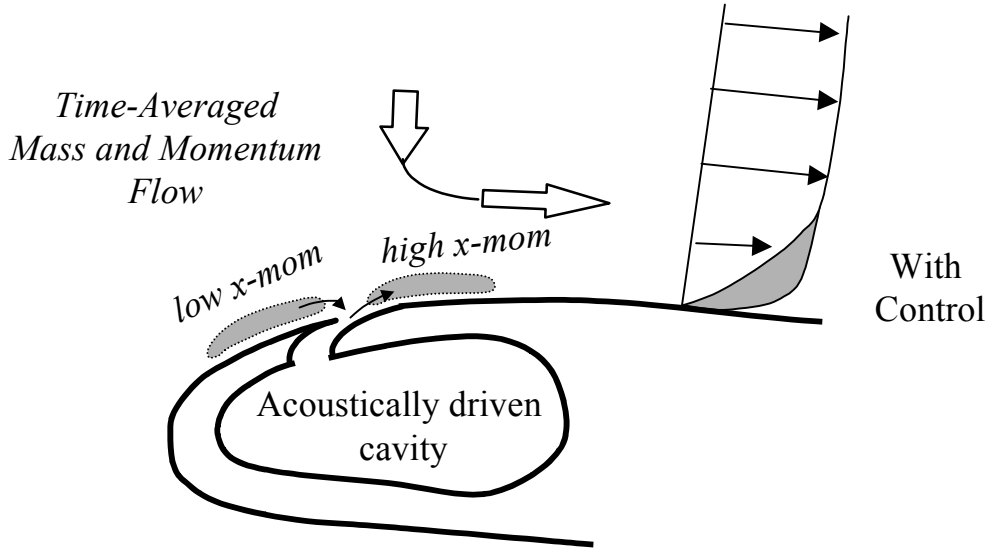

Figure 2. Directed synthetic jet separation control concept.

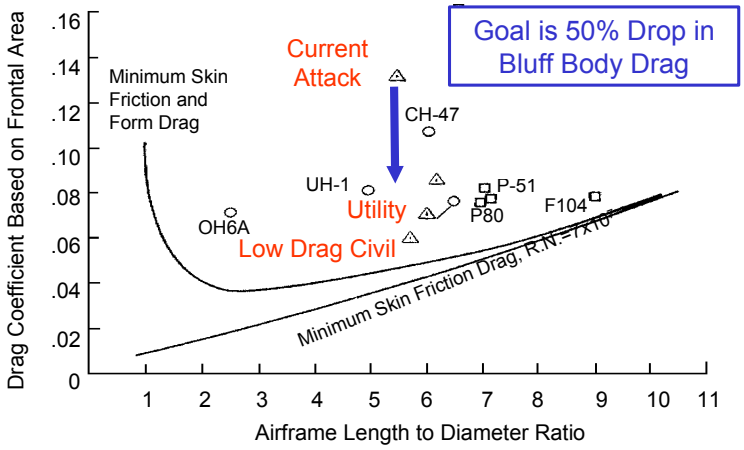

Figure 3. Airframe separation control drag reduction objective.

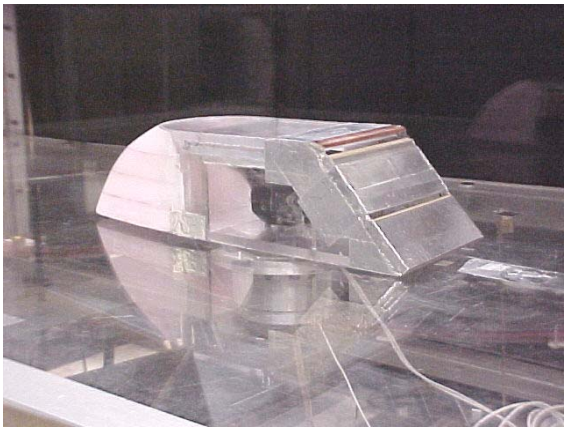

Figure 4. Small scale airframe separation control model pylon.

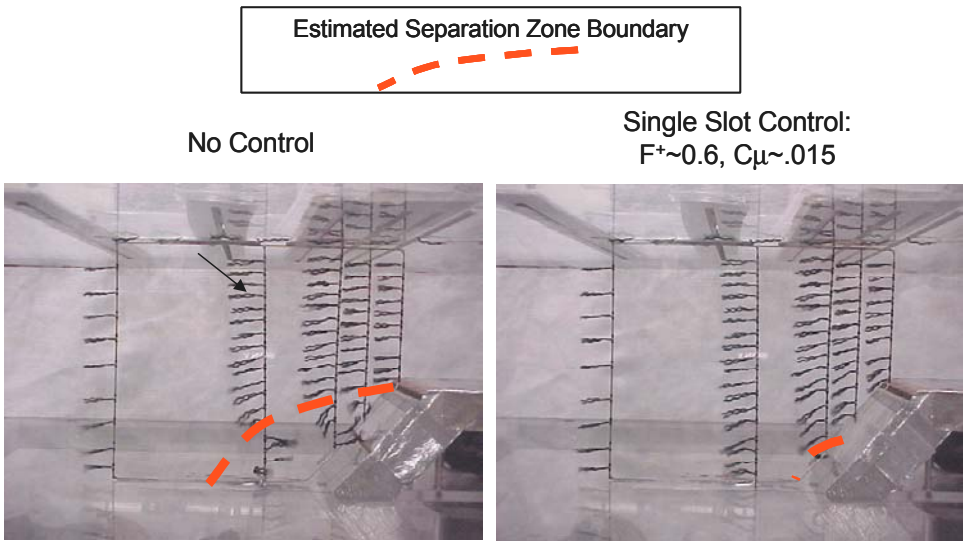

Figure 5. Reduction in separated flow area using DSJ flow control.

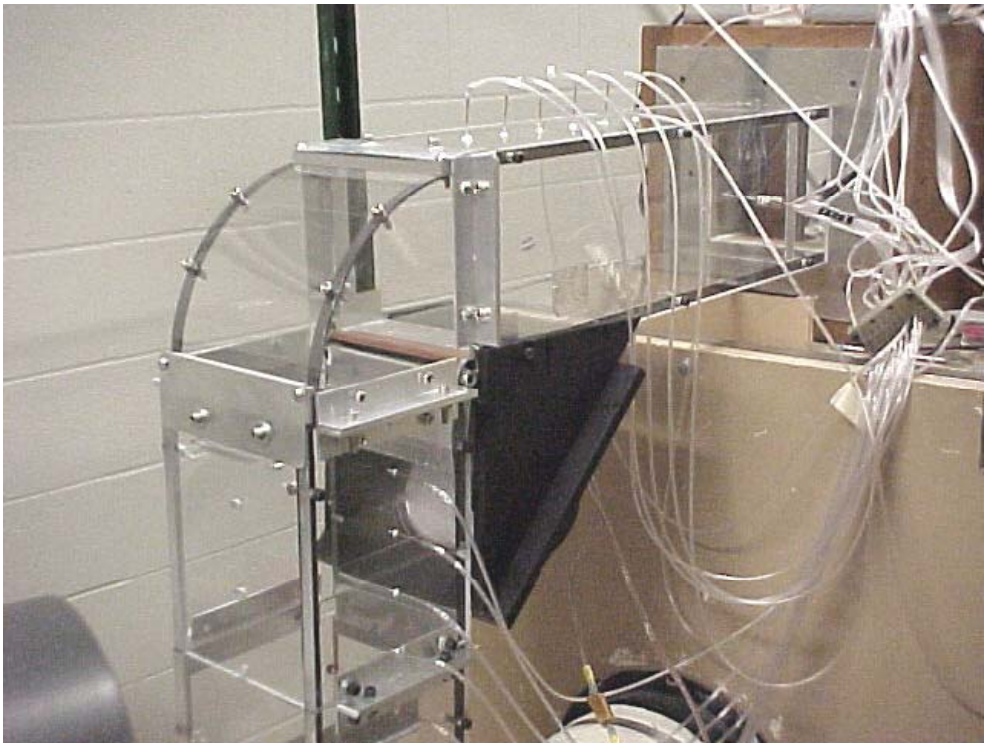

Figure 6. Internal flow turning demonstration experiment.

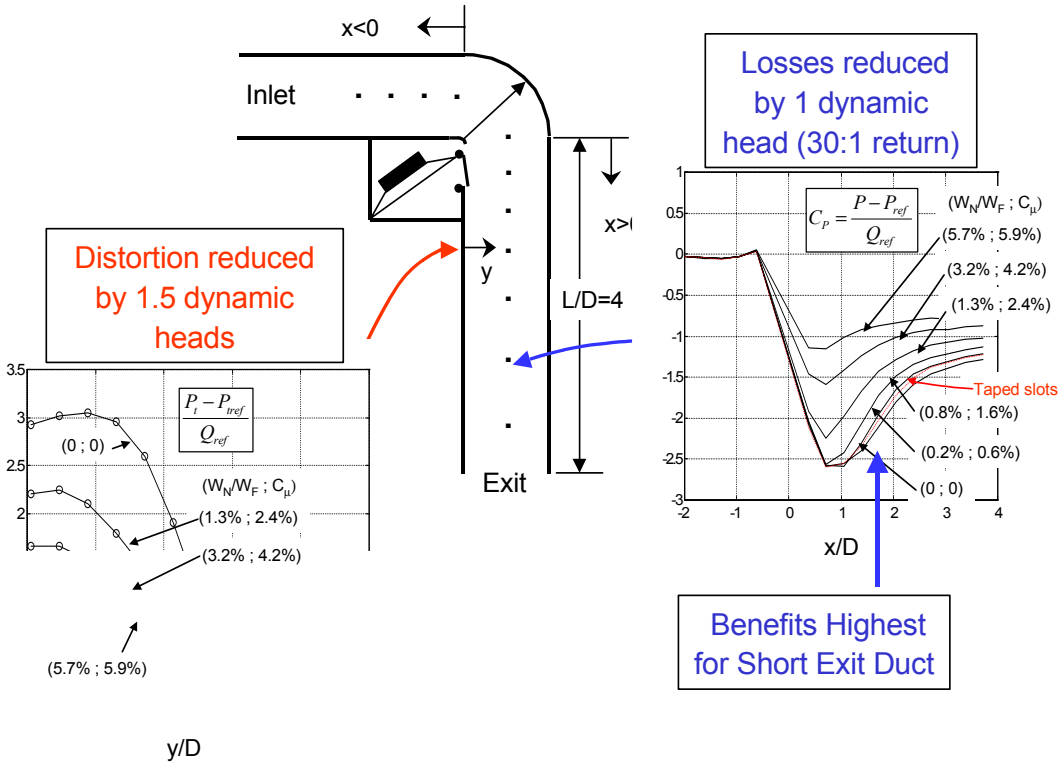

Figure 7. Internal flow turning separation control can reduce pressure losses and distortion.

Moving Voice Coil Inside Spar

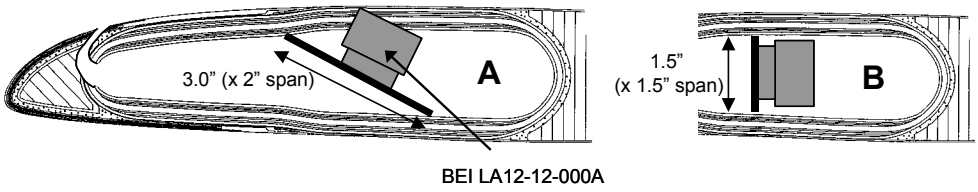

Variable Air Gap Motor

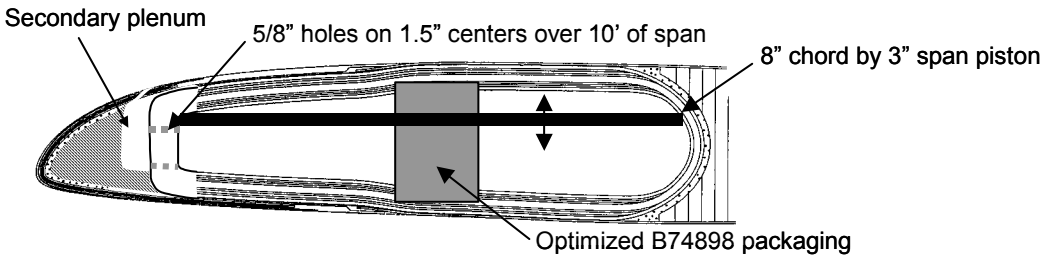

Synthetic Jet Integrated into Leading Edge

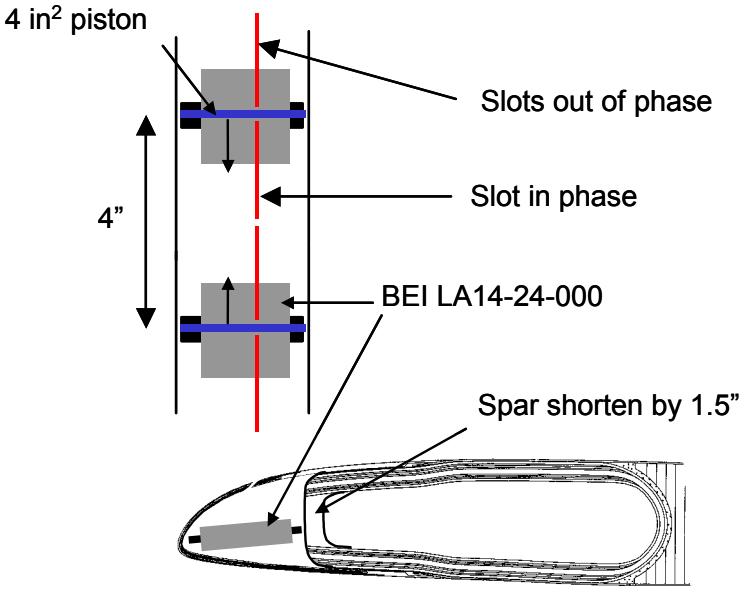

Periodic Valve

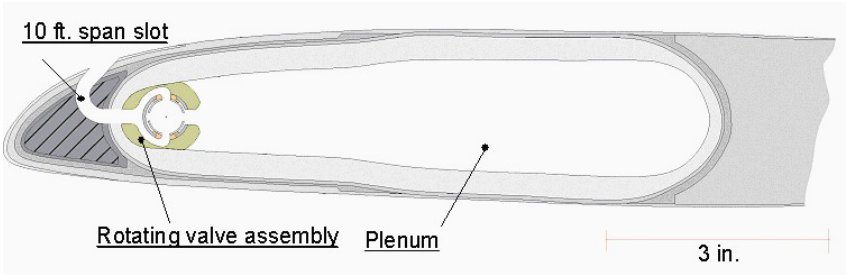

Figure 8. RBS actuation concepts examined during Phase 1.

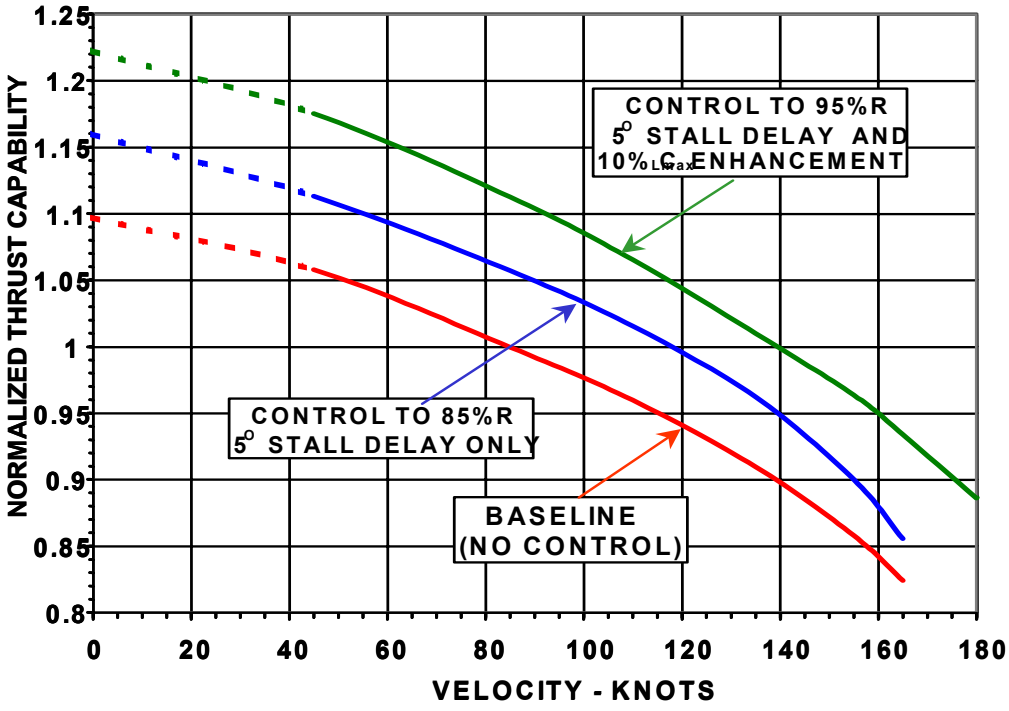

Figure 9. Impact of RBS control on normalized rotor thrust capability

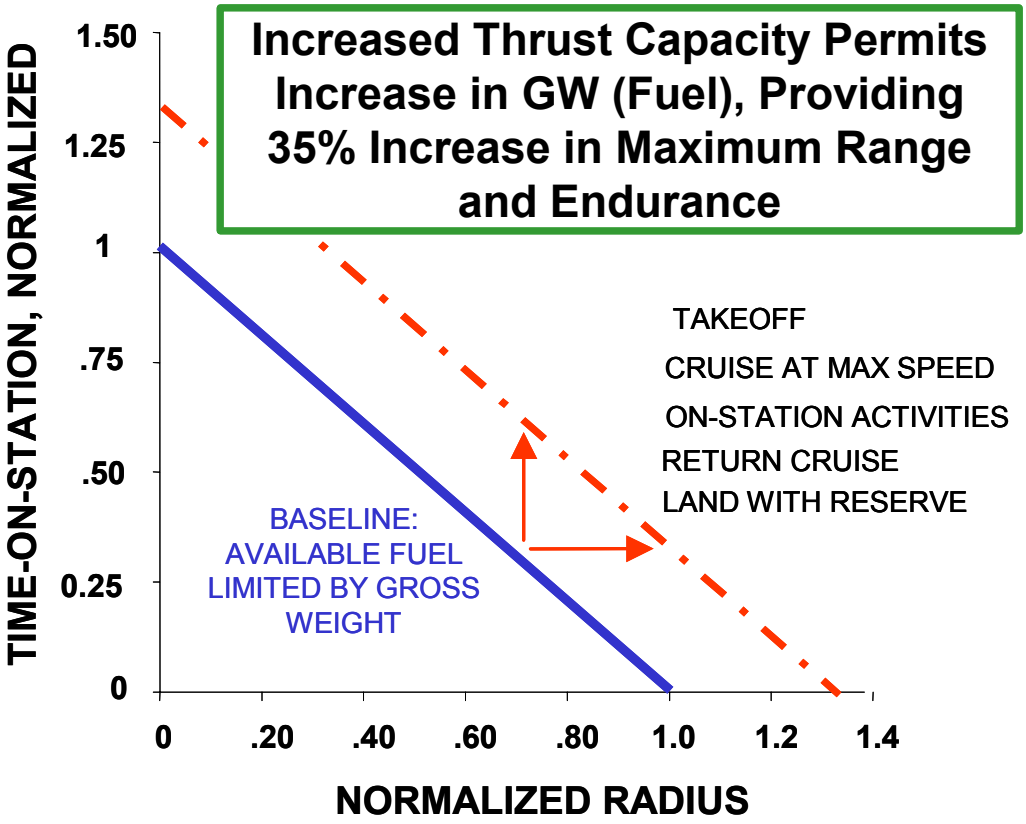

Figure 10. RBS control impact on utility mission performance

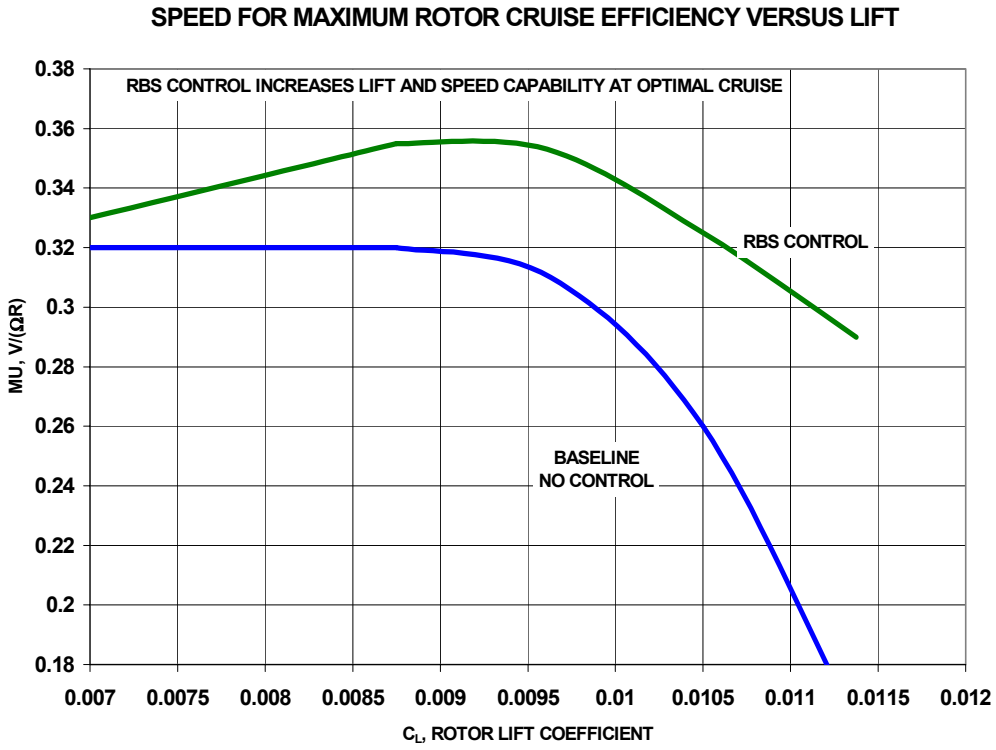

Figure 11. Speed for maximum cruise efficiency versus rotor lift coefficient.

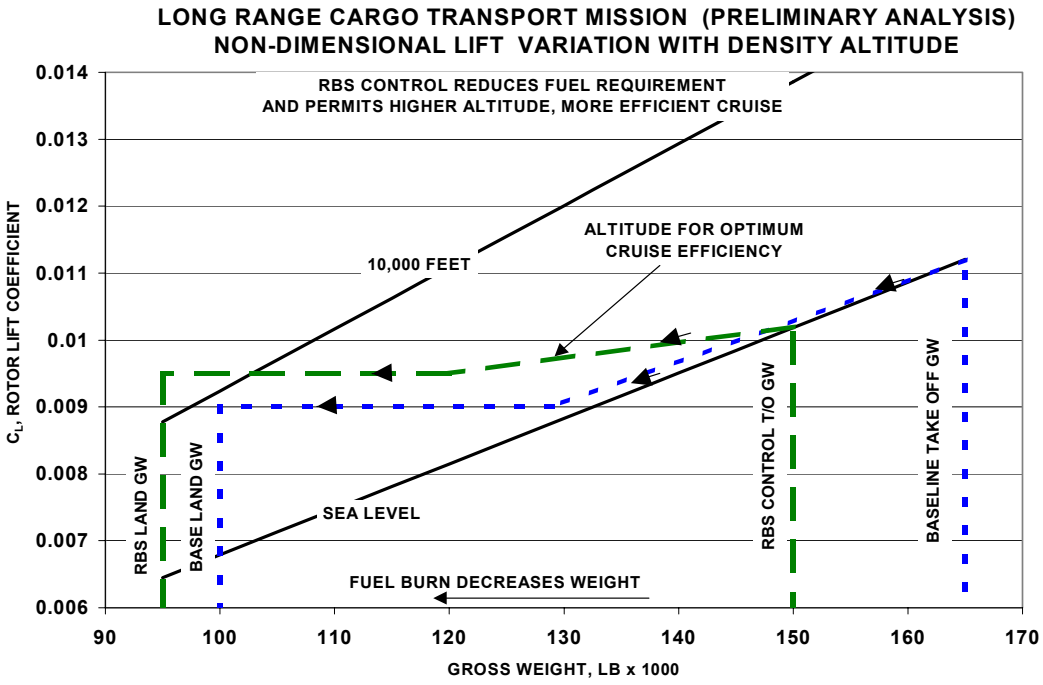

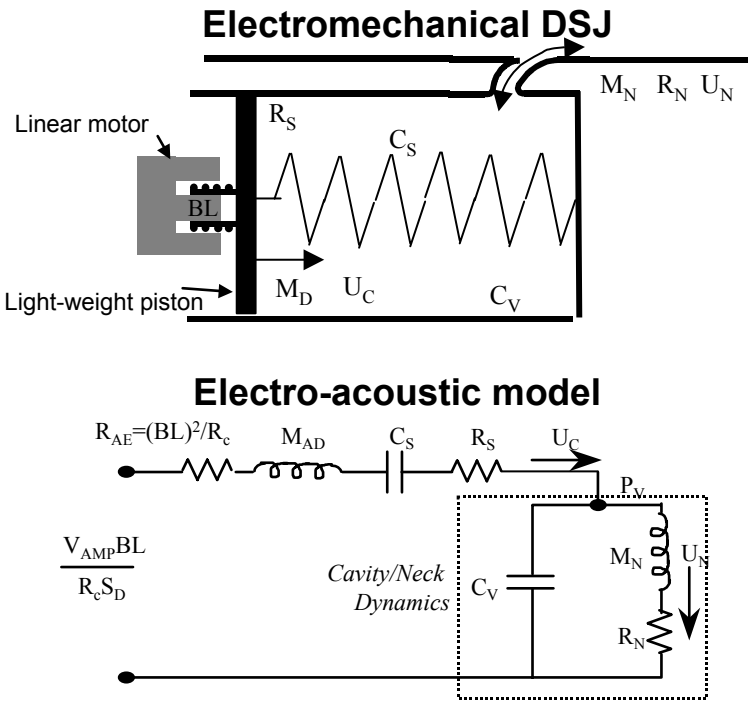

Figure 13. DSJ schematic and electro-acoustical model.

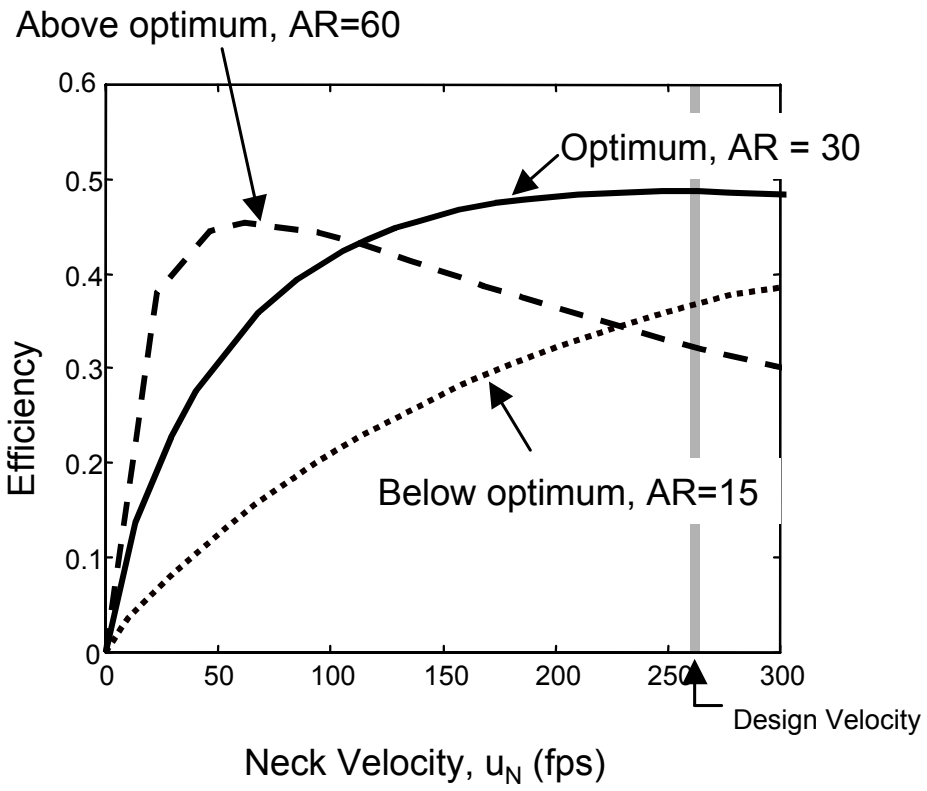

Figure 14. Example optimization study

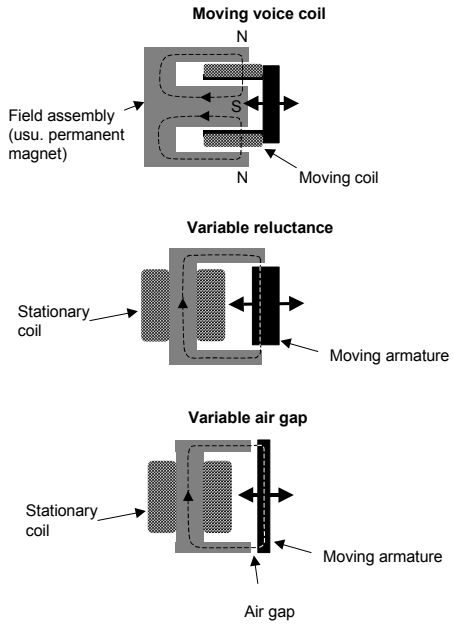

Figure 15. Three fundamental electromechanical linear motor configurations

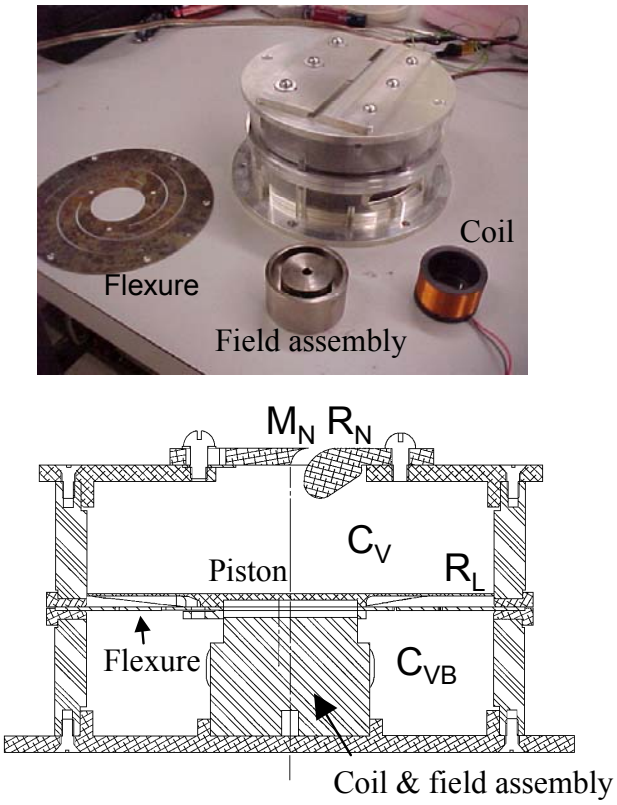

Figure 16. Initial benchtop actuator

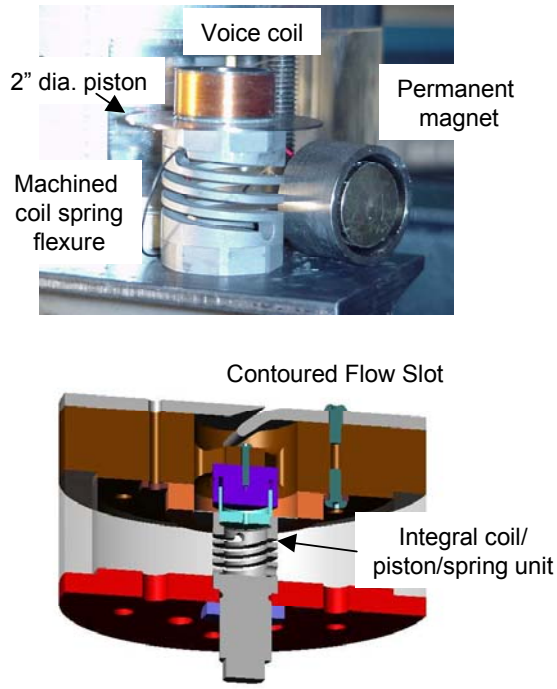

Figure 17. Benchtop prototype actuator

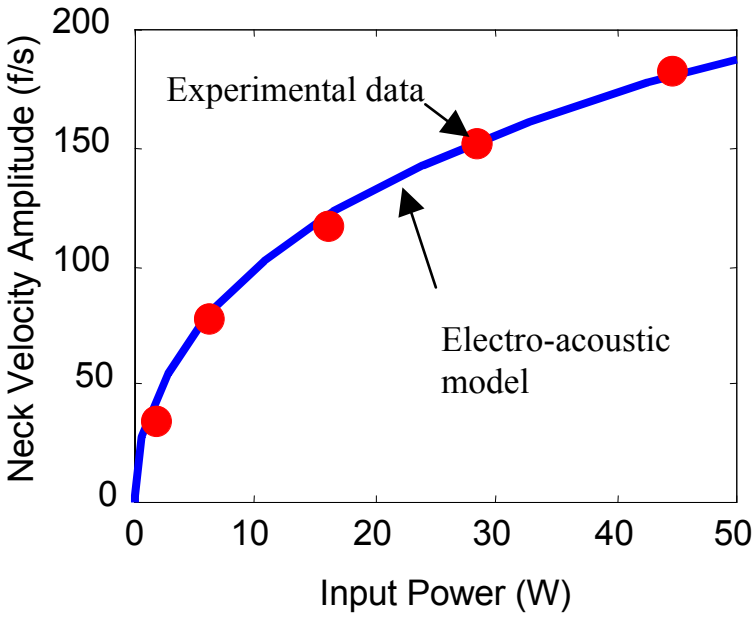

Figure 18. Benchtop prototype actuator results

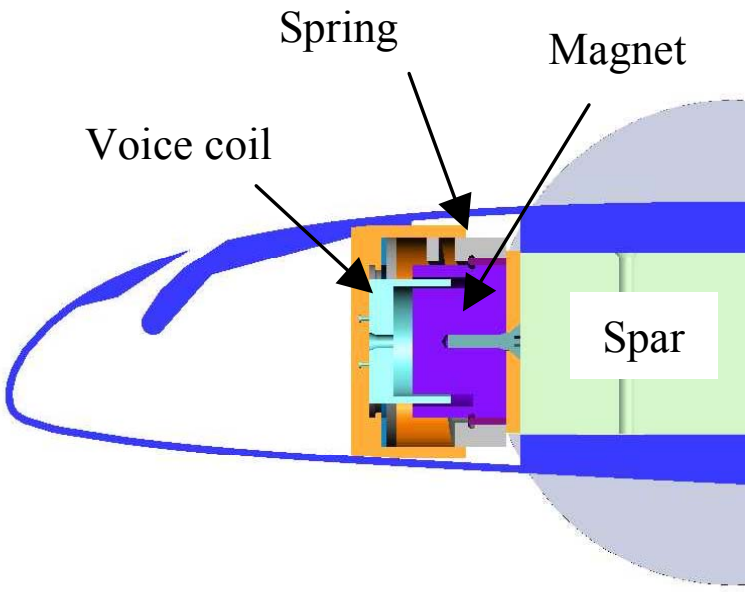

Figure 19. Compact spring/piston/motor installation for wind tunnel mode

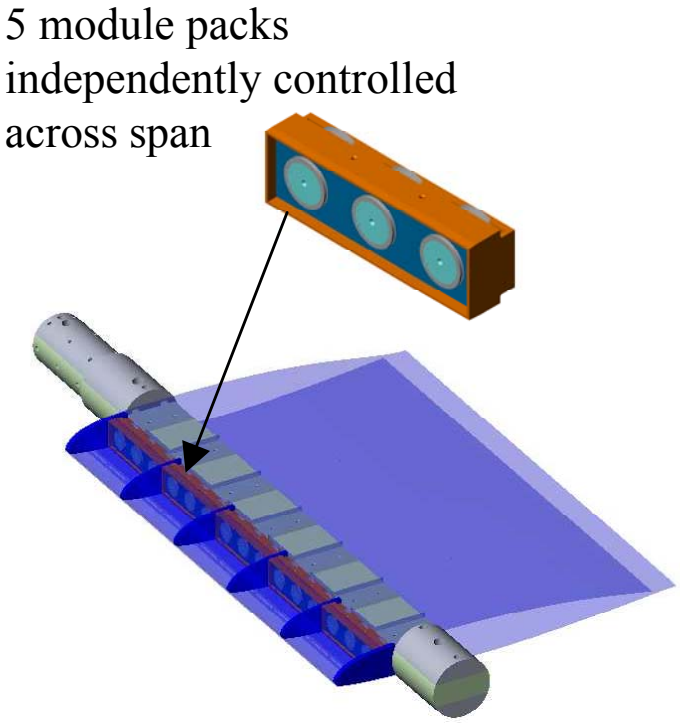

Figure 20. Finalized wind tunnel model actuator arrangement

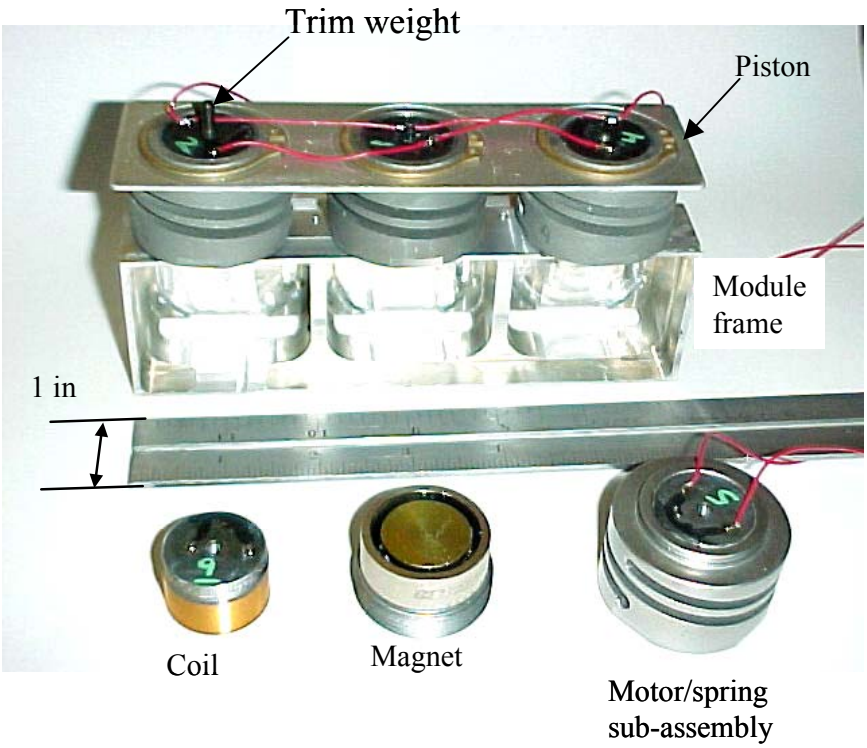

Figure 21. Disassembled actuator module and motor/spring subassembly.

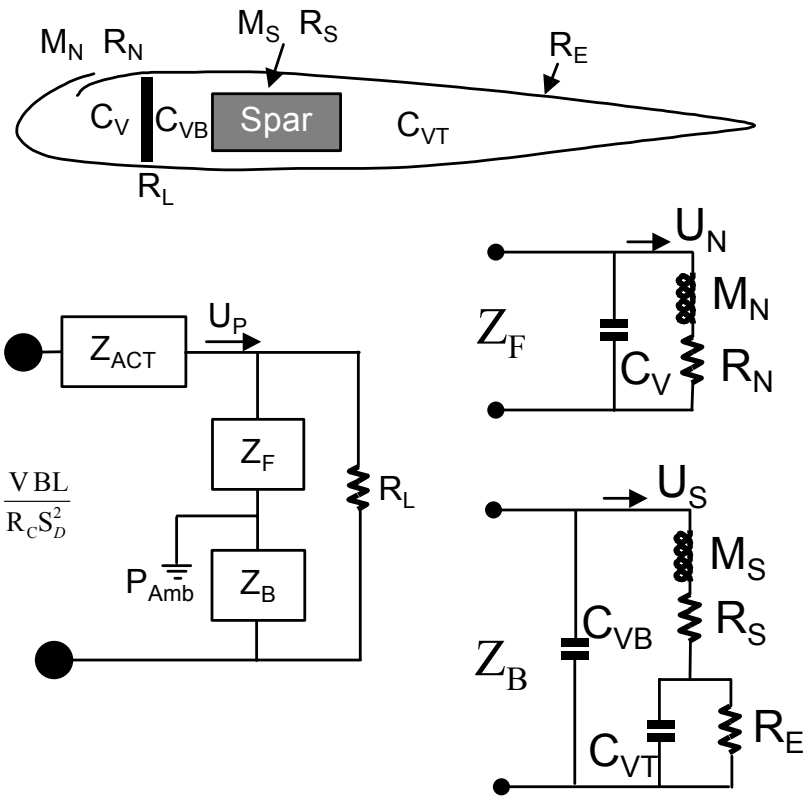

Figure 22. Electro-acoustic model of RBS actuator in wind tunnel model section

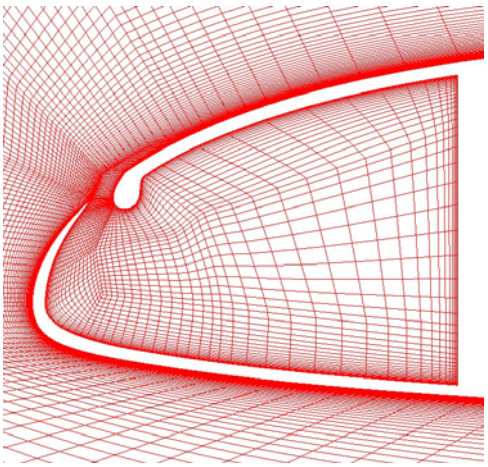

Figure 23. Computational grid in slot and plenum regions (initial design)

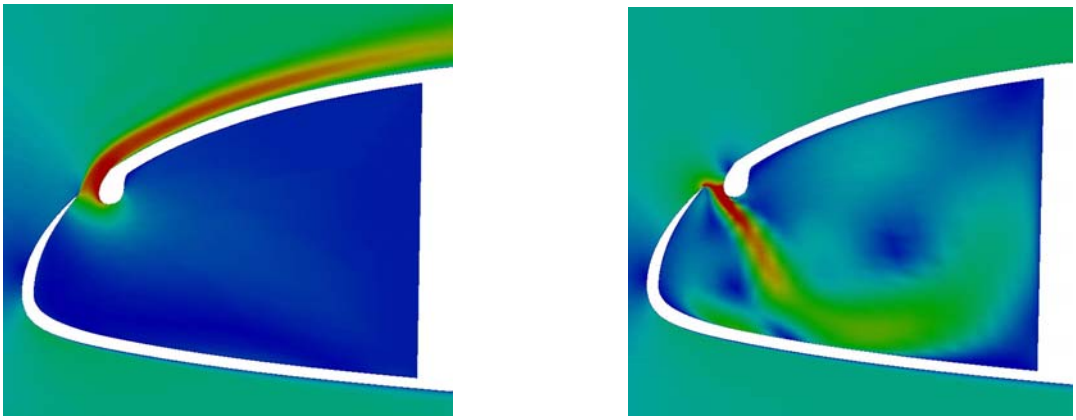

Figure 24. Velocity magnitude contours during the out-stroke and in-stroke of the DSJ

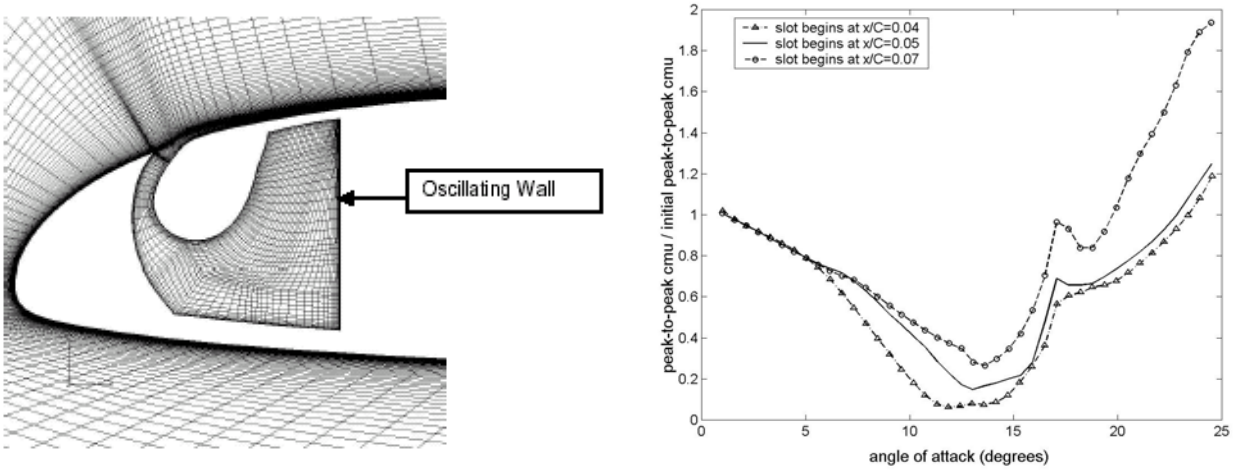

Figure 25. Modified slot geometry and amplitude of DSJ flow normalized by initial amplitude, versus angle of attack, for unsteady ramp motion at M=0.4, A=0.005. Moving the slot further aft reduced choking inside the slot.

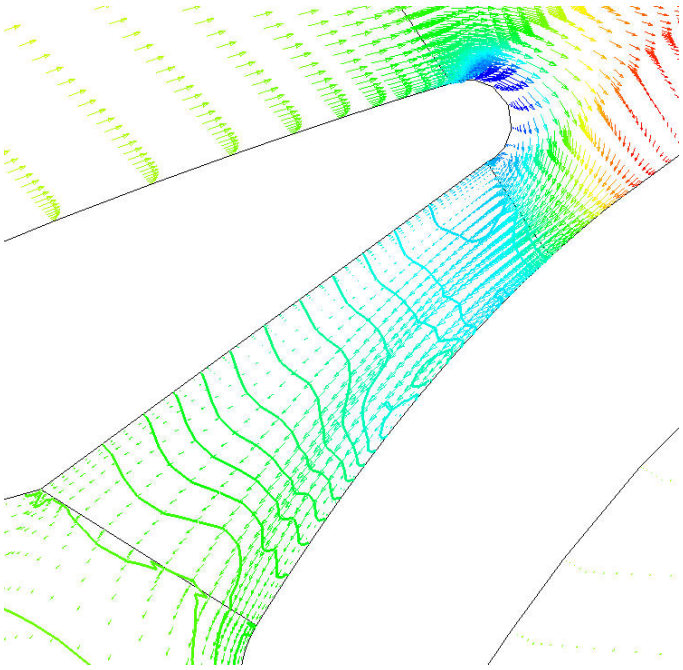

Figure 26. Pressure contours and velocity vectors colored by pressure inside the DSJ slot during maximum in-stroke. The contours show desired pressure recovery within the slot diffuser.

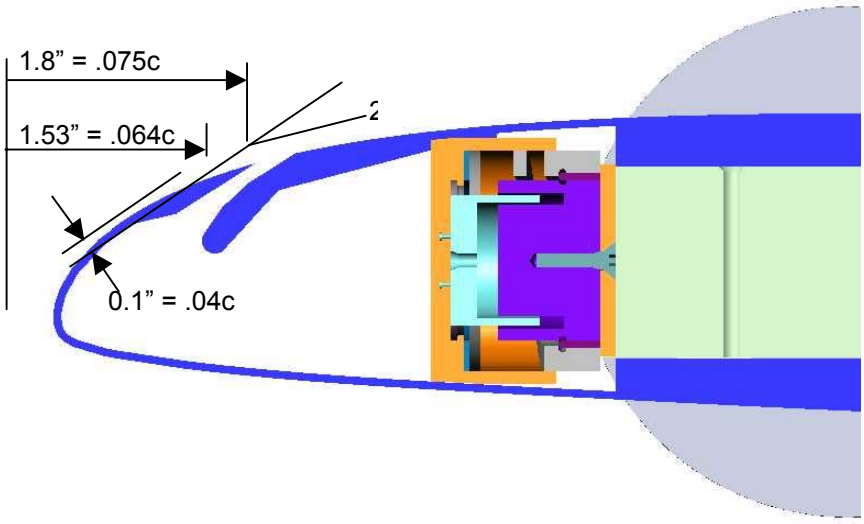

Figure 27. DSJ Slot design used for wind tunnel model.

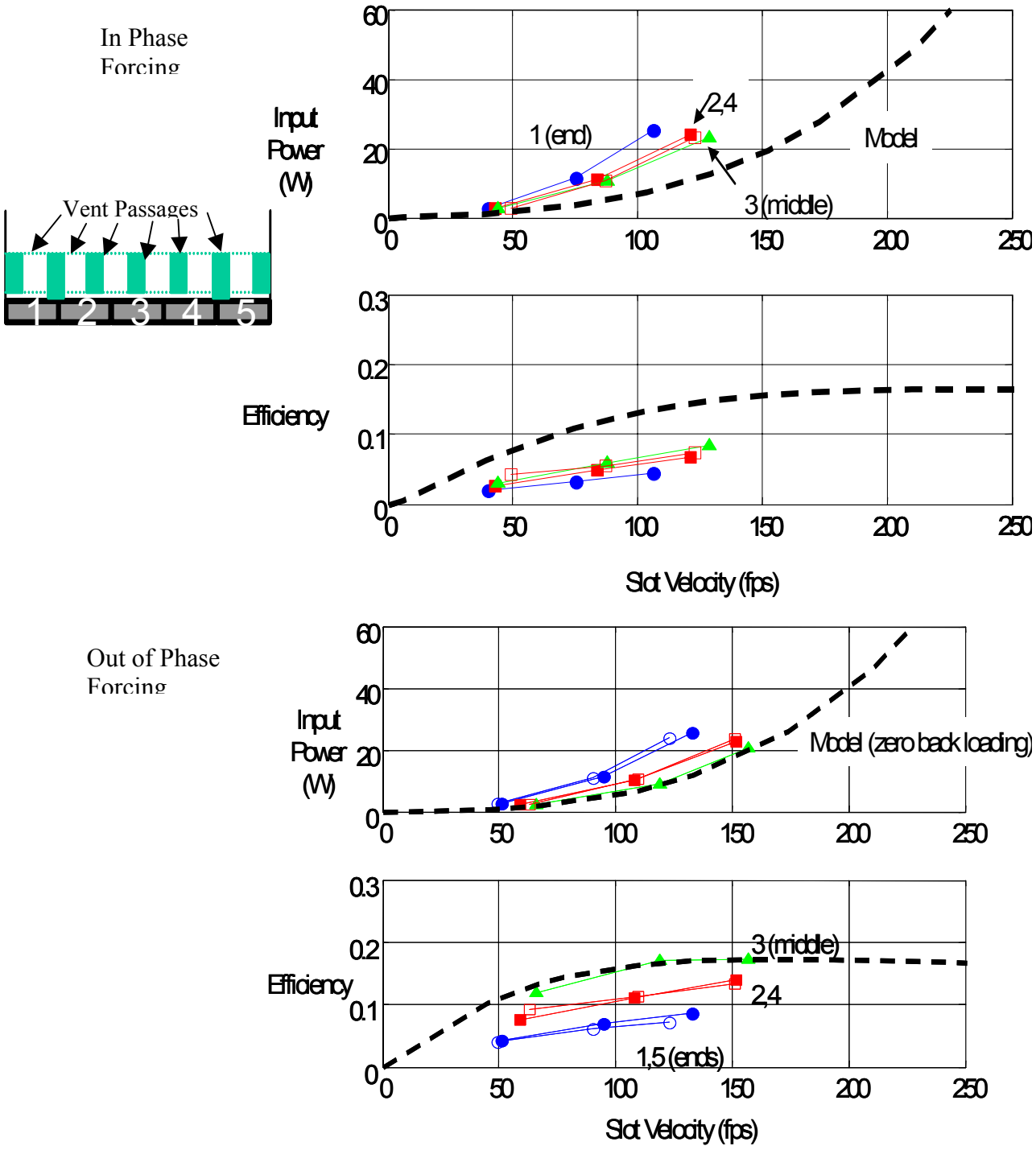

Figure 28. Actuator input power and efficiency measurements, wind-off measurements as installed in blade section. Middle (#3) actuator in out of phase mode matches model best.

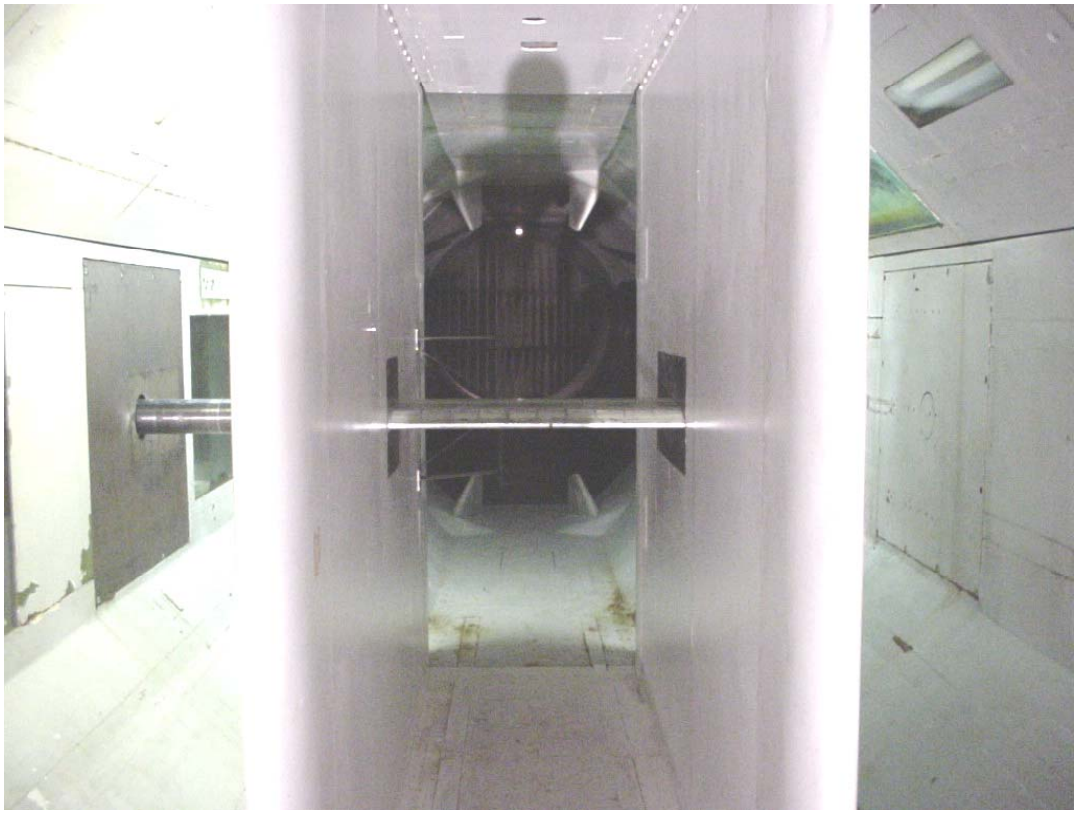

Figure 29. Oscillating blade section installed in 8' x 33" Two Dimensional Channel.

Figure 30. 24” chord SC2110 airfoil model with DSJ actuation.

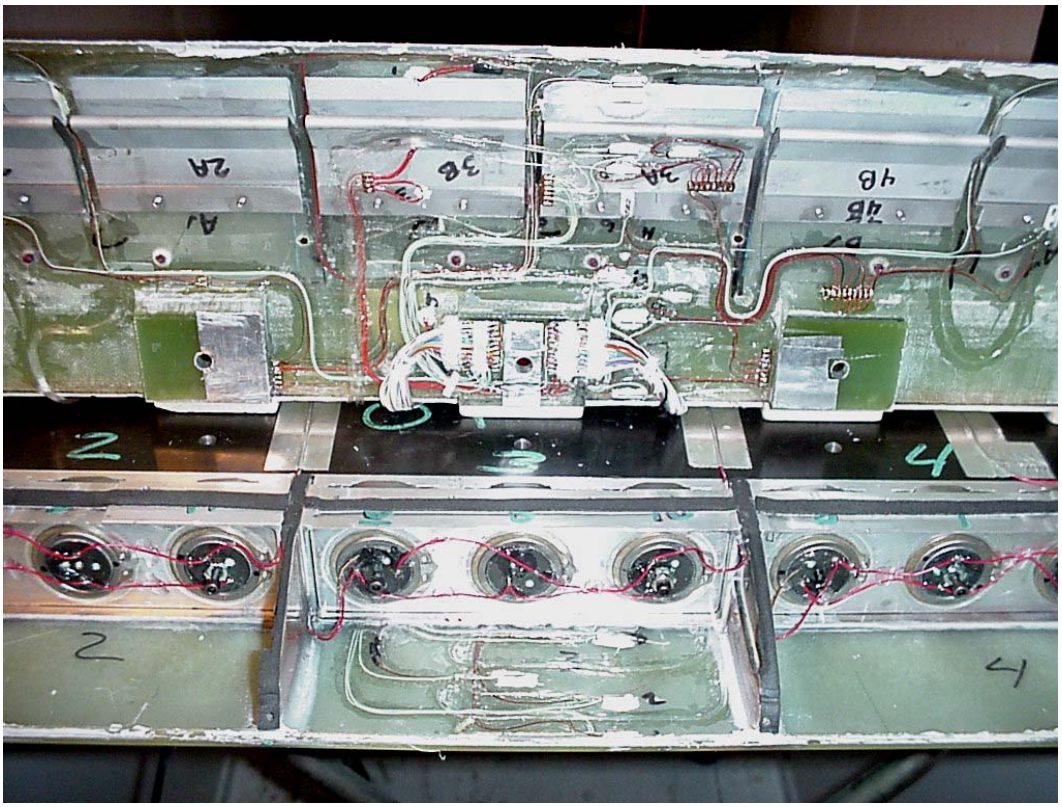

Figure 31. Model with leading edge open, showing actuator modules, DSJ slots, and pressure instrumentation.

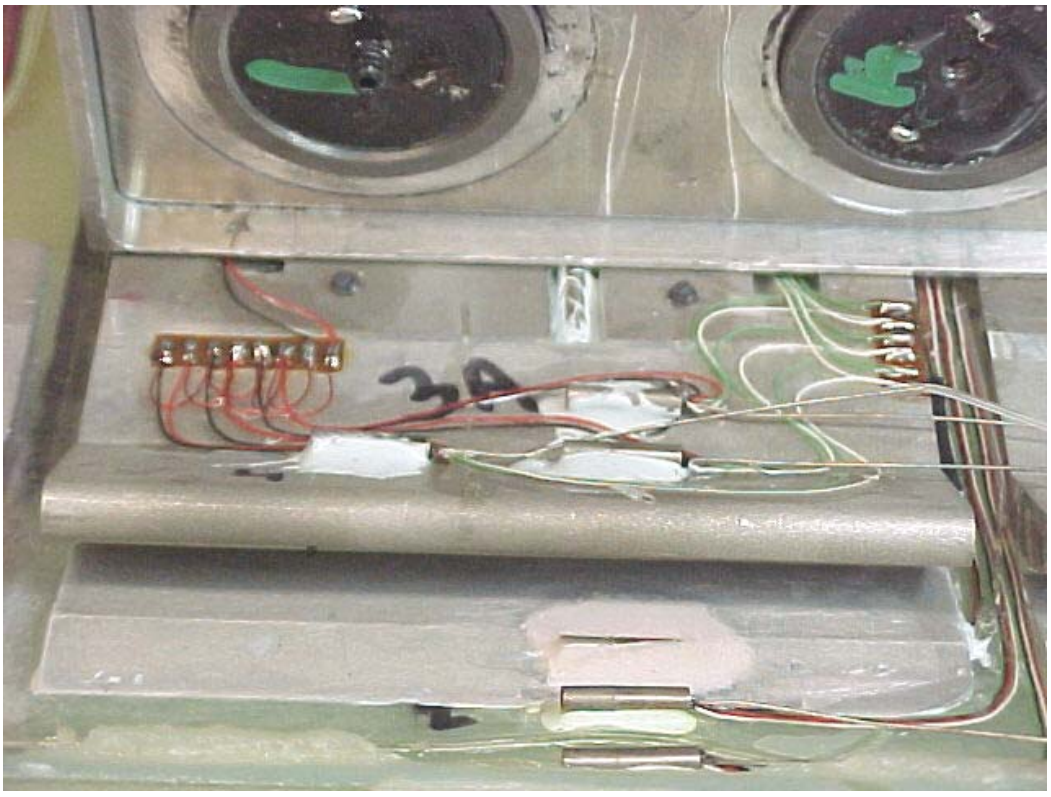

Figure 32. Close-up of pressure instrumentation near DSJ slot.

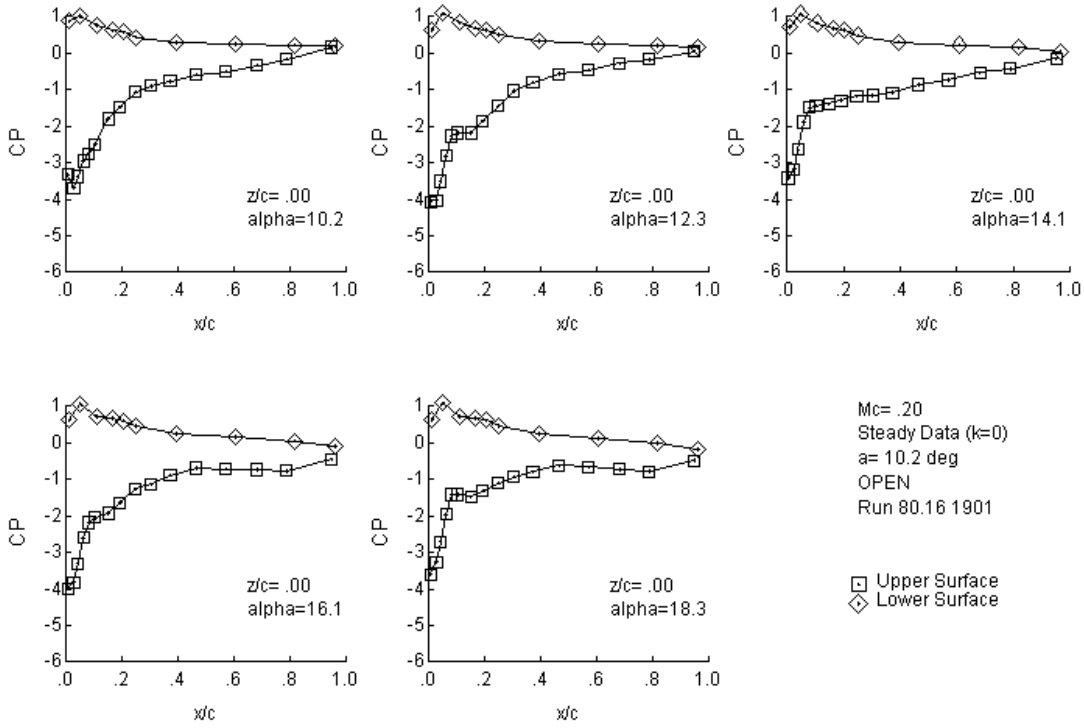

Figure 33. Airfoil pressure distributions in steady flow at M=0.2, DSJ off with slot open.

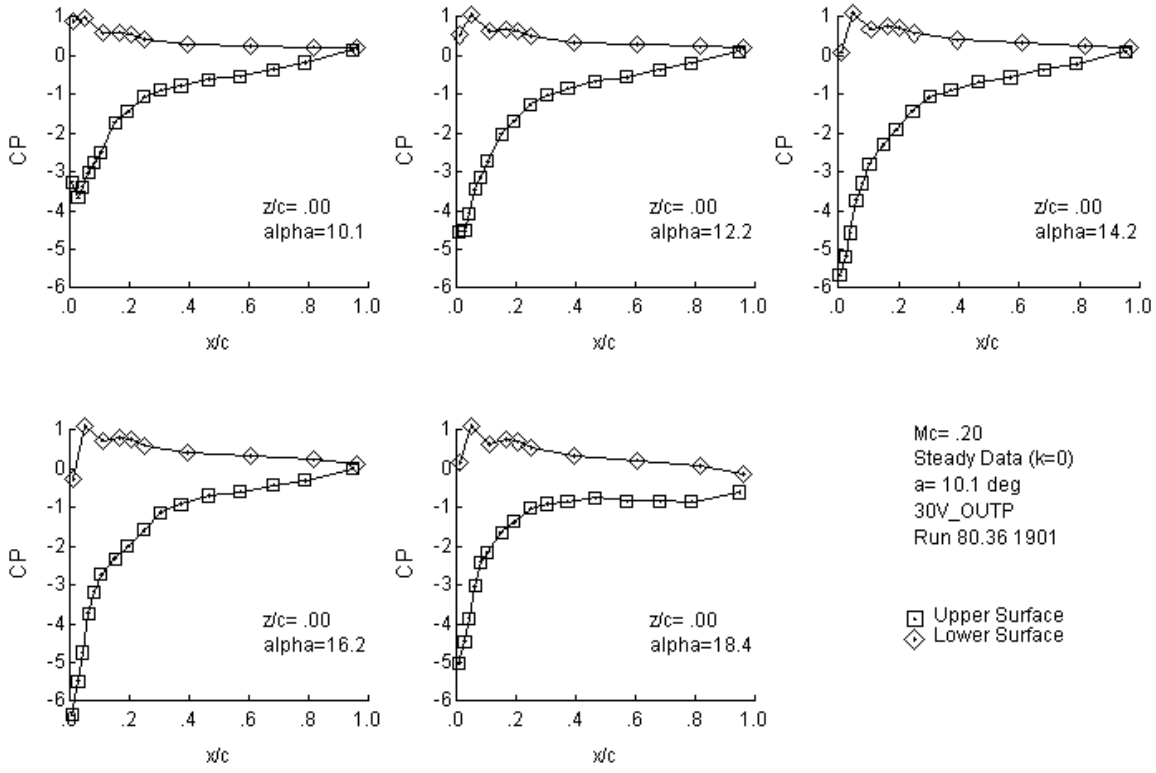

Figure 34. Airfoil pressure distributions in steady flow at M=0.2, DSJ operating at 30V, Cμ~0.15%

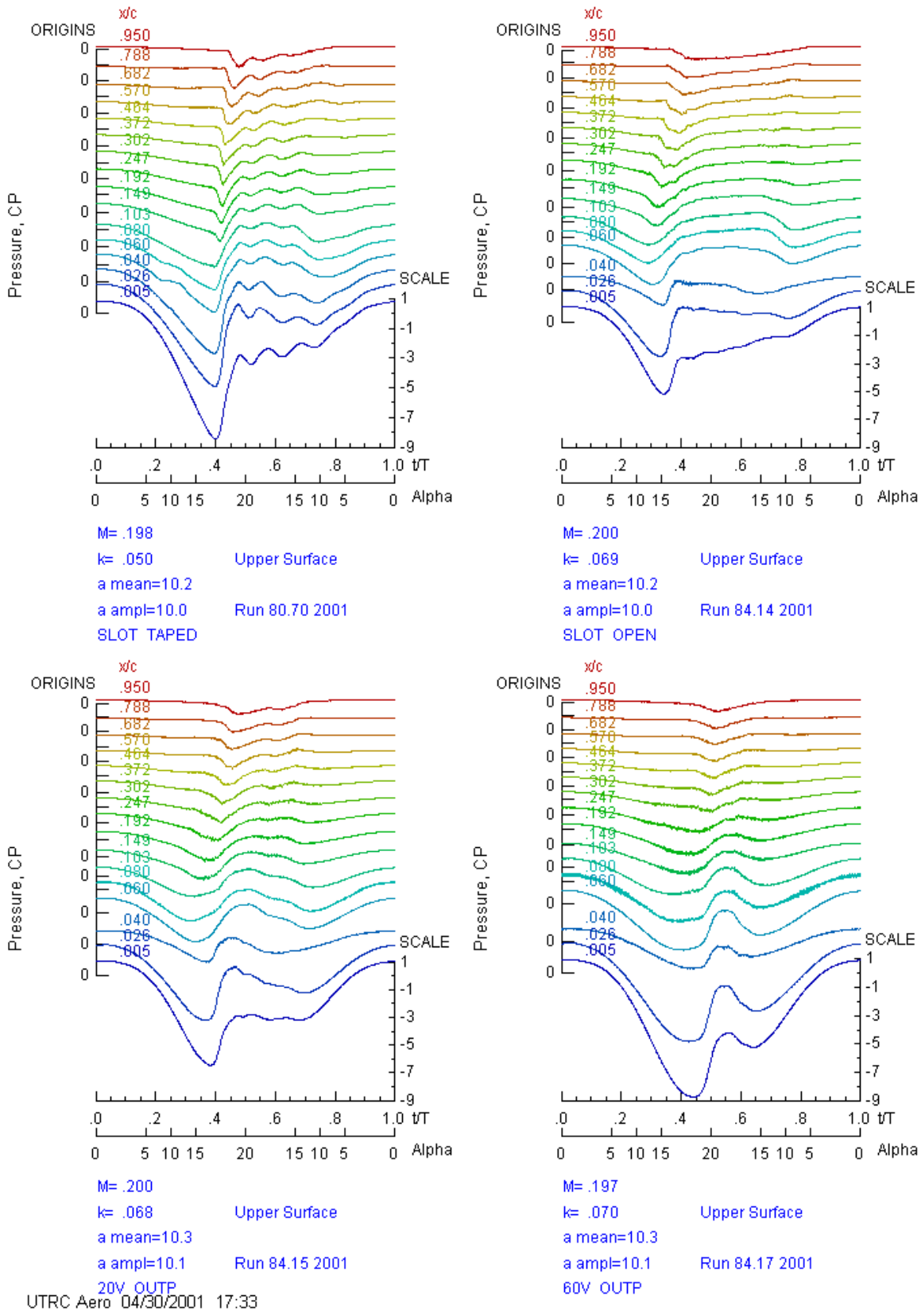

Figure 35. Airfoil unsteady pressure time histories at M=0.2, α=10°-10°cosωt, with DSJ slot taped, slot open, and operating at 20V(Cμ ~.1%) and 60V (Cμ ~.4%).

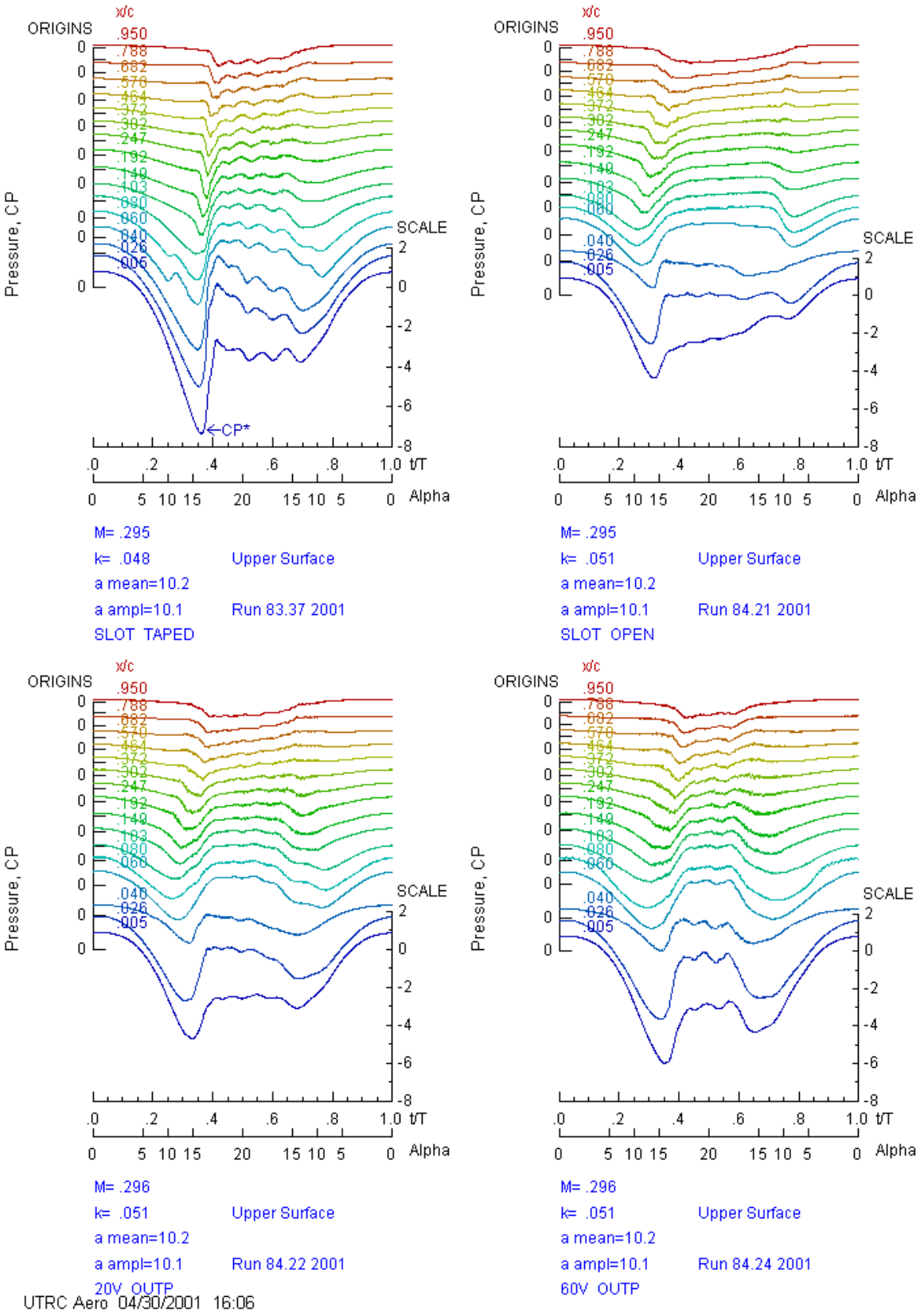

Figure 36. Airfoil unsteady pressure time histories at M=0.3, α=10°-10°cosωt, with DSJ slot taped, slot open, and operating at 20V (Cμ ~.06%) and 60V (Cμ ~.2%).

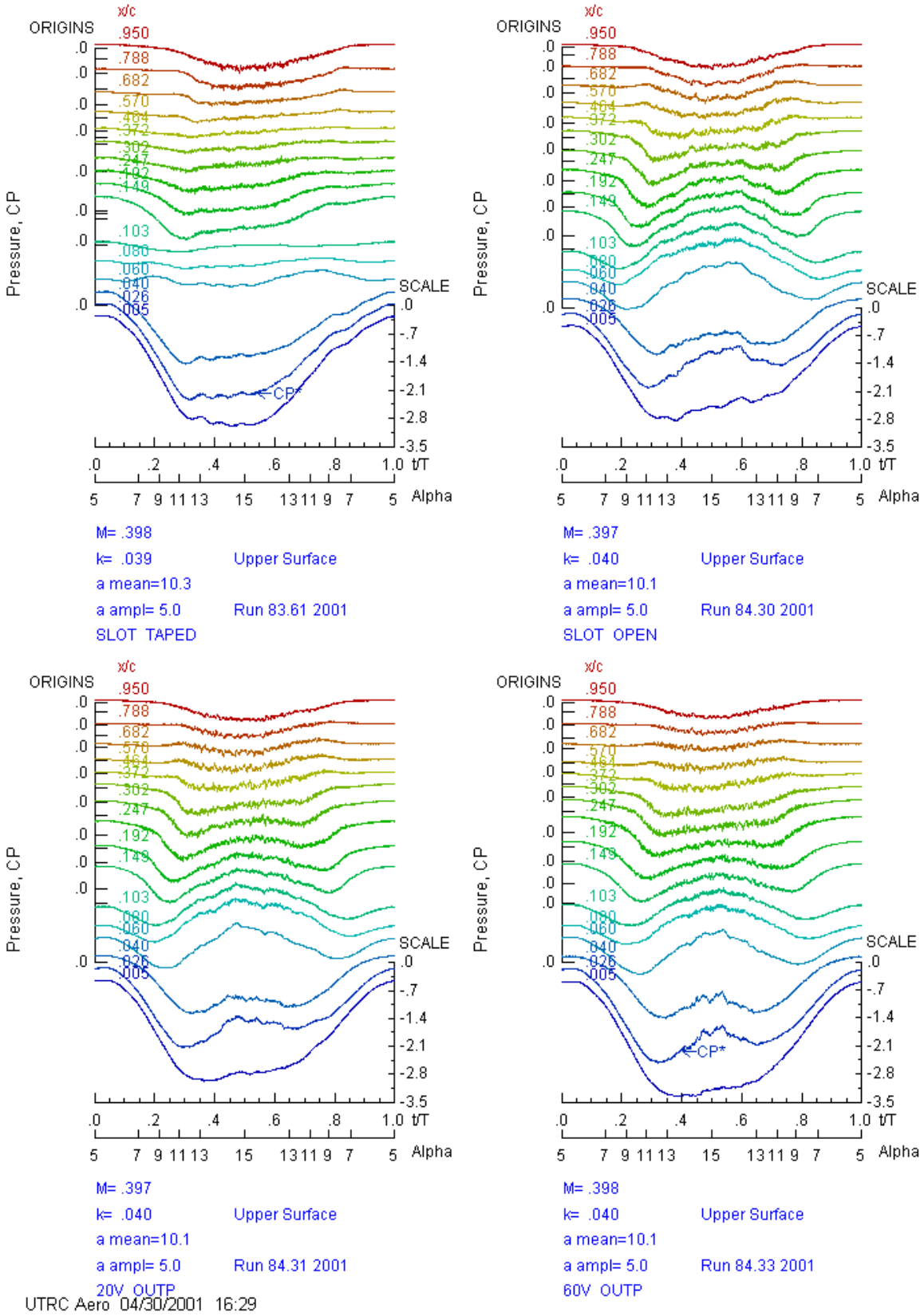

Figure 37. Airfoil unsteady pressure time histories at M=0.4, α=10°-5°cosωt, with DSJ slot taped, slot open, and operating at 20V (Cμ ~.04%) and 60V (Cμ ~.1%).

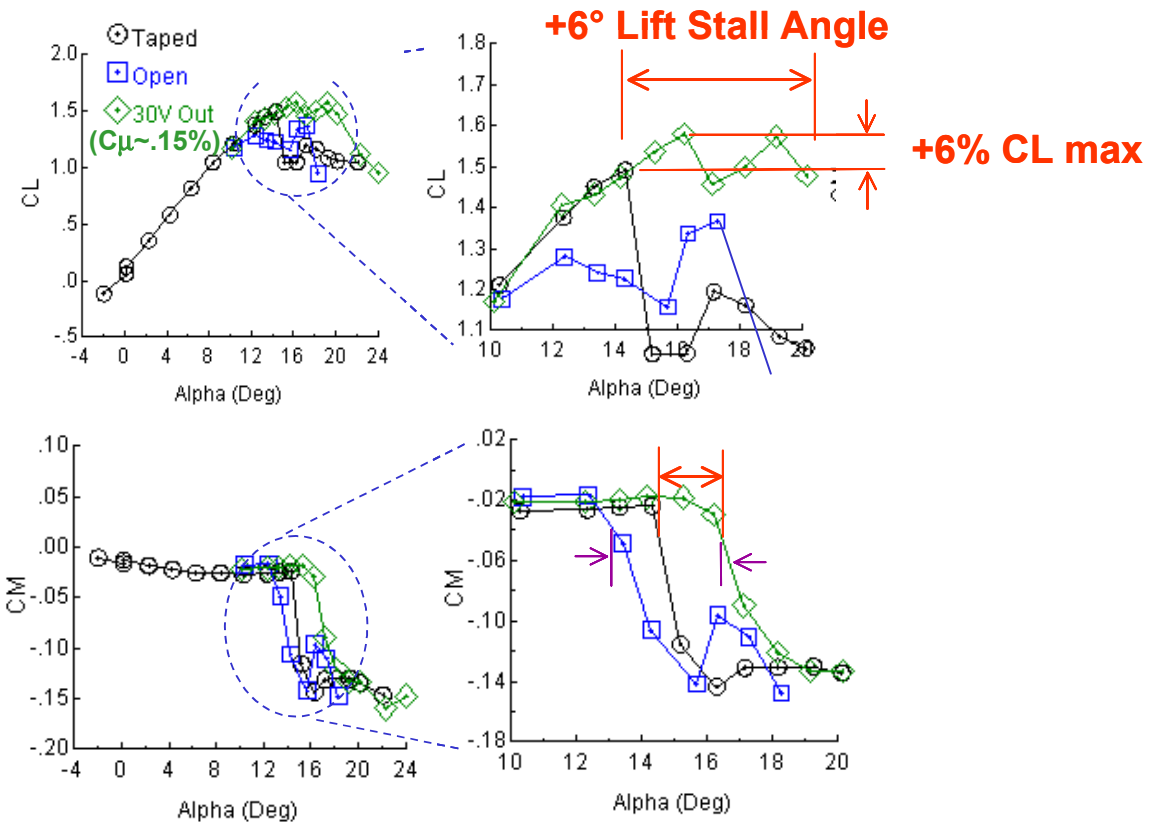

Figure 38. Steady lift and pitching moment results at M=0.2 for baseline (DSJ slot taped), slot open, and slot operating at Cu~0.15%

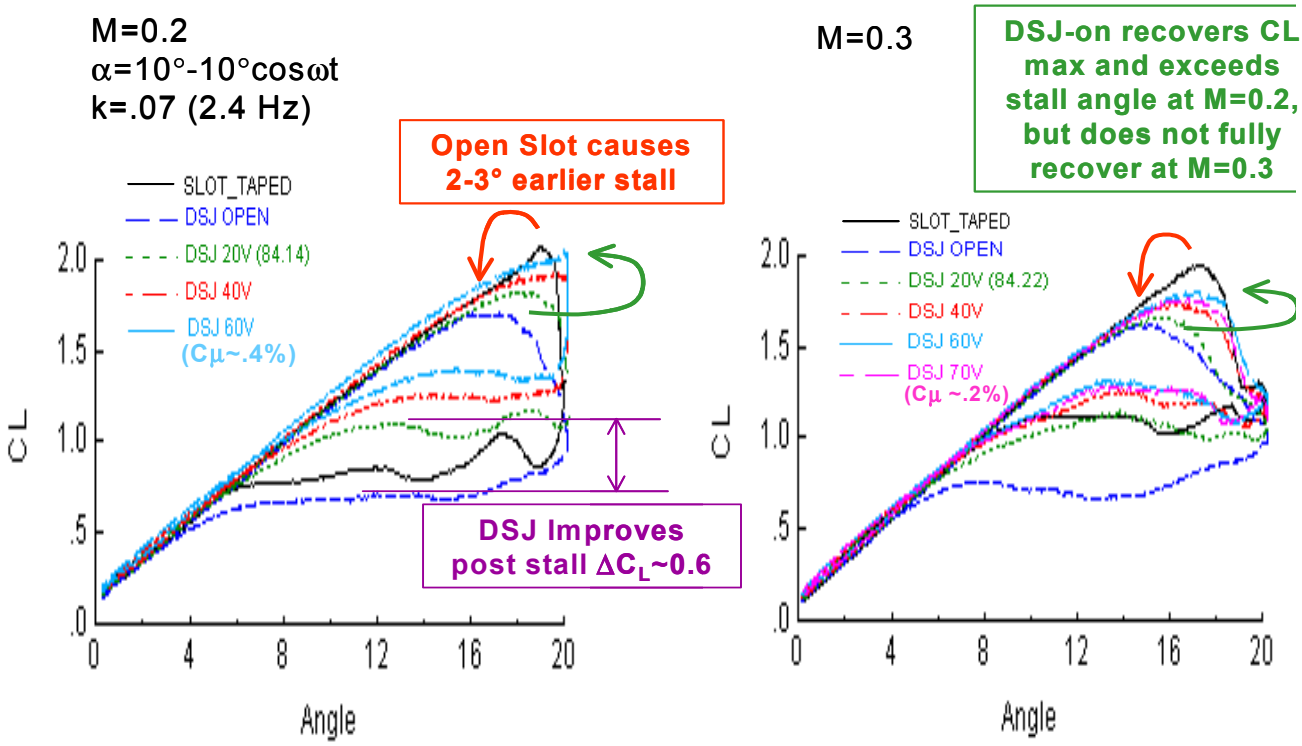

Figure 39 Unsteady lift results at M=0.2 and 0.3 for baseline (DSJ slot taped), slot open, and slot operating at several Cu.

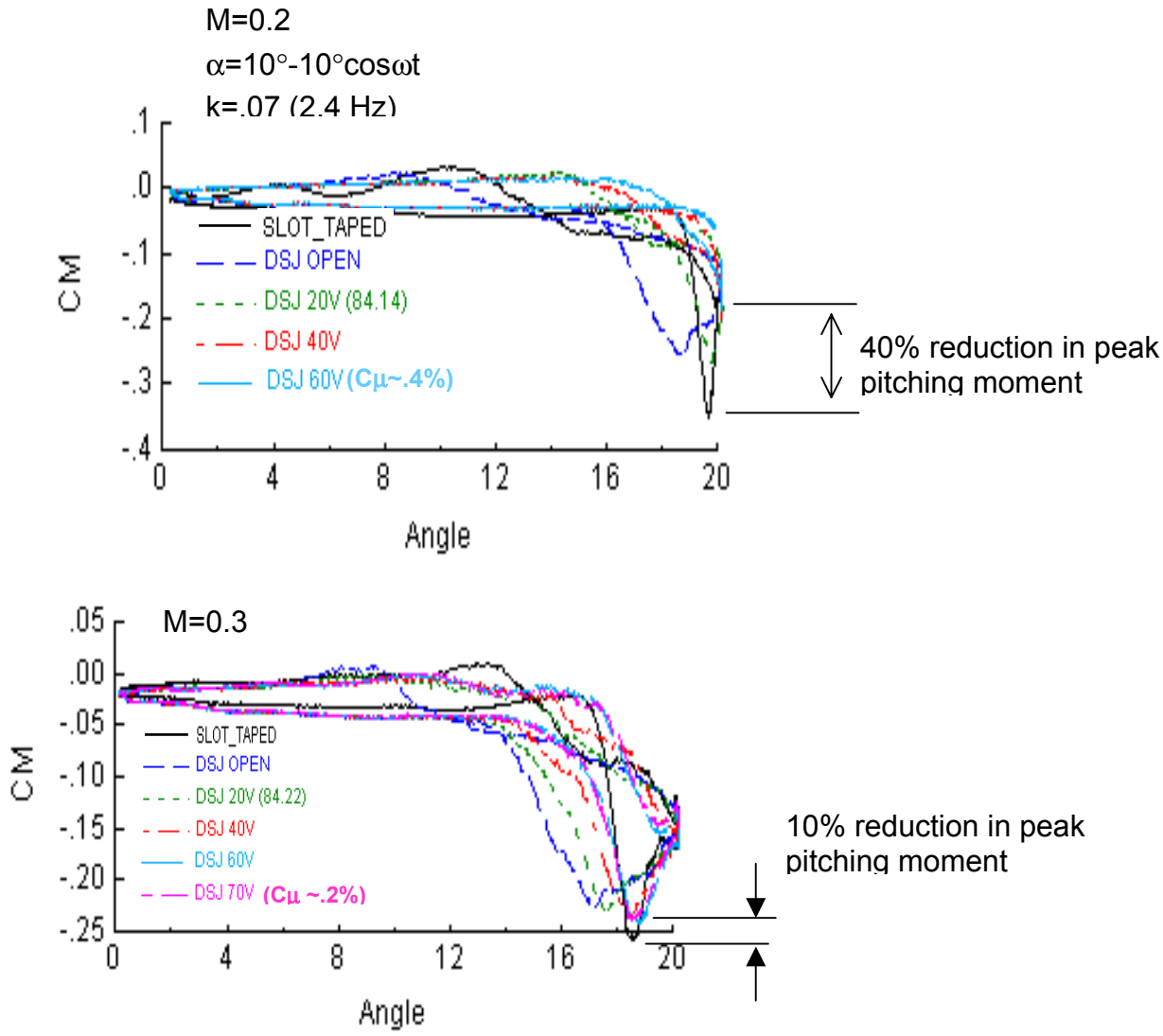

Figure 40 Unsteady pitching moment results at M=0.2 and 0.3 for baseline (DSJ slot taped), slot open, and slot operating at several Cμ.

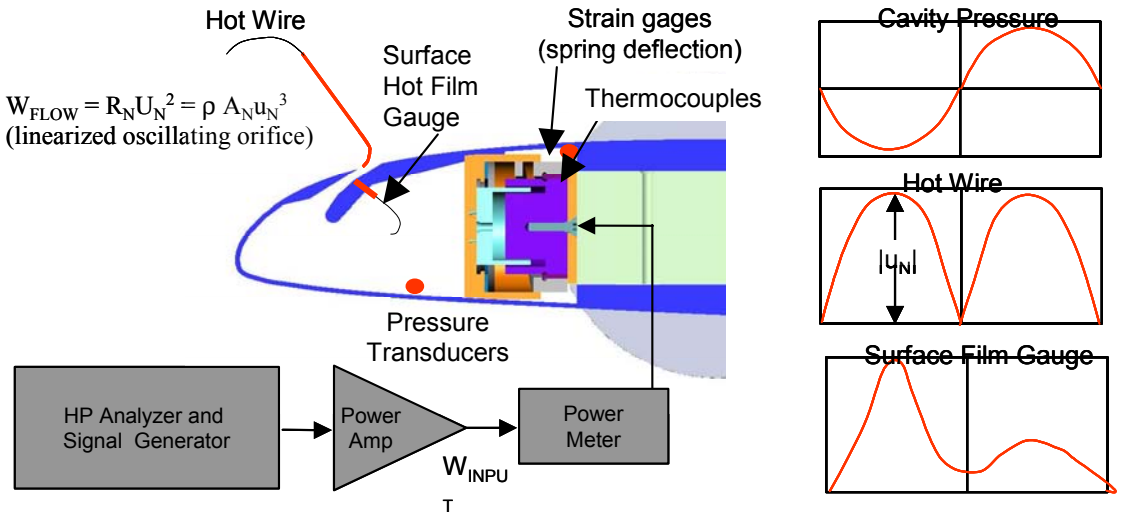

Figure 41 Actuator performance and diagnostic measurement approach

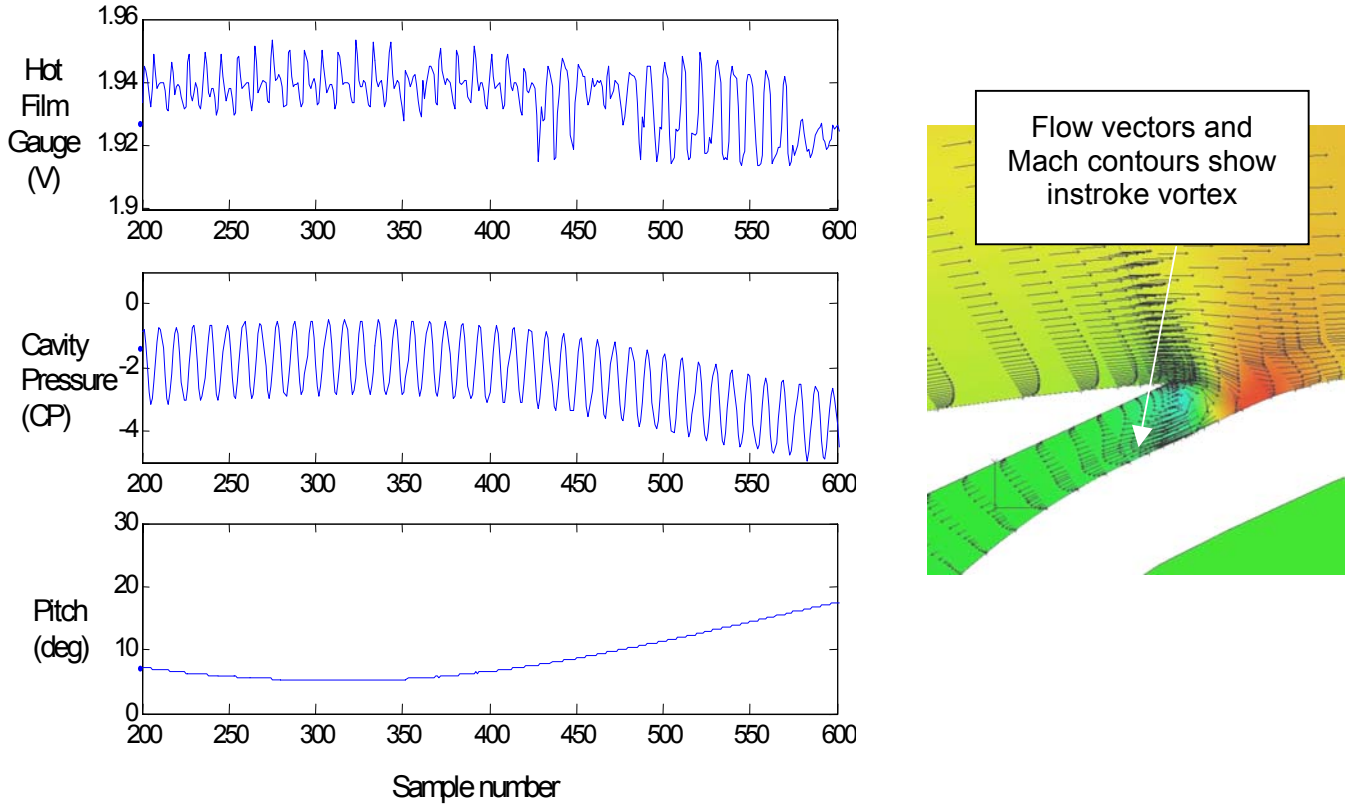

Figure 42. Sample slot diagnostic time histories: in-slot hot film gage voltage, leading edge cavity pressure, and blade pitch angle, plus CFD visualization of instroke vortex.

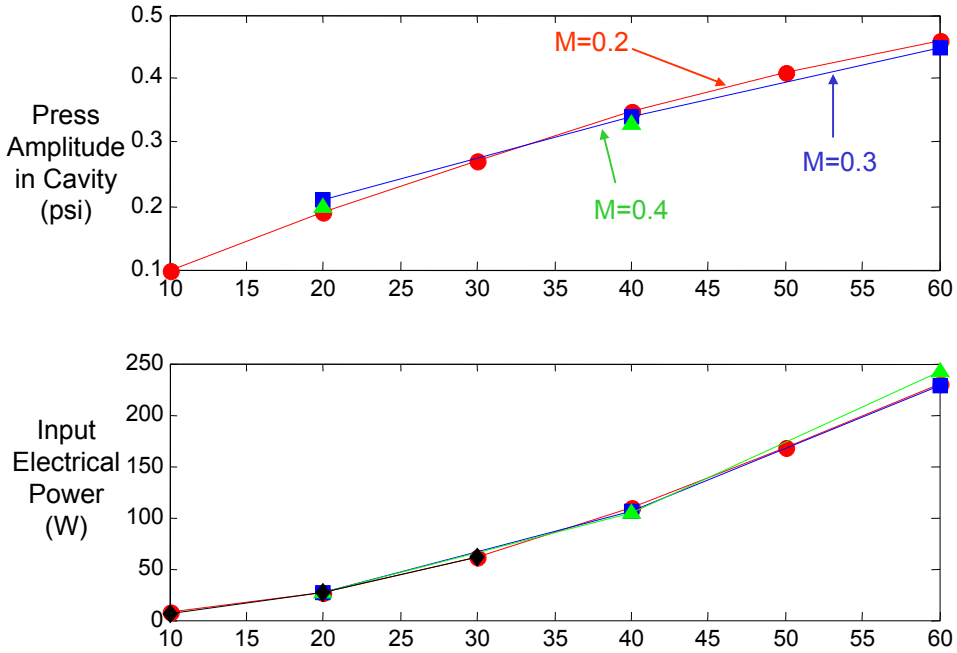

Figure 43. Cavity pressure amplitude and input power required as function of input voltage at Mach numbers of 0.2, 0.3, and 0.4.

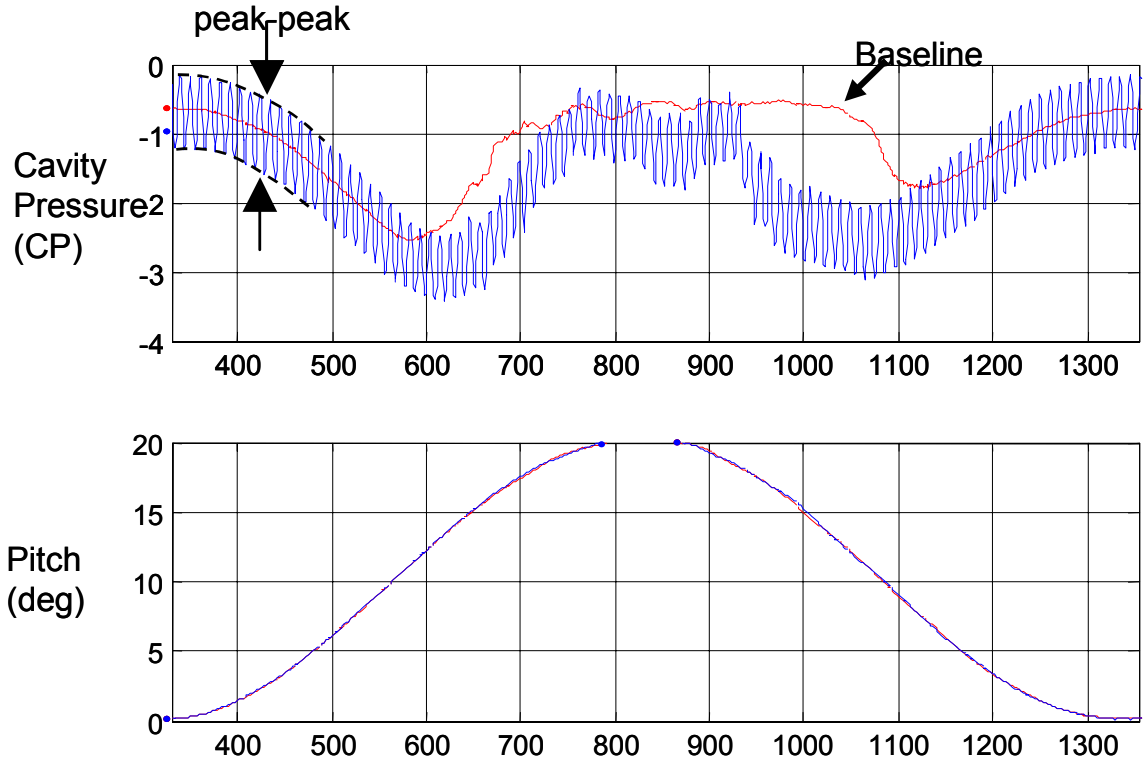

Figure 44. Comparison of cavity pressure amplitude for baseline (DSJ-on) and actuated conditions shows similar amplitudes maintained throughout airfoil pitching motion

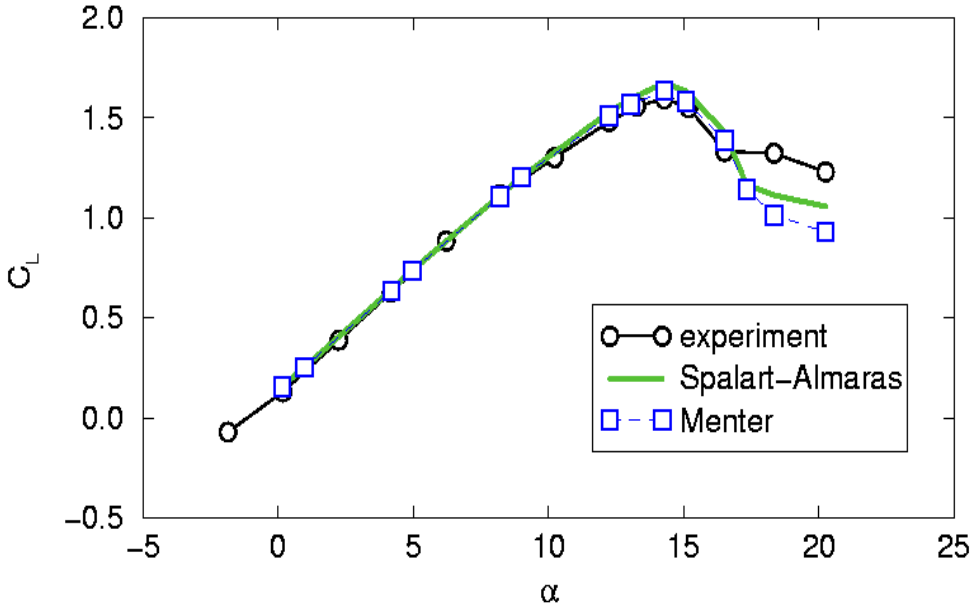

Figure 45. Steady-state stall predicted well by CFD

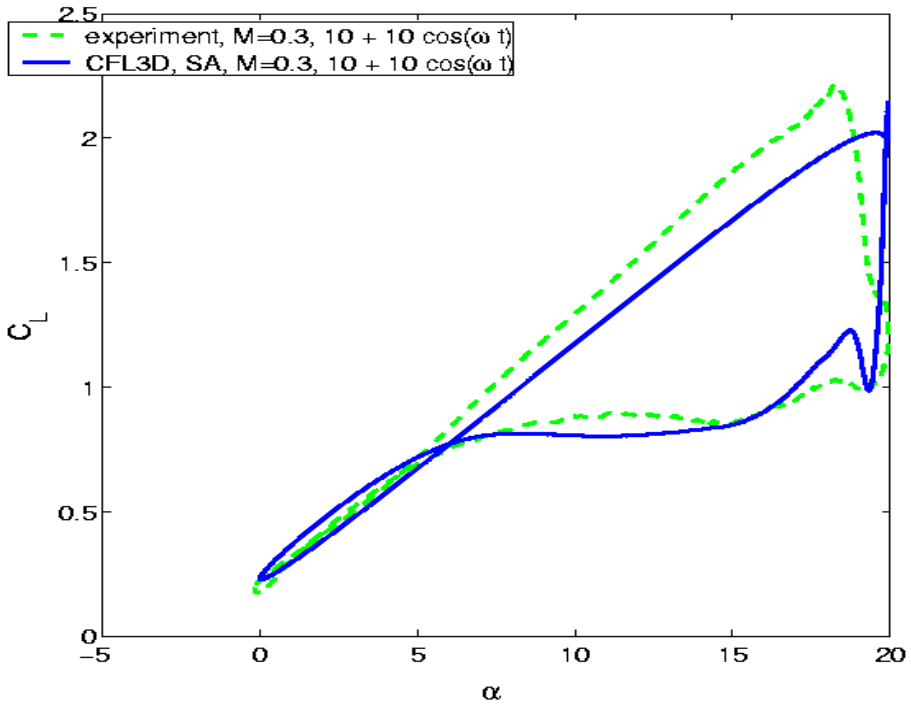

Figure 46. Unsteady CFD calculation predicts dynamic stall sufficiently well for $\alpha=10+10\sin(\omega t)$, freestream Mach number=0.3.

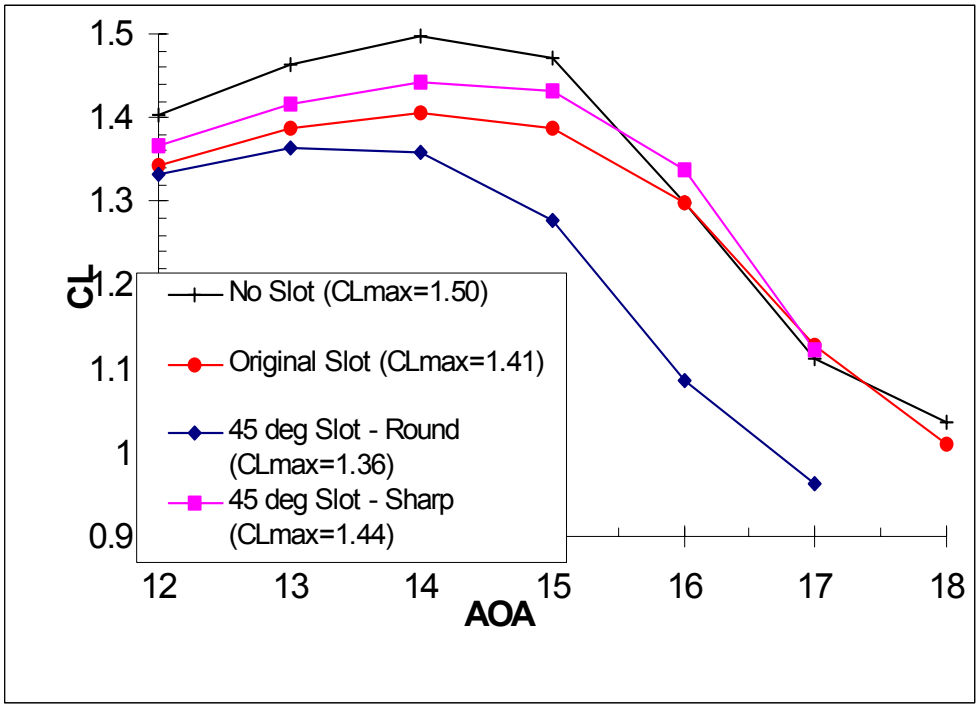

Figure 47. Slot design can recover about 50% of the lift loss due to the open slot with blowing off.

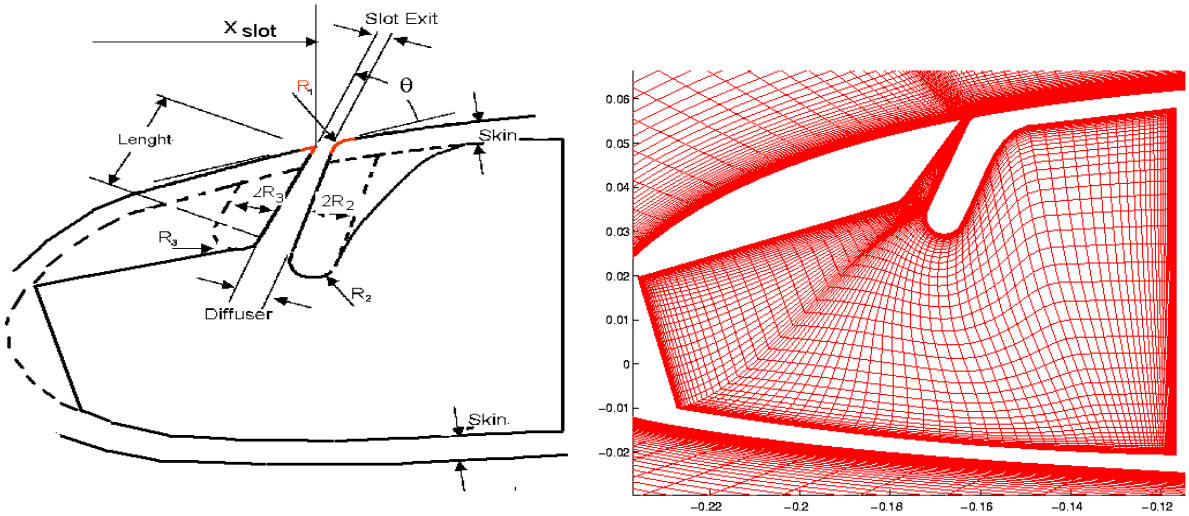

Figure 48. Slot design parameters and automatic block grids

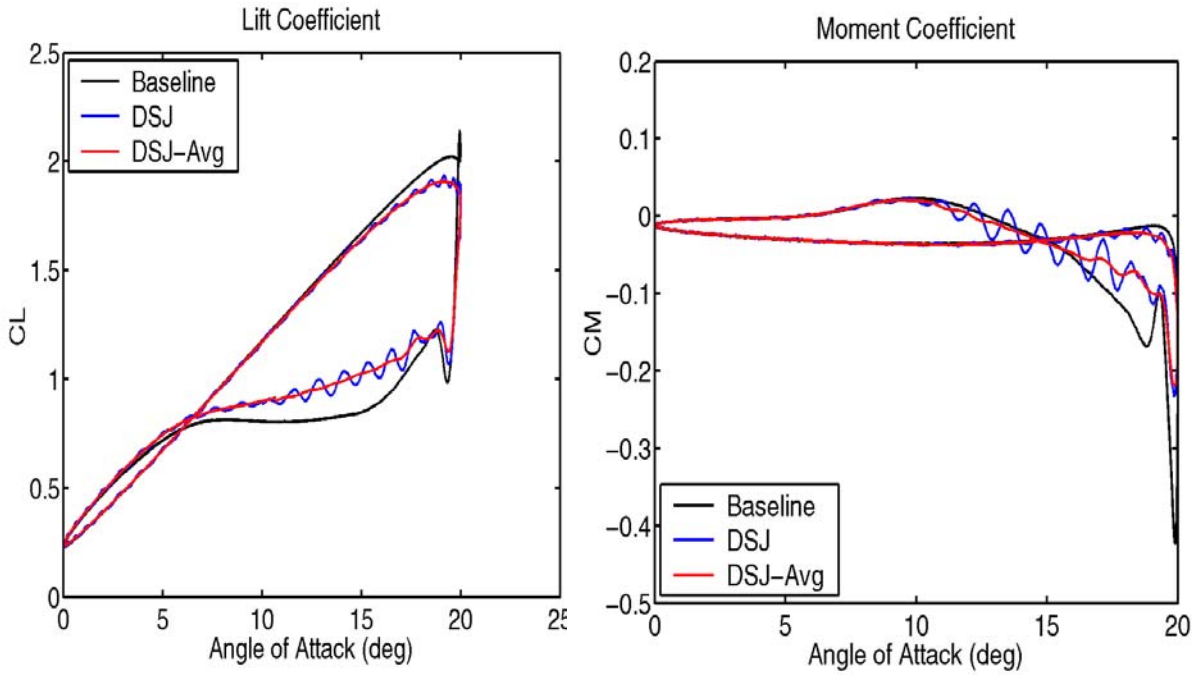

Figure 49. For sinusoidal dynamic stall, low levels of blowing do not improve maximum lift. Post-stall lift is improved as is the minimum pitching moment.

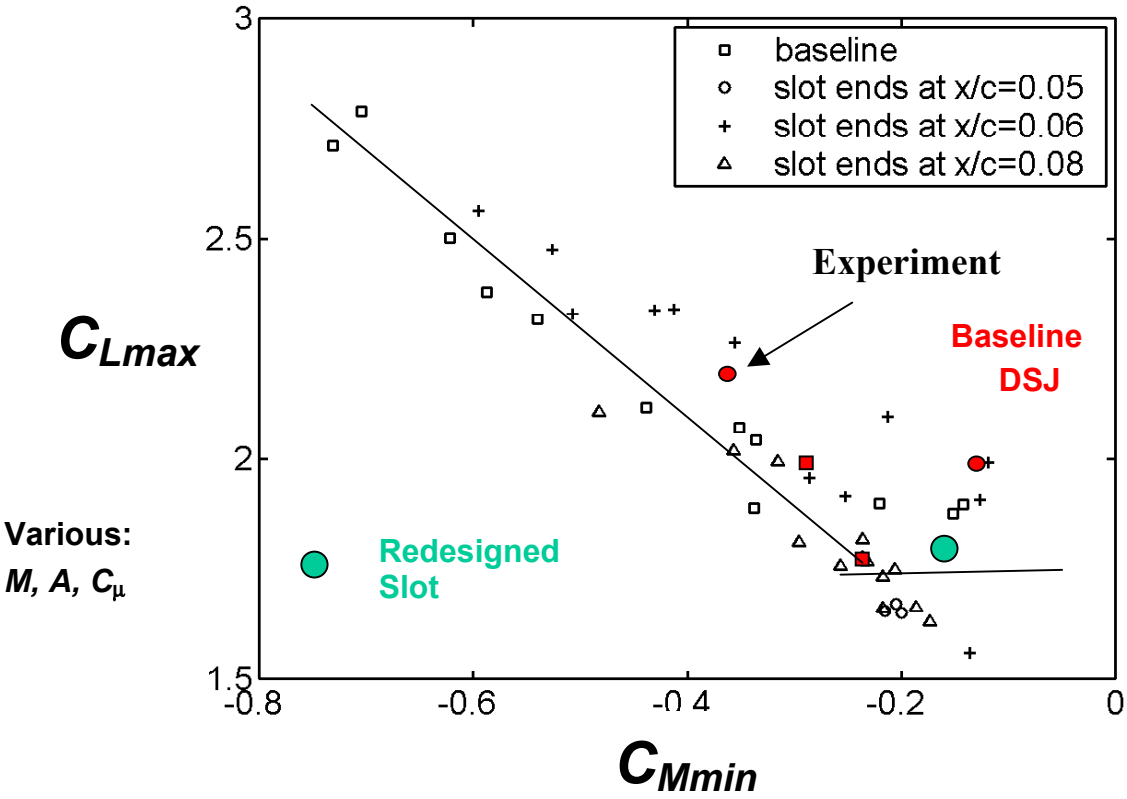

Figure 50. Maximum lift coefficient versus minimum pitching moment is shown for a range of unsteady stall cases. General trends agree with experiment. Higher levels of blowing shift airfoil to a new curve.

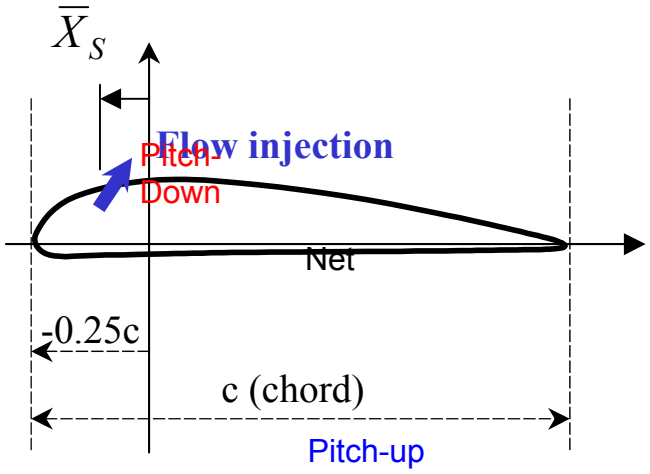

Figure 51. Schematic view of the coordinate system and flow injection slot

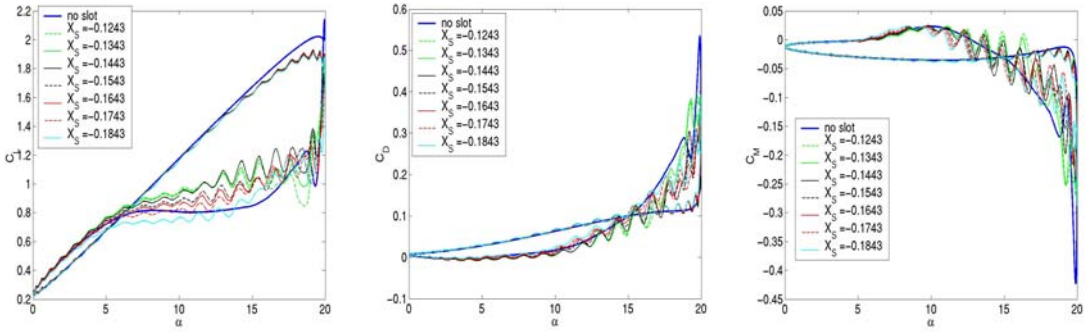

Figure 52. Unsteady lift coefficient C_L, drag coefficient C_D, and moment coefficient C_M versus angle of attack with $\alpha = 10 + 10\sin(\omega t)$ for SC2110 airfoil with variations in slot position. $C_{\mu\,Avg} = 0.13\%$.

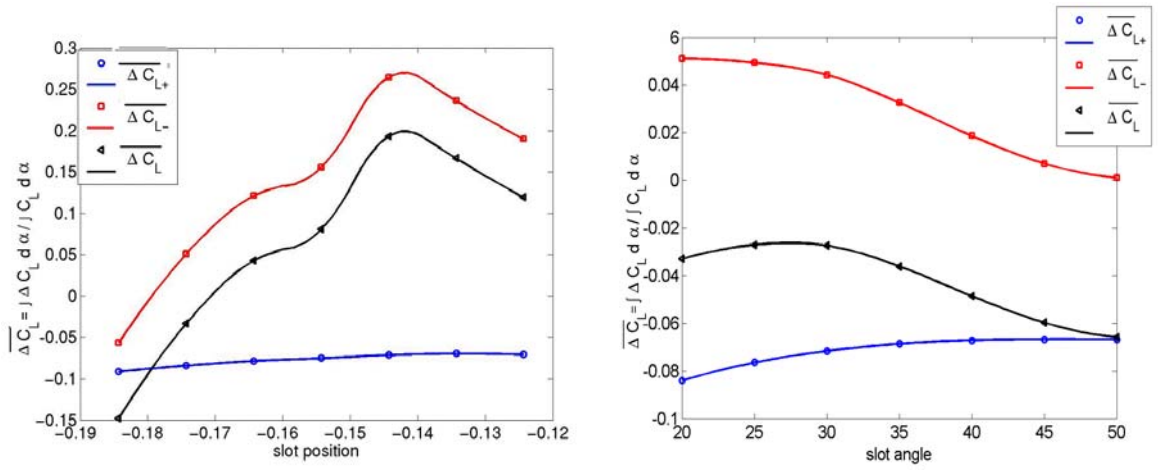

Figure 53. Variation of $\overline{\Delta C_L}$ with respect to upper surface slot position and slot angle. M_∞= 0.3, slot angle = 20 deg $C_{\mu\,Avg}$ = 0.13%.

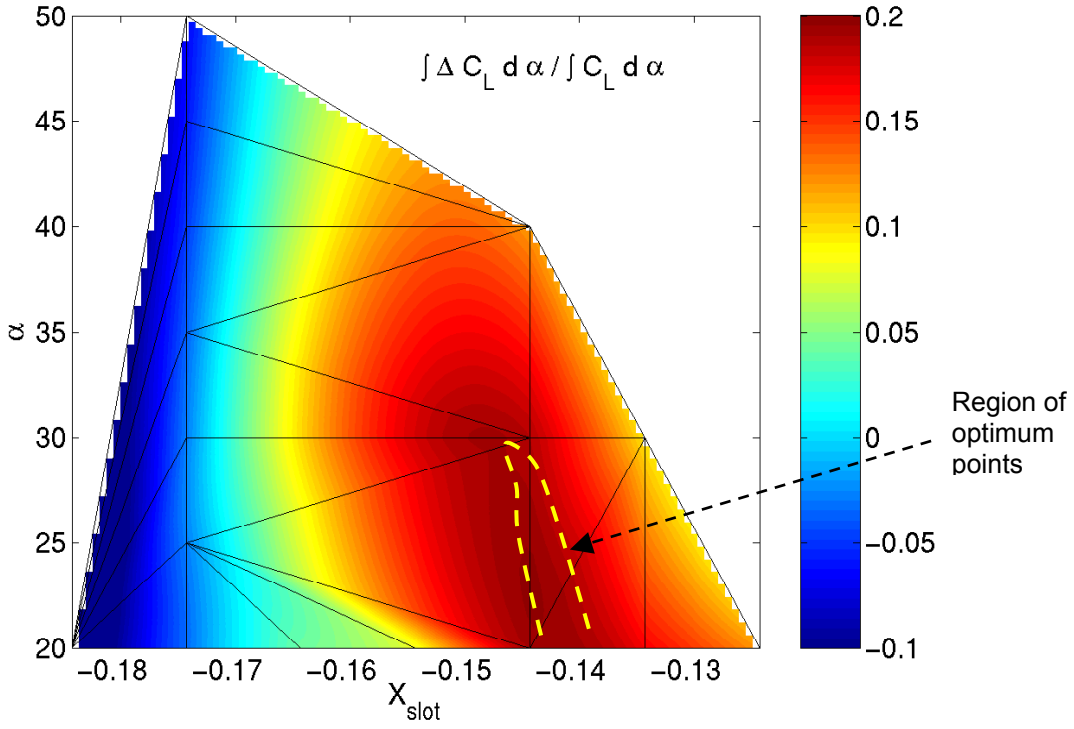

Figure 54. Contours of $\overline{\Delta C_L}$ with respect to slot angle and slot position, for a slot on upper wall of the SC2110 airfoil. Slot exit width = 0.043c. (Conditions are the same as Fig. 52.) $C_{\mu\ Avg}$ = 0.13%.

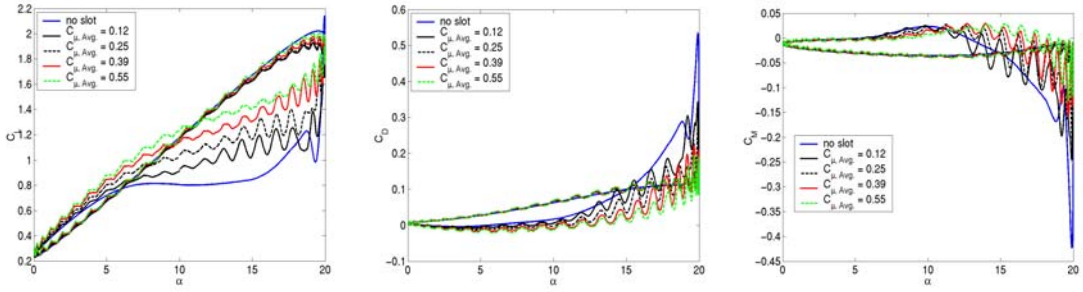

Figure 55. Unsteady lift coefficient C_L, drag coefficient C_D, and the moment coefficient C_M ver angle of attack with $\alpha = 10 + 10\sin(\omega t)$ for a SC2110 airfoil with variations in momentum coef ($C_{\mu\ Avg}$, given in %). M_∞ = 0.3, slot angle = 20 deg.

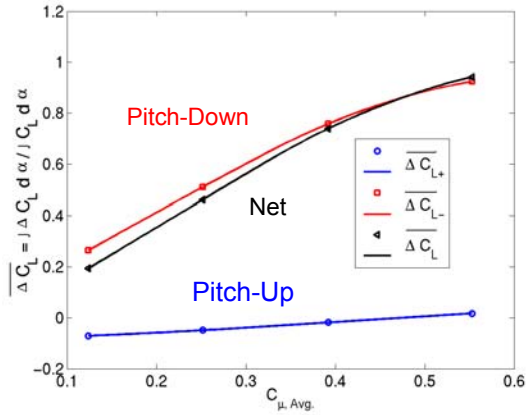

Figure 56. Variation of $\overline{\Delta C_L}$ with momentum coefficient (in %) for the SC2110 airfoil and X_S=-0.174 (same conditions as Figure 55)

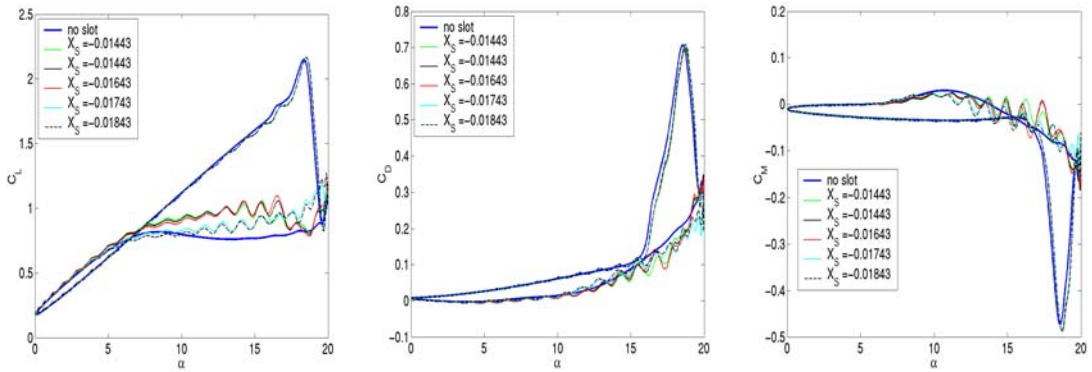

Figure 57. Unsteady lift coefficient C_L, drag coefficient C_D, and the moment coefficient C_M versus angle of attack with $\alpha = 10 + 10\sin(\omega t)$ for a SSCA09 airfoil with variations in slot position. M_∞=0.3, slot angle=20 deg. $C_{\mu\,Avg}$ = 0.13%.

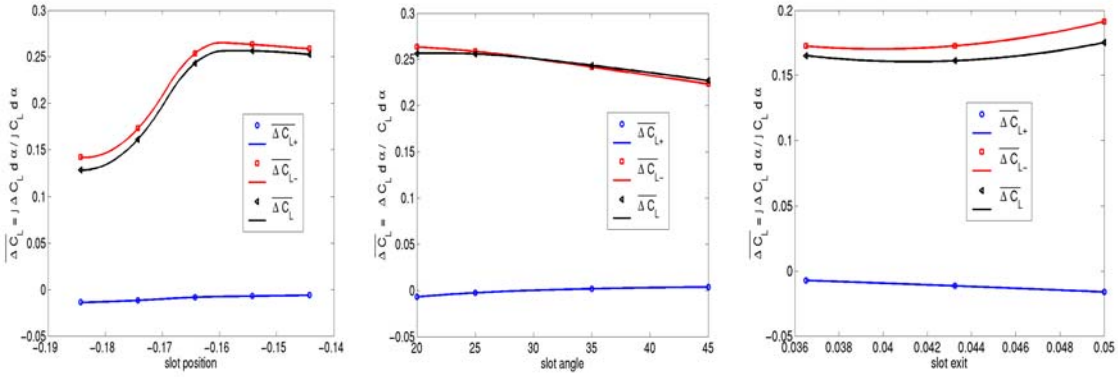

Figure 58. Variation of $\overline{\Delta C_L}$ with slot position, slot angle, and slot exit width for the SSCA09 airfoil and slot angle=20 deg (same conditions as Figure 57). $C_{\mu\,Avg}$ = 0.13%.

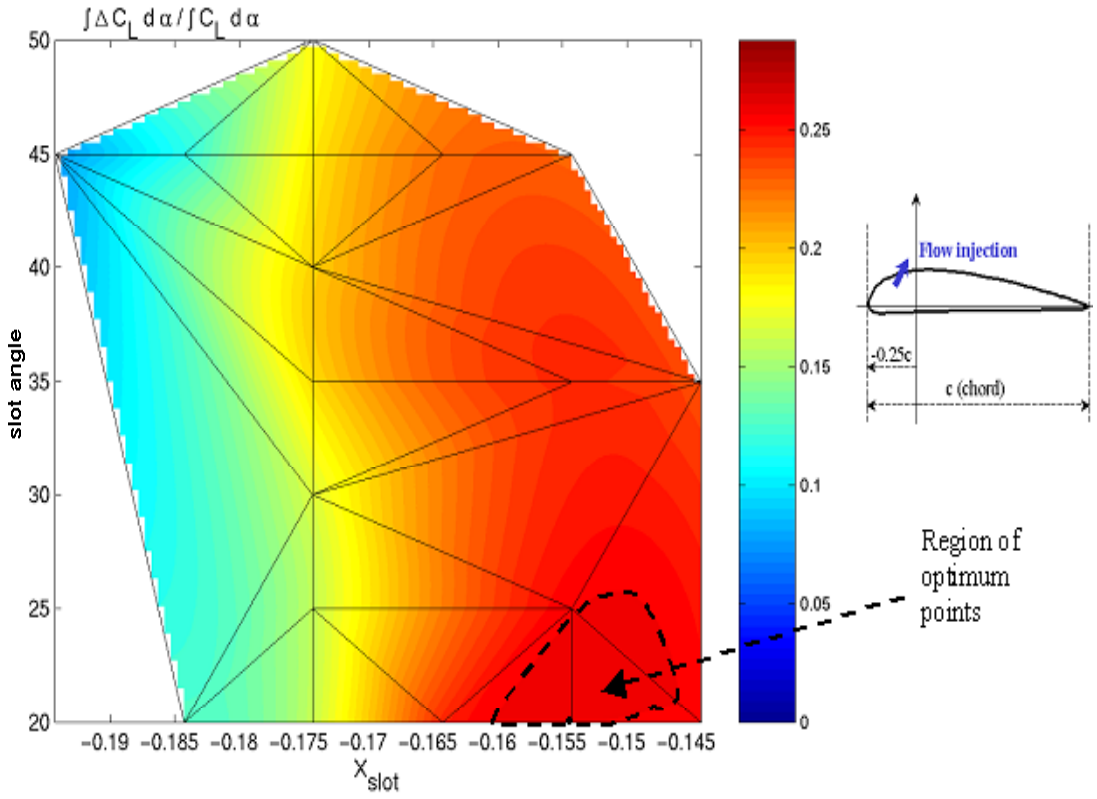

Figure 59. Contours of $\overline{\Delta C_L}$ with respect to slot angle and slot position. Slot on upper surface of the SSCA09 airfoil, height 0.043c. (Conditions as Fig. 57.) $C_{\mu\ Avg}$ = 0.13%

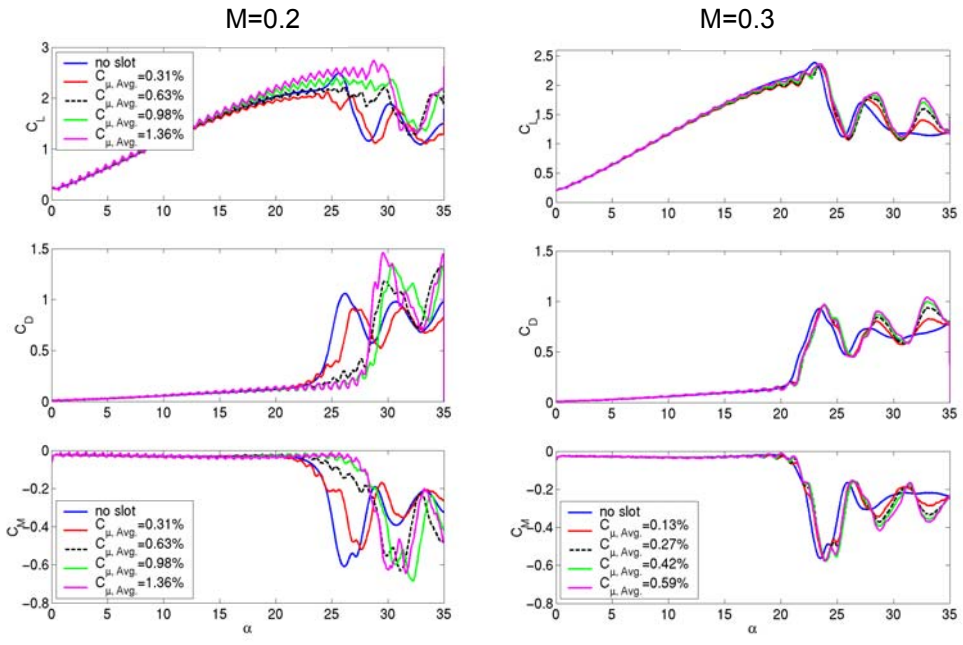

Figure 60. C_L, C_M, and C_D time histories for constant pitch rate ramp motions at M=0.2 and 0.3 and A=0.01. Single upper surface slot and SC2110 airfoil.

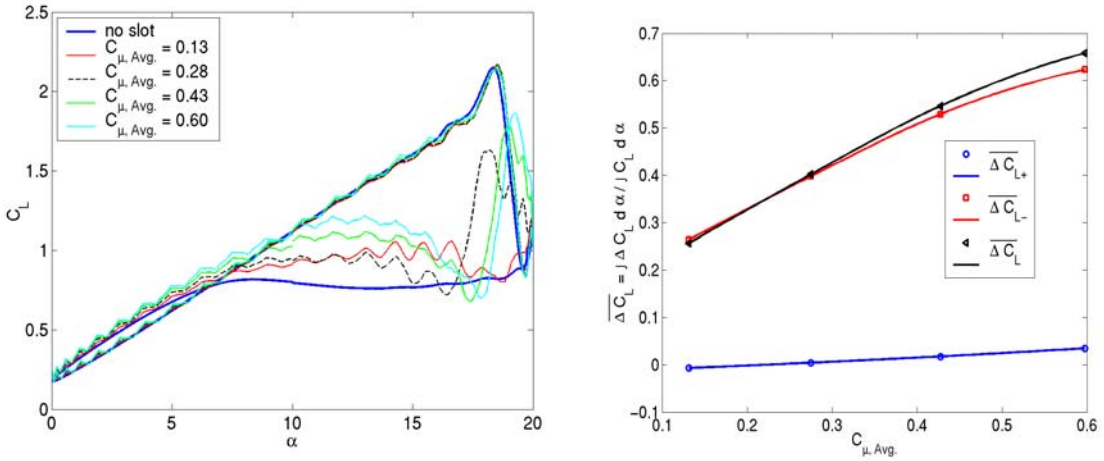

Figure 61. Unsteady lift coefficient and variation of $\overline{\Delta C_L}$ for SSCA09 airfoil for variations in $C_{\mu, Avg.}$ M_∞=0.3, X_S=-0.154.

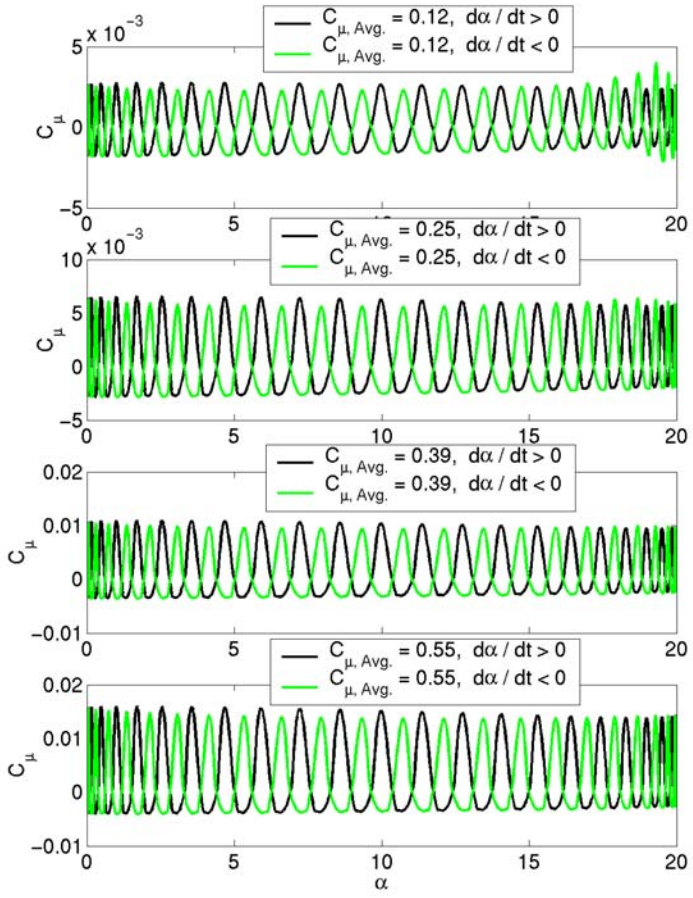

Figure 62. Instantaneous momentum coefficient versus angle of attack for different levels of unsteady blowing

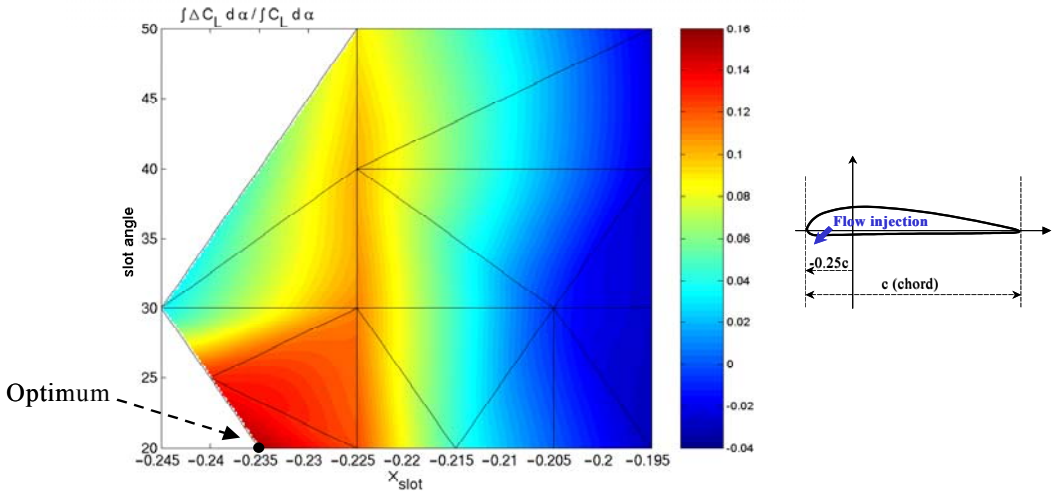

Figure 63. Contours of $\overline{\Delta C_L}$ with respect to slot angle and slot position (X_S), for a slot on the lower surface of the SSCA09 airfoil. Slot exit = 0.043c. $C_{\mu\ Avg}$ = 0.13%.

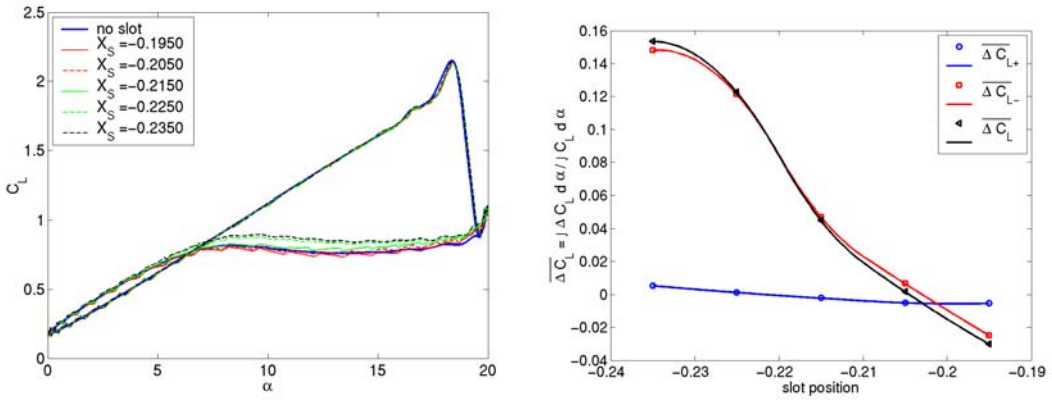

Figure 64. Unsteady C_L and variation of $\overline{\Delta C_L}$ with lower surface slot position. M=0.3, $\alpha = 10 + 10\sin(\omega t)$, SSCA09, slot angle = 20°, and $C_{\mu\ Avg}$ = 0.13%.

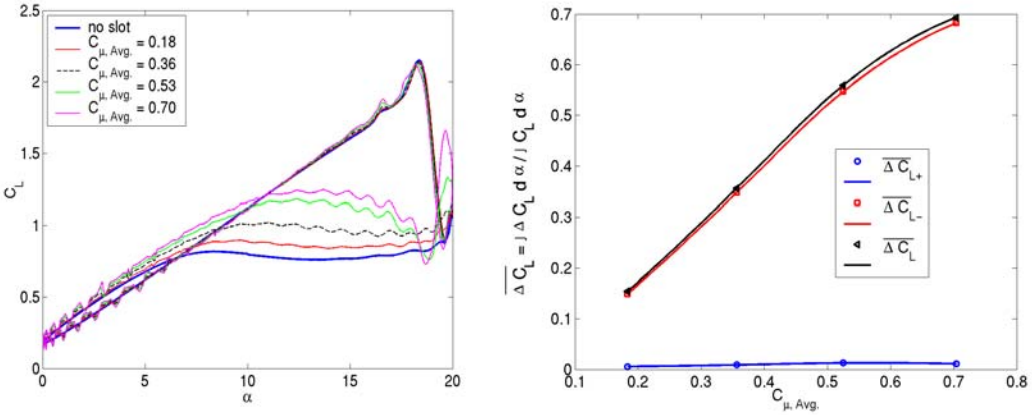

Figure 65. Unsteady C_L and variation of $\overline{\Delta C_L}$ with lower surface slot momentum coefficient. M=0.3, $\alpha = 10 + 10\sin(\omega t)$, SSCA09, slot angle = 20° and location = -0.235

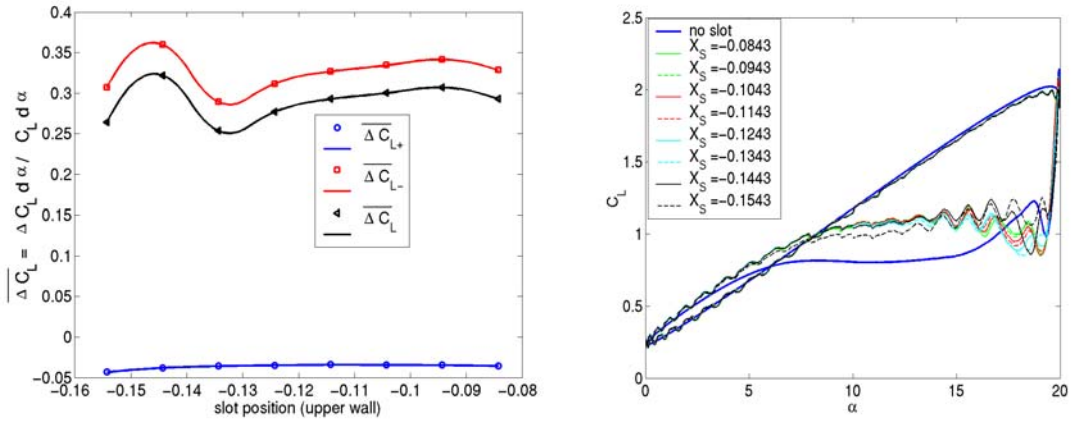

Figure 66. Unsteady C_L and variation of $\overline{\Delta C_L}$ with upper surface slot position for double-slot. M_∞=0.3, slot angle=20°, lower slot position = -0.235, and $C_{\mu\ Avg}$ = 0.13%.

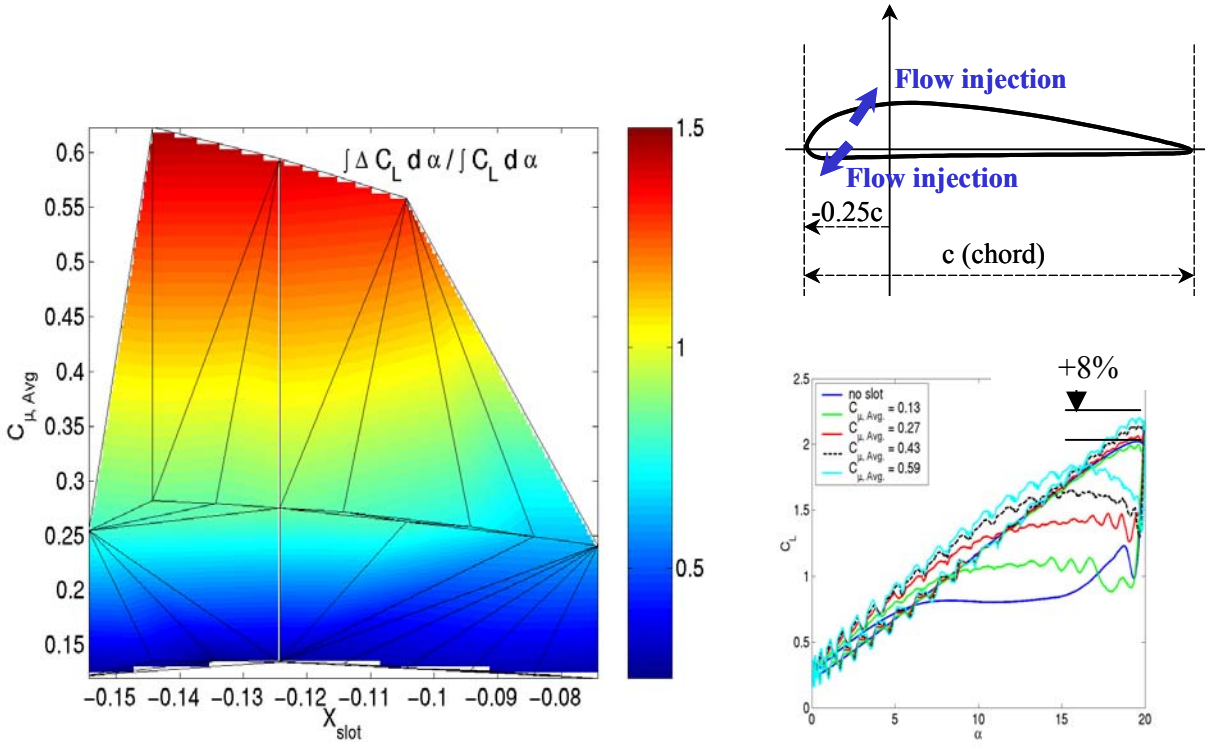

Figure 67. Contours of $\overline{\Delta C_L}$ with respect to Cμ level and upper surface slot position for double-slot. M_∞=0.3, slot angle=20°, lower slot position = -0.235.

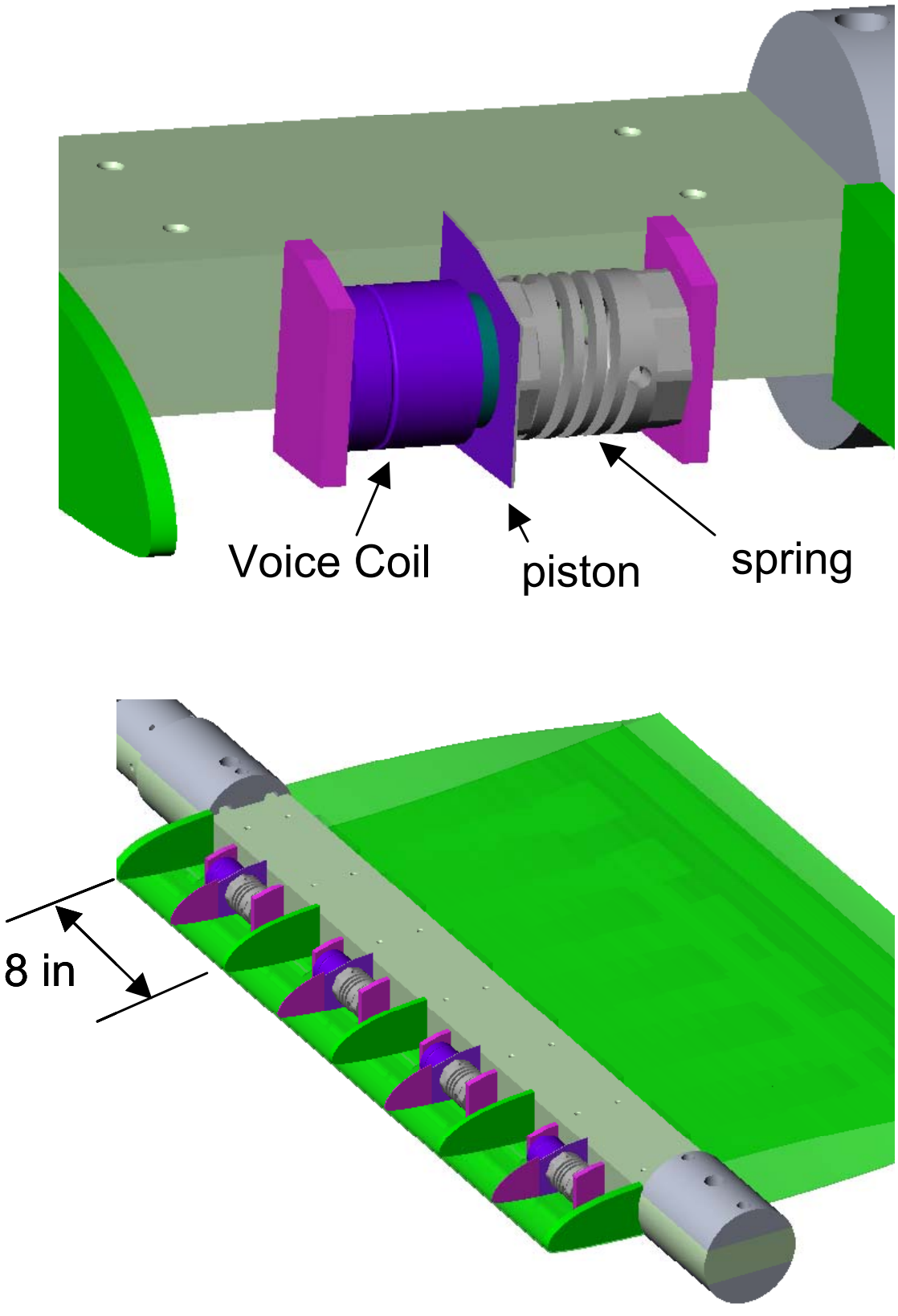

Figure 68. 2nd generation actuator arrangement

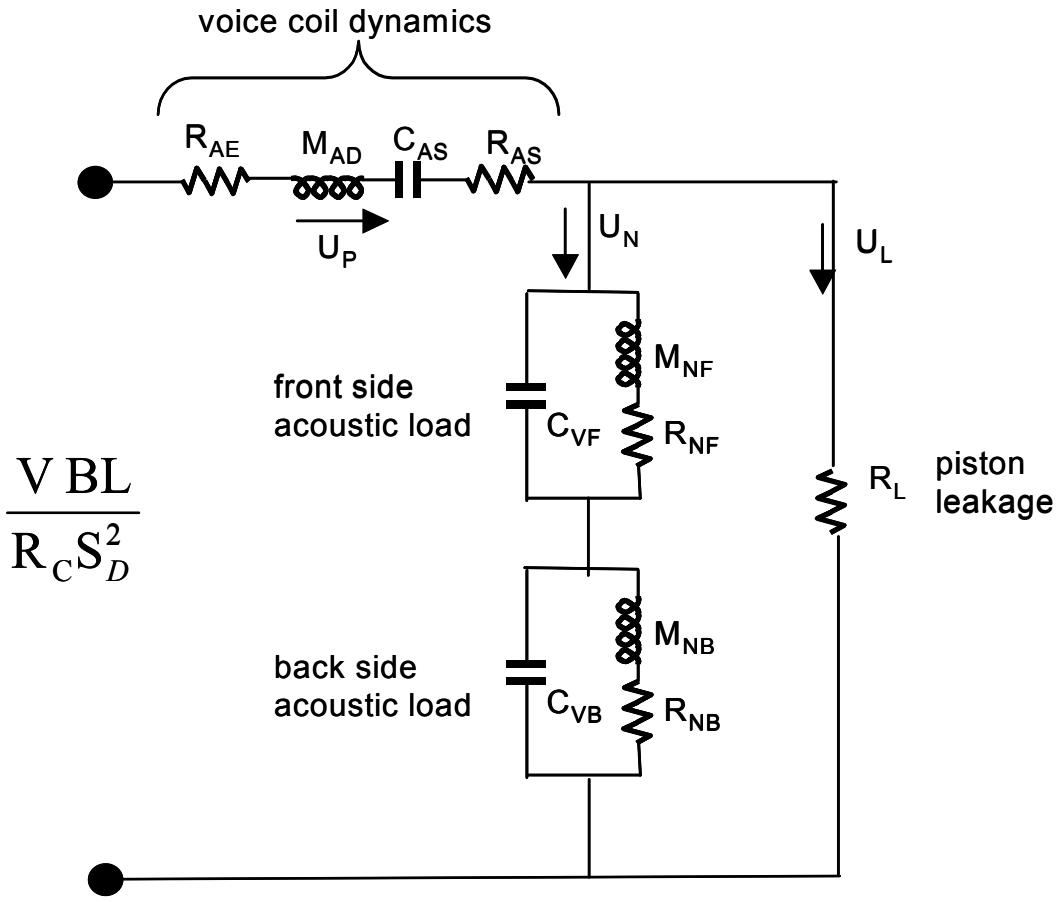

a) Full electro-acoustic model

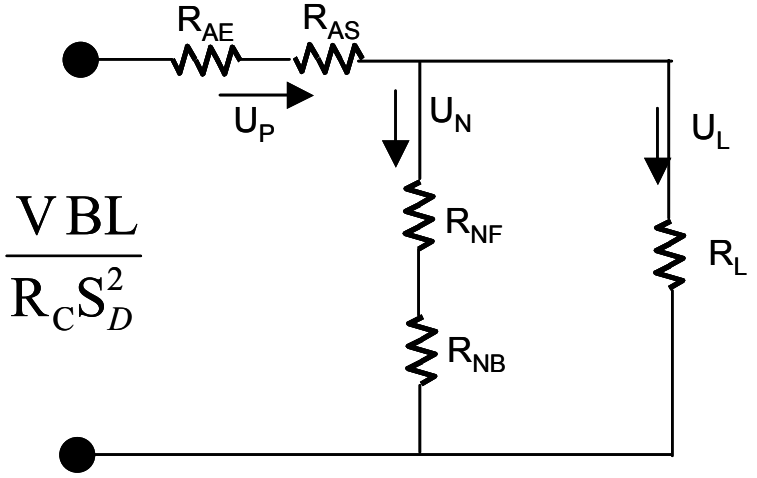

b) Approximate resonant model

Figure 69. Electroacoustic models of 2nd generation actuator

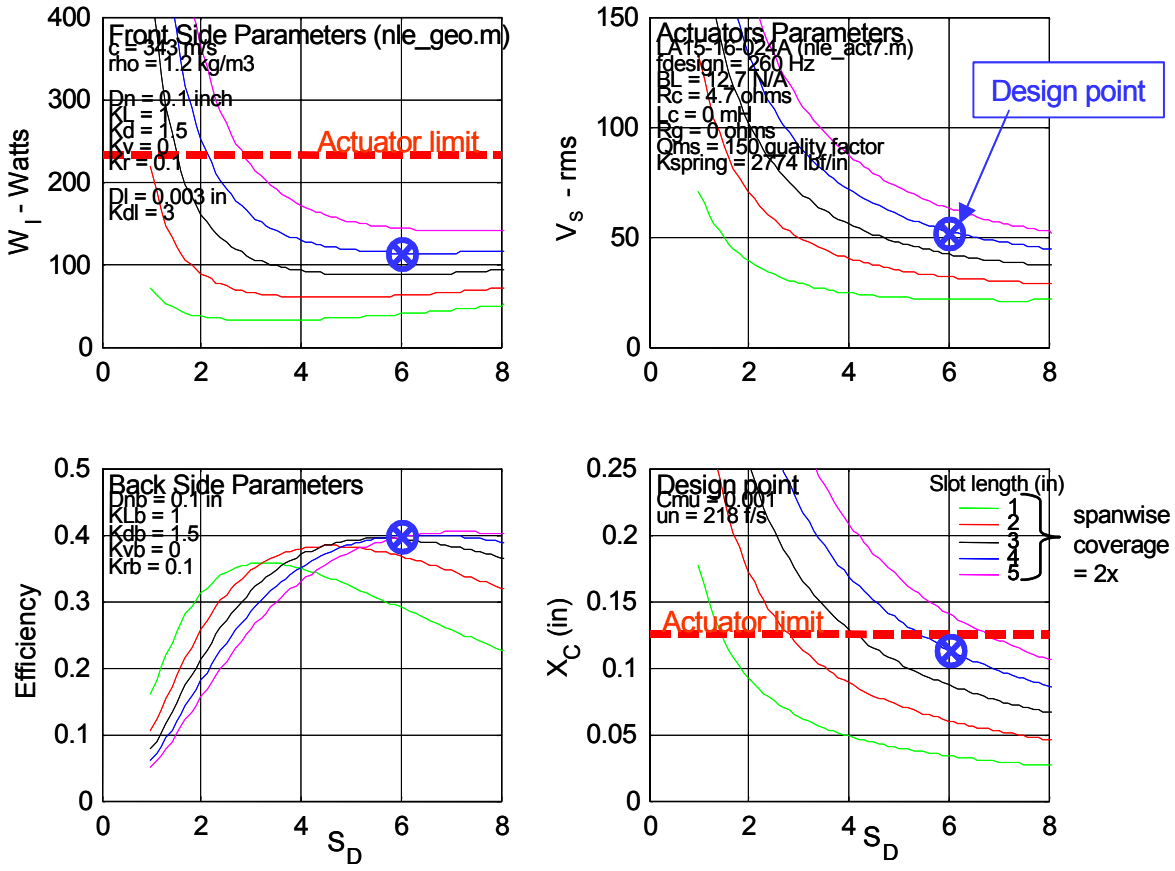

Figure 70. Actuator analysis with resonant model (Cμ=0.1%, slot width h = 0.1 in)

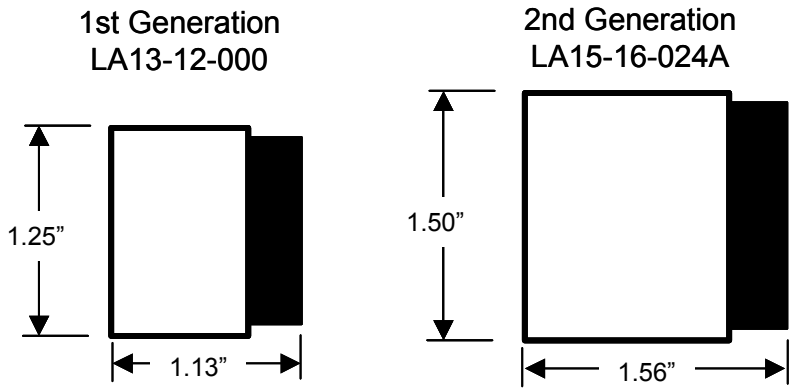

Coil weight:	14	44 g
Total motor weight:	115	225 g
Spring weight	100	254 g
Displacement:	0.125	0.125 in
Motor Const:	0.53	1.31 $lb_f/Watts^{0.5}$
Max. Power:	43	231 Watt

Figure 71. Comparison of 1st and 2nd actuator size and parameters

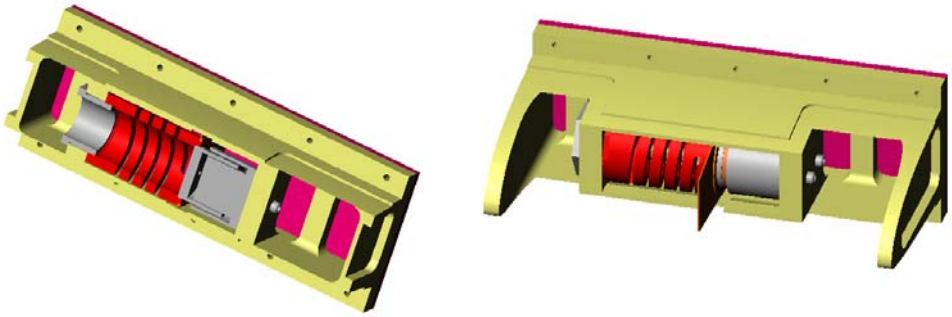

Figure 72. 2nd generator actuator design

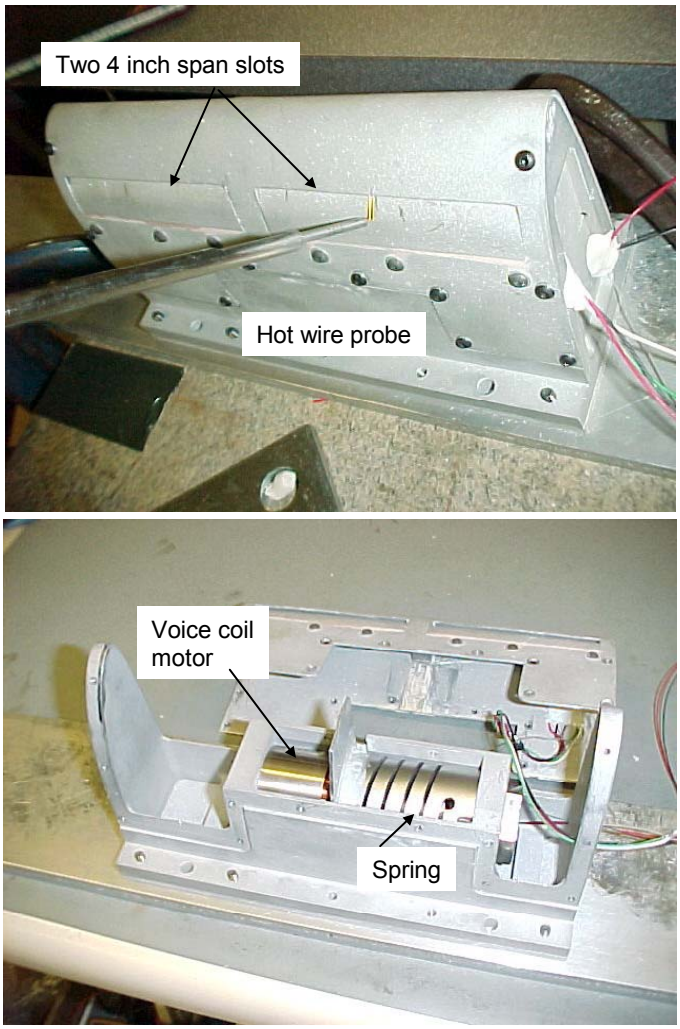

Figure 73. Bench top 2nd generation actuator

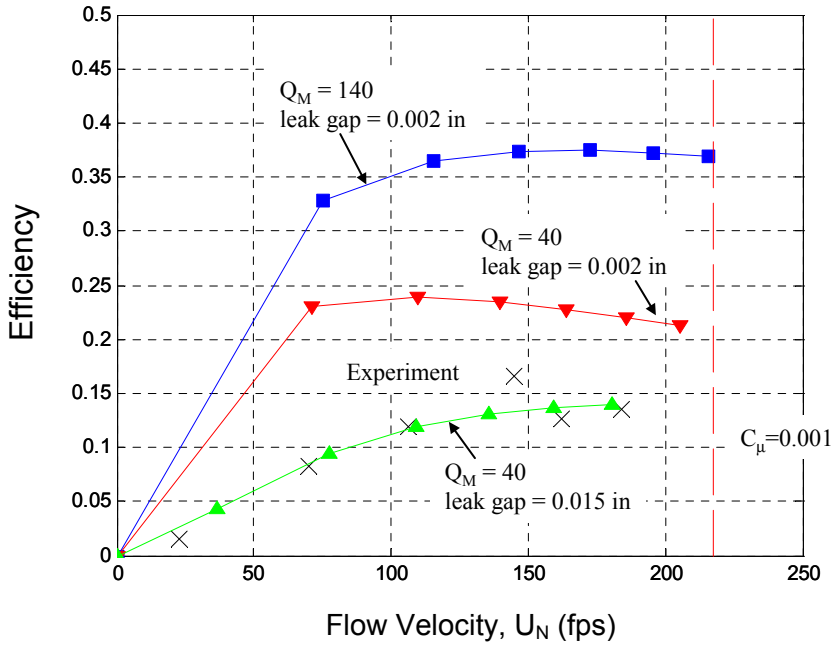

Figure 74. Bench top test results of 2nd generation actuator

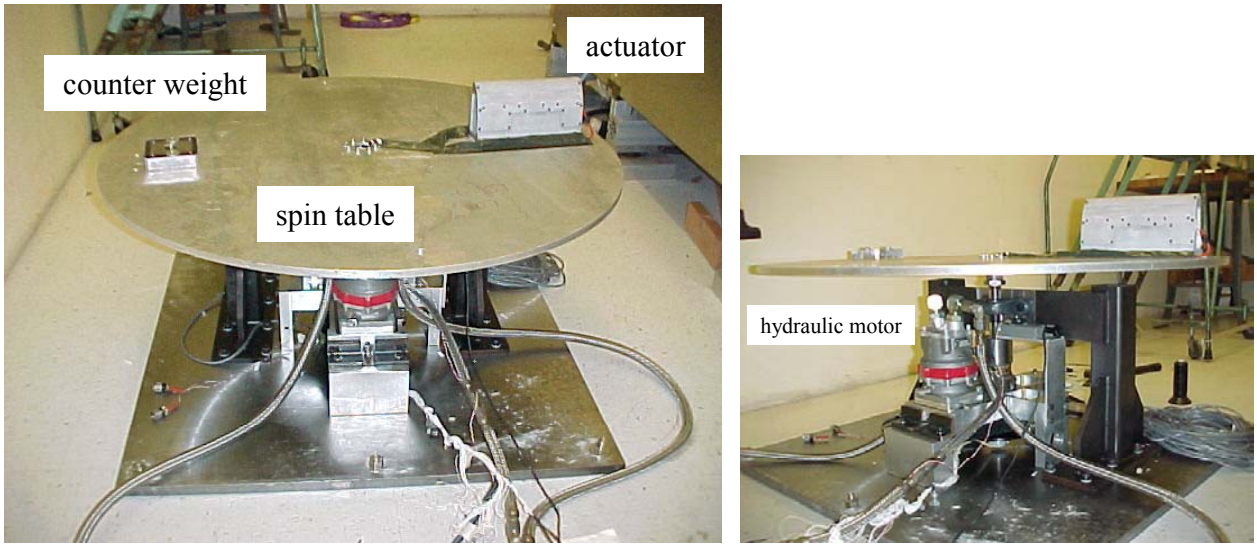

Figure 75. Actuator spin rig

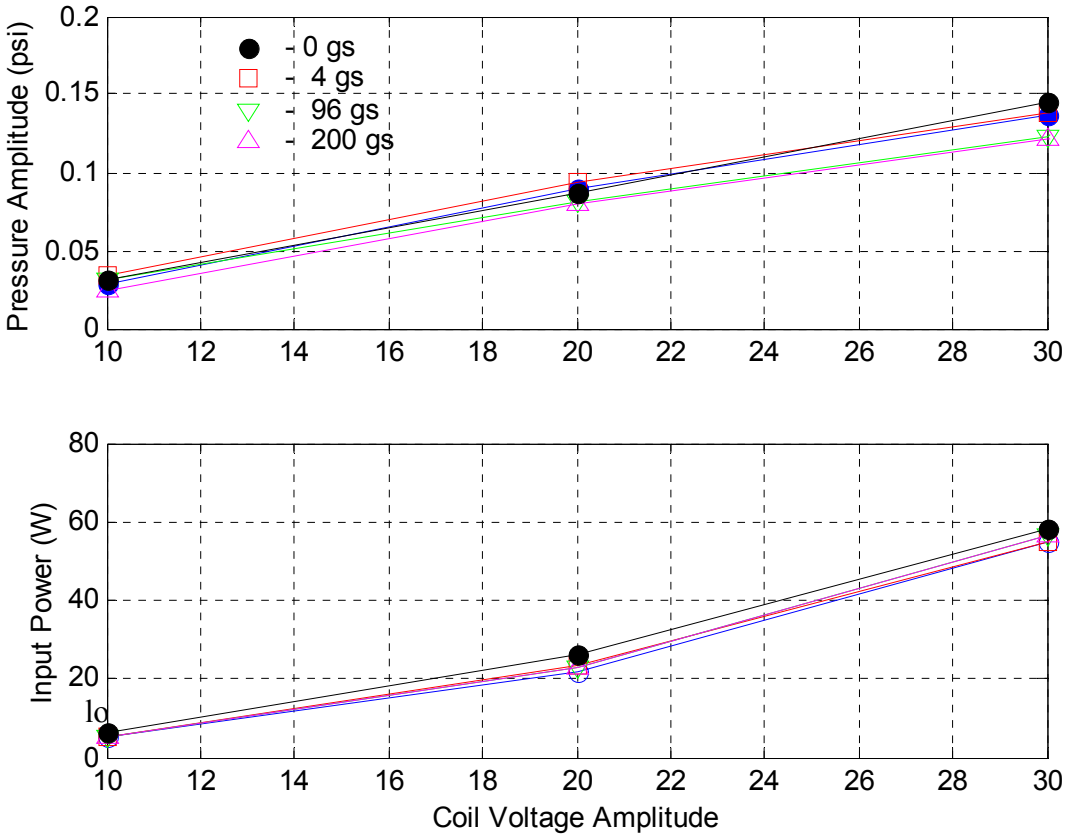

Figure 76. Actuator performance versus centrifugal